Shortening of the European Dauphinois margin (Oisans Massif, Western Alps): new insights from RSCM maximum temperature estimates and $^{40}Ar/^{39}Ar$ *in situ* dating.

M. Bellanger [a, b, c], R. Augier [a, b, c, *], N. Bellahsen [d, e], L. Jolivet [a, b, c], P. Monié [f], T. Baudin [a, b, c], O. Beyssac[g],

[a] Univ d'Orléans, ISTO, UMR 7327, 45071, Orléans, France
[b] CNRS/INSU, ISTO, UMR 7327, 45071 Orléans, France
[c] BRGM, ISTO, UMR 7327, BP 36009, 45060 Orléans, France
[d] Sorbonne Universités, UPMC Univ. Paris 06, UMR 7193, ISTeP, F-75005 Paris, France
[e] CNRS, UMR 7193, ISTeP, F-75005 Paris, France
[f] Géosciences Montpellier, CC 60, UMR 5243, Univ. Montpelier 2, Place Eugène Bataillon, 34095 Montpellier cedex 05, France
[g] Univ. Pierre et Marie Curie, UMR 7590 UPMC-CNRS, 4 place Jussieu, 75252 Paris cedex 05, France

* Corresponding author: romain.augier@univ-orleans.fr

Abstract

The Oisans Massif, located in the external zones of the western Alps, experienced significant shortening during the Alpine collision. While a series of major top-to-the west shear zones was recently described, the general low grade of the metamorphism has not attracted much petrological and geochronological studies. This paper provides combined temperature and age constraints on the evolution of the Oisans Massif. Temperature was estimated with the Raman Spectrometry of Carbonaceous Material (RSCM) method and chlorite geothermometry. Maximum temperature reached by the Mesozoic cover (Tmax) from Grenoble to the Galibier pass (E-W) and from Saint Jean de Maurienne to Embrun (N-S) yielded almost constant ca. 330°C temperatures all through the Massif. Temperatures however strongly decrease either westward toward the top of the Vercors sedimentary sequence or eastward toward the Penninic Frontal Thrust. Age constraints were retrieved using $^{40}Ar/^{39}Ar$ *in situ* analyses performed on variously strained samples from Alpine shear zones. Over strain gradients, incipient Alpine recrystallizations progressively develop at the expense of former Variscan parageneses. A combined textural and EPMA approach permitted to identify newly formed chlorite and phengite that unequivocally grew in response to deformation or to low grade metamorphism. Chlorites recorded temperatures from ca. 350 to 150°C during the activity of shear zones. In parallel, $^{40}Ar/^{39}Ar$ *in situ*

experiments enabled dating deformation using both synkinematic phengites crystallized below the closure temperature of white-micas and former Variscan muscovite whose isotopic system have been, at least partially re-opened. Activity of top-to-the-west shear zones responsible for the shortening and thickening of the Oisans massif thus occurred between 34-33 and 25 Ma. Integrating these new age-constraints, Tmax estimates, and published geological data on the Oisans Massif and neighbouring areas allow proposing a new shortening scenario for the external zones. From ca. 34-33 Ma, the Oisans Massif was buried as a rigid block below more internal units and reached temperature of ca. 330°C. Shearing progressively localized along a series of top-to-the-W shear zones in the basement until 25 Ma. Deformation then localised along a major thrust at the base of the ECM massif and propagated along the basement-cover interface below the Vercors massif after 16Ma.

1 Introduction

The involvement of basement units in the external zones of collisional orogens is still poorly understood because the associated deformation is not intense and metamorphic conditions not severe enough to erase the effects of earlier deformation episodes, rendering the syn-collision deformation difficult to recognize. The deformation and kinematic history of these continental units thus often remains partly enigmatic and the rheology of the crust in the early stages of collision poorly known.

The Oisans Massif, which belongs to the External Crystalline Massifs (ECM) of the Western Alps is a key-place to understand the first stages of continental collision. Major basement brittle/ductile shear zones reworking the earlier Variscan fabric have been recognized which have accommodated most of the collisional shortening (Wibberley, 1999, 2005; Bellahsen et al., 2012, 2014; Bellanger et al., 2014; Boutoux et al., 2014a), but precise P, T, time data are still lacking to better constrain the sequence of shortening and thickening.

The Oisans Massif also comprises a Mesozoic sedimentary cover, mainly deposited during the Early Jurassic rifting episode, which has not seen the Variscan metamorphic conditions and can thus be used to assess the Alpine history. Bellahsen et al. (2012) and Bellanger et al. (2014) have shown that localised west-verging Alpine shear zones developed in the basement during collision while the cover was strongly folded above without a major décollement in between. The geometry and kinematics of these shear zones is thus now established and it remains to estimate the P-T conditions of their development and to date them.

In this contribution, we first provide a map of the maximum temperature (Tmax) reached by the cover between Grenoble and the Galibier pass (E-W) and between Saint Jean de Maurienne and Embrun (N-S) (Fig. 1) using the RSCM method (Beyssac et al., 2002). It constrains the thermal history as well as the burial dynamics around the Oisans Massif. Then, we compare these Tmax with temperatures obtained in both basement and cover, using two chlorite geothermometers (Cathelineau and Nieva, 1985; Cathelineau, 1988; Vidal et al., 2001, 2005, 2006). In a second step, we provide EPMA analyses of white micas coupled to detailed microstructural and textural analysis of samples collected from various shear zones, in order to document the nature of these white micas, i.e. inherited vs. synkinematic. Finally, in a third step we performed *in situ* dating of white micas using the $^{40}Ar/^{39}Ar$ method. These results constrain the scenario of collisional shortening in the external zones of the Western Alps.

2 Geological setting

2.1 The Oisans Massif within the Western Alps

The Belledonne, Grandes Rousses, and Oisans massifs belong to the external zones and more particularly to the Dauphinois zone of the Western Alps (Fig. 1). External zones, which mainly recorded the Liassic rifting stage and the Oligo-Miocene collision event, were affected by a low-grade metamorphism after the end of Eocene. These massifs are parts of the External Crystalline Massifs (noted ECM, thereafter) that correspond to uplifted Variscan basement covered by Mesozoic to Cenozoic sedimentary series. The ECM were underthrusted below an orogenic prism made of stacked continental (Briançonnais zone) and oceanic (Piemontais zone) nappes transported along the Penninic Frontal Thrust (PFT). The PFT, also called the Crustal Pennine Thrust or the Embrunais Basal Thrust in Dumont et al. (2011, 2012) was active with top-to-the-(north-)west motion during the Early Oligocene (Ceriani et al., 2001; Tricart et al., 2001, 2006). The internal zones, east of the PFT (Fig. 1), corresponds to the subducted continental margin of Europe and the Ligurian Ocean. They are pervasively affected by high-pressure low-temperature (HP/LT) metamorphism, which occurred between 70 and 35 Ma (Rosenbaum and Lister, 2005; Berger and Bousquet, 2008). During the Palaeozoic, the Oisans Massif experienced a complex tectonometamorphic history (Debon and Lemmet, 1999; Guillot and Menot, 1999; Von Raumer et al., 1999; Guillot et al., 2009). High-grade Carboniferous metamorphism has strongly overprinted previous tectonometamorphic records. The Oisans Massif mainly consists of late Variscan

granites and earlier Devono-Dinantian plutonic and younger volcano-sedimentary sequences, including Visean conglomerates, volcano-sedimentary and coal intercalations (Barféty and Pêcher, 1984). The Belledonne and Rochail massifs were then structured by nappe stacking during the Visean and later affected by late Carboniferous to early Permian late-orogenic gravitational collapse (Guillot and Menot, 1999), contemporaneous with partial-melting and plutons emplacement between 330-290 Ma and the formation of extensional Stephano-Westphalian continental basins (i.e. in Grandes Rousses, Belledonne and La Mure massifs) (Barféty and Pêcher, 1984; Barféty et al., 1984, 1988; Guillot et al., 2009). This zone was ultimately eroded during Permian to Triassic times as evidenced by the continental Permo-Triassic deposits (sandstones and conglomerates together with coal intercalations) and middle to late Triassic shallow marine sediments (dolomitic limestone with evaporitic layers). These formations remained attached to the basement during Alpine deformation, and the contact can thus be used as a reference surface to quantify both the extensional strain during the rifting episode and the later compressional deformation during collision (Dumont et al., 2008, 2011; Bellahsen et al., 2012, 2014; Bellanger et al., 2014; Boutoux et al., 2014a).

During early Liassic times, the post-Variscan basement was stretched during the rifting episode (Dumont, 1988; Dumont et al., 1998), as evidenced by basaltic flows ("spilites") (Laurent, 1992) and a series of large-scale fault-bounded tilted blocks, limited by major normal faults that still shape the present-day geometry of the external zones (Barféty and Gidon, 1983; Lemoine et al., 1986; Lemoine and De Graciansky, 1988). During the early Liassic, the Meije block (Fig. 3) was a horst, as evidenced by a condensed sedimentary cover and shallow paleobathymetric conditions (Roux et al., 1988; Bouillin et al., 1997; Corna et al., 1997).

After the rifting stage, the Liguro-Piemontais oceanic domain formed between the European and Apulian continental domains from the Bajocian onward, as evidenced by the age of the first sediments deposited above the ocean floor (De Wever and Caby, 1981; De Wever et al., 1987). Subduction of the Ligurian domain, which started during late Cretaceous times was followed by subduction of the leading edge of the European continental margin under the Apulian microplate as evidenced by the HP to UHP metamorphism in the internal zones (e.g., Chopin, 1984; Agard et al., 2001). The more proximal margin was subducted to shallow depths and shortened and the deformation propagated outward.

The "Pyreneo-Provençal phase", Late Cretaceous to Early Eocene in age, responsible for E-W folds and thrusts especially in the southern part of the external zone, is the first post-

Variscan shortening event (Lemoine, 1972; Caby, 1973). Ante-Senonian E-W fold axes described in the Dévoluy massif, were recently interpreted as due to submarine sliding (Michard et al., 2010). The Nummulitic series are deposited within the foreland flexural basin from Lutetian/Bartonian to Priabonian/Rupelian (Sinclair, 1997; Du Fornel et al., 2004 Mulder et al., 2010). They uncomformably overly reverse faults associated to N-S shortening, south of the Oisans Massif (Ford, 1996). The timing and the kinematics of other thrusts north of the Oisans Massif, such as the Meije or Combeynot thrusts, are debated, whether they are pre- (Barbier, 1963; Bravard and Gidon, 1979; Ford, 1996), or syn- to post-Nummulitic (Beach, 1981b; Dumont et al., 2011; Bellanger et al., 2014). The only evidence of N-S to NW-SE Oligocene shortening within the basement is restricted to a narrow area around the PFT (Bellanger et al., 2014).

The main Alpine collisional tectonometamorphic event in the external zones was thus due to its burial under the internal units immediately after the deposition of a Rupelian olistostrome topping the Nummulitic series, the so-called "schistes à blocs" (Kerckhove, 1969; Gidon and Pairis, 1980; Sinclair, 1997; Mulder et al., 2010). In the Oisans Massif, E-W shortening was responsible for folding in the cover with axial plane cleavage development in the west (Gratier and Vialon, 1980; Bellahsen et al., 2012; Bellanger et al., 2014). The metamorphic peak reached 300 to 350°C for 1-5 kbar (Waibel, 1990; Jullien and Goffé, 1993; Crouzet et al., 1999, 2001; Ceriani et al., 2003), which implies a tectonic overburden of around 10km when considering a normal geothermal gradient. The temperature in the Bourg d'Oisans area (Crouzet et al., 1999, 2001) reached 330°C after the end of deformation. The metamorphic peak was dated with large uncertainties around 26-24 Ma by K-Ar method in fine clay fraction from the cover (Nziengui, 1993), zircon fission-tracks ages ranging between 27 Ma (alt. 3065m) and 13 Ma (alt. 1310m) (van der Beek et al., 2010). A deformation stage was dated between 34 and 27 Ma by $^{40}Ar/^{39}Ar$ phengite ages from strike-slip shear zones related to E-W shortening in the eastern part of the Oisans Massif (Simon-Labric et al., 2009). Bellahsen et al. (2012) and Bellanger et al. (2014) have further proposed that the E-W shortening in the Oisans Massif was mainly accommodated by kilometer-scale top-to-the-west reverse shear zones, which are summarized in the next section.

2.2 Inherited or newly formed: the Oisans shear zones revisited

Contrary to the internal zones where deformation is too intense to preserve former structures, the amount of shortening of the Oisans Massif was less than ca. 30-40% during the Alpine collision (Dumont et al., 2008; Bellahsen et al., 2012, 2014; Bellanger et al.,

2014). As a consequence, inherited structures are still preserved, which allows studying relationships between inherited and Alpine newly formed structures. The detailed structural evolution of the Oisans Massif, which is beyond the scope of the present paper, was recently investigated by Bellahsen et al. (2012) and Bellanger et al. (2014) in order to describe the distribution of the deformation in the basement.

The Oisans Massif presents unambiguous evidence of intense shortening either at small (outcrop) scale or at large (kilometric) scale. Maps of shortening axes of small-scale structures together with transport directions over the whole Oisans Massif reveal only one major E-W shortening stage (Fig. 2). Strain localization in the basement leads to the formation of a set of newly-formed, top-to-the-west, reverse shear zones that fold the basement-cover interface to the west and form large basement thrusts near the Penninic Frontal Thrust (Bellanger et al., 2014). Alpine shear zones can be separated from the Variscan deformation by the lower-temperature, more localised character of the deformation that cross-cuts a former high-temperature, pervasive Variscan fabrics. Moreover, an Alpine age is ensured by the deformation with consistent top-to-the-west kinematics within the Triassic-Liassic tegument (Bartoli et al., 1974; Barféty and Pêcher, 1984; Bellahsen et al., 2012; Bellanger et al., 2014).

While similar Alpine shear zones of Argentera or Mont Blanc massifs were recently dated from the Oligo-Miocene (Rolland et al., 2008; Sanchez et al., 2011a; Cenki-Tok et al., 2013), the only recent constraints on the timing of the Alpine deformation were performed on strike-slip shear zones of the eastern Oisans Massif (Simon-Labric et al., 2009). The most prominent structures accommodating most of the shortening, W-directed reverse shear zones remain therefore undated.

3 Aims and methods

To put age-constraints on reverse shear zones developed during collision in the Oisans Massif, deformed rocks of four main shear zones were sampled across the W- E profile. These are, from west to east: the Col de Cluy, Plan du Lac, Col du Lac and Combeynot shear zones (Fig. 2), all sharing a common and consistent E-W to SE-NW stretching lineation and an overall top-to-the-west sense of shear. *In situ* $^{40}Ar/^{39}Ar$ laser ablation method (Maluski and Monié, 1988) was chosen as it allows linking radiochronology to petrology and particularly to textures/structures (Agard et al., 2002; Müller, 2003; Augier et al., 2005; Gerber, 2008). This link is particularly important as

different parameters such as temperature, deformation or fluid circulations may drastically impact the behaviour of the K/Ar system. It is therefore crucial is to decipher the respective contribution of these parameters to isolate the signal related to deformation.

To ensure a reliable T record, temperatures were constrained at the scale of the Oisans Massif and the neighbouring areas using the Raman Spectrometry of Carbonaceous Material method (RSCM; Beyssac et al., 2002; Lahfid et al., 2010). These data were supplemented by local temperature estimates using the chemical composition of chlorite in the chlorite-quartz-water equilibrium (Vidal et al., 2001, 2005, 2006) either to control RSCM results or to put direct constraints within the shear zones. In parallel, impact of the deformation was evaluated by a combined textural/petrological study of the dated samples and particularly the behaviour of white-micas. Besides, the potential impact of the fluid percolations was evaluated by a careful study of output isotopic ratios. The next sections are dedicated to a brief description of the methods used in this study.

3.1 Raman spectrometry of carbonaceous material (RSCM)

The Raman Spectrometry of Carbonaceous Material method (Beyssac et al., 2002) is based on the quantitative study of the degree of graphitization of carbonaceous material (CM), which is a reliable indicator of metamorphic T. Because of the irreversible character of graphitization, CM structure is not sensitive to the retrograde reactions during exhumation and therefore depends on maximum T (noted Tmax, thereafter) reached during metamorphism (Beyssac et al., 2002). Tmax can be determined in the range 200-650°C by using two empirical geothermometers which link the degree of graphitisation measured from Raman Spectra (RS) to the highest temperature ever experienced by the rock (Beyssac et al., 2002; Lahfid et al., 2010). Lahfid et al. (2010) geothermometer was used when the D4 defect band was present in the RS, for the low-grade rocks. Absolute precisions of ca. 50°C between 650 and 300°C and ca. 25°C between 330 and 200°C are related to uncertainties on petrological data used for the calibration. However, relative uncertainties on Tmax appear however much smaller, probably around 10-15°C and variations of that order of magnitude may be detected (Beyssac et al., 2004, 2007; Gabalda et al., 2009; Vitale-Brovarone et al., 2013).

All Raman spectra were measured and analysed following procedures described in Beyssac et al. (2002, 2004 and 2007) and Lahfid et al. (2010). Raman spectra were obtained using a Renishaw InVIA Reflex microspectrometer (IMPMC, Paris, France) with a 514 nm argon laser. RSCM analyses were conducted on thin sections prepared on CM-rich metasediments

particularly abundant in the cover series in the studied area, cut in the structural X-Z plane (i.e. orthogonal to foliation and parallel to lineation). To avoid defects on the CM related to thin-section preparation, analyses were all performed below the surface of the section by focusing the laser beam beneath a transparent crystal (i.e. dominantly quartz, calcite, albite and occasionally phyllosilicates). Before each session, the spectrometer was calibrated with a silicon standard. 10-20 spectra were routinely recorded for each sample to smooth out the inner structural heterogeneity of CM within samples.

3.2 Microprobe and independent temperature estimates

Mineral analyses were performed with a Cameca SX50 electron microprobe (ISTO-BRGM, Orléans). Analytic conditions were 15 kV accelerating voltage and 10 nA beam current using Fe2O3 (Fe), MnTiO3 (Mn, Ti), diopside (Mg, Si), CaF2 (F), orthoclase (Al, K), anorthite (Ca), albite (Na) as standards. Elements, which are measured in %weight of oxide, are SiO_2, Al_2O_3, Fe_2O_3, MgO, MnO, CaO, Na_2O, K_2O, TiO_2, F and Cl. Chemical composition of chlorite and the white-micas were particularly studied. Composition of chlorite has been used to retrieve independent T constraints using a thermodynamic approach (Vidal et al., 2001, 2005, 2006). Besides, composition of white-micas was used to distinguish different mineral generations to characterise the dated minerals.

Chlorite, which is abundant in the studied low-grade metamorphic rocks, was used as a geothermometer. Temperatures were estimated by two ways: i) traditional empirical geothermometry based on temperature dependency of the Si, Al and vacancy content of the tetrahedral and octahedral sites within chlorite (Cathelineau and Nieva, 1985; Cathelineau, 1988), and ii) a thermodynamical approach (Vidal et al., 2001, 2005, 2006) that integrates multiple substitutions ($FeMg_{-1}$, $Al_{IV}Al_{VI}Si_{-1}Mg_{-1}$, $(Mg, Fe^{2+})_3\square_{-1}Al_{-2}$ where □ is the vacancy). In the last case, metamorphic temperatures that prevailed during the formation of chlorite were estimated upon 4 equilibria at fixed water activity and pressure (a_w=1 and P=4kbar (Simon-Labric et al., 2009)). Standard deviations are routinely close to ±10°C (from ±4°C to ±32°C).

3.3 In situ *$^{40}Ar/^{39}Ar$ dating*

The $^{40}Ar/^{39}Ar$ *in situ* laser ablation method was first described by Schaeffer et al. (1977) and successively upgraded by York et al. (1981) and Maluski and Monié (1988). Procedure was detailed in Agard et al. (2002), Augier et al. (2005) or Turrillot et al (2011).

We recall here the main stages for $^{40}Ar/^{39}Ar$ *in situ* sample preparation and analytical procedure.

Measurements were all performed at Géosciences Montpellier (France) with an analytical system that consists of: (a) an IR-CO_2 laser of 100 kHz used at 5-15% during 60-80 sec; (b) a beam shutter for selection of exposure times; (c) a lenses system for beam focusing; (d) a camera connected to the monitor for beam focusing and selection of ablated zones; (e) a steel chamber with a copper plate and the four samples on. This chamber is depressurized to 10^{-8} to 10^{-9} bar; (f) an inlet line for purification of gases including two Zr-Al getters; (g) a Argus VI (Thermo-Fisher) multi-collector mass spectrometer from; (h) a software which controls the timing of extraction/purification and the data acquisition. Rock sections of 1 mm thick, which had been used to make the petrographic thin-sections, were double polished to c. 1 µm. Whole section and detailed-area photographs of both the rock section and corresponding thin section were taken for an accurate selection of suitable areas for laser experiments. All samples were ultrasonically rinsed in ethanol and distilled water, wrapped in pure aluminium foils and then irradiated in the Triga Mark II nuclear reactor (Pavia, Italia) with several aliquots of the Fisch Canyon sanidine standard (28.03 ± 0.08Ma, (Jourdan and Renne, 2007) as flux monitors. After irradiation, both the monitors and the sections were placed on a Cu-holder inside the sample chamber and heated for 48 h at 150–200 °C.

For each experience, argon was released from a 100 x 300 µm mean surface corresponding very often to aggregates of white micas. Incision of the sample did not exceed 10-20 µm depending on the three-dimensional orientation of the white mica crystals. For each experiment, ages have been obtained after correction with blanks, mass discrimination, radioactive decay of ^{37}Ar and ^{36}Ar and irradiation-induced mass interferences. They are reported with 1σ uncertainty and were evaluated assuming an atmospheric composition for the initially trapped argon [i.e. $(^{40}Ar/^{36}Ar)_i$ = 295.5]. The proportion of ^{38}Ar and ^{37}Ar isotopes that result from interference with chlorine and calcium during irradiation reveals the contribution of Cl and Ca-rich minerals or inclusions to the overall argon release and so to the calculated age. A blank analysis was done every two or three analyses to evaluate the argon background within the whole analytical system. Isotopic data are computed with the ArArCalc freeware (Koppers, 2002) based on the algorithms described in (York, 1968; Faure, 1986; McDougall and Harrison, 1988; Renne et al., 1998; Min et al., 2000).

Along with a strong dependency with temperature and deformation, the behaviour of the K/Ar system in white micas can be partially altered by fluid circulations. As fluid

316 circulations are hardly detected *a priori*, output isotopic ratios ($^{36}Ar/^{39}Ar$, $^{37}Ar/^{39}Ar$ and
317 $^{38}Ar/^{39}Ar$ ratios) were carefully checked.
318
319 **4 Temperature record within the sedimentary cover**
320
321 ***4.1 A large-scale RSCM Tmax cover in the sedimentary series***
322
323 ***First order thermal features***
324 Our dataset consists of 70 samples collected across the external zones, from Vif to
325 the Penninic Frontal Thrust (E-W transect) and from Saint Jean de Maurienne to Chorges
326 (N-S transect) in various lithologies and all structural units of the studied area except
327 Variscan basement rocks (Table 1, Fig. 4). A more systematic sampling was performed
328 along the E-W transect where the thermal structure is so far poorly documented. Results are
329 all presented in maps of various scales and projected along structure-orthogonal cross-
330 sections. For the sake of comparison, results of previous studies including illite-crystallinity
331 maps (Aprahamian, 1974; Barlier et al., 1974) or RSCM data in bounding areas (e.g.
332 Gabalda et al., 2009) are also shown (Fig. 4).
333 At first glance, an unexpected major result of this study is the relative homogeneity of the
334 Tmax value at the scale of study area, with an average value of ca. 330°C (329±8 for 27
335 Tmax values along an E-W cross-section), from the Lower Jurassic series close to Vif, all
336 the way to the Galibier pass, at the eastern edge of the study area (Fig. 4, 5). Conversely,
337 lower Tmax ca. 200-220°C is recorded to the south either in the Mesozoic series or Eocene
338 flysch (north of Saint Michel de Chaillol; Fig. 4). Moreover, Tmax results recorded further
339 south along an E-W section between Chorges and l'Argentière-la-Bessée (Fig. 4) highlight a
340 drastic southward lateral change in the thermal structure. There, Tmax values present an
341 overall upward temperature increase from 253±10°C to more than 330±5°C in the vicinity of
342 the Penninic Frontal Thrust. Besides, additional important temperature variations were
343 recorded either to the west of the study area (Belledonne and La Mure massifs), to the east
344 in the vicinity of the Penninic Frontal Thrust (Fig. 4, 5). These variations are described here
345 in more details.
346
347 ***Thermal structure of the western bound of the Belledonne and La Mure massifs***
348 To the west of the Belledonne and La Mure massifs, Tmax values decrease upward
349 the stratigraphic succession from 334±6°C-329±8 in the Liassic, 325±6-286±5°C in

calcareous Dogger and 227±23-<200°C in upper Jurassic black-shales (Fig. 4, 5) highlighting a ca. 130°C temperature variation. In details, Tmax values gradually decrease sequence along a ca. 30°C/km gradient but also highlight a localised temperature decrease near the top of the calcareous Dogger (296±5-286±5°C) and the base of the upper Jurassic (227±23-204±14°C). This ca. 80°C temperature gap can be followed 40 km strike, which is consistent with a normal sense west-dipping tectonic contact located within the upper Jurassic black-shales (Oxfordian). However, due to poor local outcrop conditions, this contact has not been observed in the field.

In the same area, the base of thick Jurassic sequences of the Vercors yielded Tmax value close to 335°C (334±6°C) while the thin Jurassic cover of the Belledonne and La Mure massifs yielded only ca. 280°C (279±9°C). In this case, Tmax distribution evidenced an east-verging shear zone/thrust consistent with the description of a large-scale backthrust in the field by Butler (1989). The Mesozoic sequence of the Vercors therefore appears i) transported eastward above the La Mure thrust which roots in Triassic or Liassic units, and ii) is partly dismembered by an extensional structure (Fig. 4, 5).

Thermal structure in the vicinity of the Penninic Frontal Thrust

To the east of the study area, close to the Lautaret and Galibier passes, Tmax values decrease gradually from ca. 330°C in the easternmost Mesozoic cover of the Oisans Massif to ca. 260°C in the Helmintoids flysch (Tête Noire area) despite the presence of numerous tectonic contacts including the PFT. Tmax results therefore align well along an apparent 20-30°C.km^{-1} gradient suggesting either that the Tmax imprint was post-tectonic or that extensional movements are not restricted to the PFT and rather distributed over numerous small-scale, normal-sense structures. In any case, in their current position, Briançonnais units did not experience Tmax higher than ca. 270°C which fall well below the ca. 330°C temperatures characterising the internal Dauphinois. Conversely, a ca. 40°C localized temperature drop is recorded further south, across the PFT (around L'Argentière-la-Bessée, Fig. 4) where the Nummulitic series yielded ca. 330±5°C while Briançonnais units only experienced 291±6°C. There, this result is consistent with both field and low-temperature thermochronology evidences of the reactivation of the PFT as an extensional structure (Tricart et al., 2001, 2004, 2006, 2007; Ceriani and Schmid, 2004).

4.2 Independent temperature record using chlorite geothermometry

Four samples were selected from the sample collection of the sedimentary cover for the RSCM approach (see location on Table 2 and on Fig. 2). The main aim of this approach is to estimate the temperature recorded by the cover series using independent geothermometers based on the chemical composition of chlorites (Cathelineau and Nieva, 1985; Cathelineau, 1988; Vidal et al., 2001, 2005, 2006). Results are all presented on figure 6.

Chlorites present different habits and occur in various textures. They are either dispersed in the matrix (samples A-2-2, A-4-232, see location Fig. 2), crystallized within veins (samples A-1-345(2)) or along the foliation and top-to-the-W shear bands (sample A-1-321). Irrespectively to their structural position and to the potential impact of the protolith bulk chemical composition, the two geothermometers yielded quite consistent results for all samples within both the analytical and calibration errors and the within-sample internal dispersion. However, the thermodynamical approach generally yield more dispersed temperature results between ca. 210 and 350°C than empirical geothermometry that show an unimodal distribution centrered on the narrow ca. 270-330°C range (Fig. 6). Temperature ranging from 150 to 350°C was retrieved from sample A.2.2, 150-340°C from sample A-4-232, 230-380°C for sample A-1-321 and 240-390°C for sample A-1-345 (Fig. 6). Interestingly, RSCM Tmax fall systematically within the high temperature value indicating i) the cross-validation of the methods and that ii) chlorites, at variance with the RSCM, do record other discrete metamorphic increments. However, textural observations did not allow distinguishing the relative timing of successive chlorite growth events during the metamorphic evolution (prograde or retrograde (re-)equilibrations).

5 Phyllosilicate habits, chemical composition and chlorite temperature (TChl) record for dated samples

The crystallisation-deformation relationships of chlorite and white-micas that were first recognised in the field were then strengthened by detailed textural observations in thin-section. Mineral chemical compositions were used to constrain i) the chemistry of dated minerals and ii) the physical conditions by chlorite geothermometry. Together with textural observations, these results are of prime importance to gather accurate *a priori* constraints and discussion elements for *in situ* laser-probe investigations.

5.1 First order common features: guidelines for the $^{40}Ar/^{39}Ar$ in situ approach

At the scale of the outcrop, rocks present routinely large white-mica crystals. Conversely, aggregates of very fine-grained white-micas occur only in deformed zones. At the scale of thin-sections, deformed samples present two contrasted habits of white-micas. Large, up to 2mm variously oriented white-mica flakes appear closely associated with a former high-temperature foliation and high-temperature parageneses (Fig. 7). These crystals coexist with aggregates of fine-grained white-micas growing either at the expense of former large crystals or in cracks of various scales within feldspars. Besides, this population presents a close association with deformation structures and particularly with top-to-the-west shear bands within proto-mylonites, mylonites or phyllonites. This strong correlation has been observed at the scale of strain gradients along which large, well-developed white-mica clasts tend to disappear whereas fine-grained blasts form the frame of the rock (Fig. 7). Interestingly, EPMA analyses reveal the existence of two texturally controlled groups of white-mica of contrasted compositions reminding the results of Lanari et al. (2012) in the Briançonnais domain, further east. The first group, which plots close to the muscovite end-member composition, is mainly represented by the large white-micas clasts population carried by an earlier foliation (Fig. 7). Besides, the Na-content of this population is systematically higher than 0.05 a.p.f.u. (atoms per formula unit) while the Si content is lower than 3.1 a.p.f.u. (Fig. 7). The second group, mostly corresponding to fine-grained aggregates of white-micas, has a phengite chemistry, i.e. between muscovite and celadonite end-member due to Tschermak substitutions. This group presents variable silica-content scattered between 3.2 and 3.6 a.p.f.u. and Na-content systematically lower than 0.05 a.p.f.u. (Fig. 7, 8). However, the small size of crystals and large internal variations of compositions suggest a partial mixing between two end-members.

EPMA analysis of the chemical compositions confirm the presence of two unrelated generations of white-micas recognised on the basis of textural observations and characterized by contrasted chemical compositions. Being conspicuously involved with the greenschist facies partial reequilibration of former high-temperature parageneses and closely associated with a top-to-the-W asymmetry, phengites therefore appear as a synkinematic mineral particularly suitable to put age-constraints on the deformation. Conversely, the habits of pre-kinematic clasts and the muscovite composition of most of the large white-mica population are likely inherited crystals pertaining to Variscan parageneses.

Besides, temperature, which is the most important factor controlling Argon diffusion, must be estimated to make a difference between cooling and deformation (crystallisation) ages. Similarly to temperature estimates performed in the cover series, temperature recorded by basement rocks was estimated using two different chlorite geothermometers. Results are all presented in figure 8.

5.2 Textural and chemical characteristics of dated samples

Following this structural and chemical guideline, white-micas present in the dated samples were carefully studied. Besides, chemical composition of chlorite was used to constrain the temperature experienced by the rocks. Results are all presented from west to east on figure 8.

Col de Cluy shear zone

Samples from Col de Cluy are Variscan micaschists and gneisses with greenschist to amphibolite facies associations with quartz, white-micas, feldspar, biotite and/or chlorite. Rocks show generally only an incipient recrystallization. Former biotite and K-feldspar are still preserved and locally abundant. White-micas, which are present in all samples, mostly occur as ca. 1-2mm weakly deformed flakes and locally as clasts involved in shear bands. This population coexists with fine-grained white-micas that occur as rare isolated aggregates. Grain-size is generally less than 10 x 50 µm and white-mica crystals are often closely associated with chlorite. EPMA analyses of the white-micas mostly plot within a rather narrow composition range close to the muscovite end-member. Analyses of fine-grained white-micas plot along continuous pattern from muscovite (Si(3.05); Na(0.09;0.12)) to low-silica content phengite (Si(3.15;3.25); Na(0;0.02)) (Fig. 8). Chlorite occurs as numerous small-scale aggregates. Chlorite shows variable composition with 70 to 85% of clinochlore and XMg values close to 0.45 for variable silica content. Geothermometric results yield quite contrasting results. While the thermodynamic approach yielded dispersed temperature between 150 to 370°C, empirical geothermometry showed quite consistent ca. 230 to 320°C temperature results (Fig. 8). Being devoid of conspicuous Alpine re-equilibrations, these samples appear, at a first glance poorly suitable to allow dating the deformation and were therefore not used for the $^{40}Ar/^{39}Ar$ *in situ* approach.

Plan du Lac shear zone

Thanks to good outcrop conditions allowing the recognition of the strain distribution, the Plan du Lac shear zone was particularly studied. Four samples were selected over the strain gradient. Sample A-4-74b is a proto-mylonite sample showing a rather weak Alpine deformation by comparison to samples A-4-68 and 68b that are phyllonites. Sample A-4-66b was selected from an intermediate position within the strain gradient. All samples show a clear top-to-the-west asymmetry except sample A-4-66b picked along a localized top-to-the-E shear zone.

All samples derive from a quartz, feldspar, biotite and white mica Variscan gneiss. Chlorite pervasively replaces biotite either as static pseudomorphs in low strain domains or as synkinematic crystallisations in mylonites. In low strain domain, white mica occur as large, up to ca. 1-2mm clasts with clear disequilibrium textures while fine-grained white-mica are rare and clearly secondary. Conversely, mylonite and phyllonite are almost devoid of large clasts and exclusively made of fine-grained white-micas. EPMA composition of white-micas reveals two distinct poles with very few intermediate values (Fig. 8). The first pole that corresponds to muscovite (Si(3.15); Na(0.06;0.08)) and the second one to a silica-rich phengite (Si(3.2;3.4); Na(0;0.02)) (Fig. 8). Interestingly, mineral composition shows a conspicuous dependency to deformation. Mylonite and phyllonite samples yield mostly phengitic white-micas. Conversely, less-deformed proto-mylonite sample yield texturally-controlled chemical compositions with muscovite compositions for the large clasts and phengite composition for the fine-grained blasts.

Chlorite is locally abundant. It occurs in the matrix, growing at the expense of biotite, crystallized in syn-deformation veins or associated with fine-grained white-micas along shear planes. Most analyses yield consistent results with 70 to 90% of clinochlore content, an XMg close to 0.45 for a variable silica content (Fig. 8). Regardless of strain intensity, structural position and habits, most results cluster between 260 to 290°C (Fig. 8).

Col du Lac shear zone

Sample A-1-355 was collected from the core of a top-to-the-W shear band characterized by a thin layer of phengite-quartz phyllonites. This sample derives from a Variscan high-grade gneiss still preserved a few decimetres apart on the same outcrop. The rock is made of quartz, feldspar and biotite partly turned into chlorite. Interestingly, white

mica is absent from the mineralogical composition of the protolith. Small-scale but abundant white-mica aggregates from the phyllonites are therefore newly-crystallized as the result of strain and/or fluid-induced destabilization of the K-feldspar (e.g. Gueydan et al., 2003). Accordingly, EPMA analyses of the white-micas all yielded phengitic compositions with a very low dispersion (Si(3.2;3.4); Na(0;0.02)).

Chlorite occurs as small-scale aggregates and rare dispersed larger crystals that may derive from former biotites. Chlorite shows almost constant composition close to the clinochlore end-member with XMg values around 0.6. Most geothermometric results cluster between 250 and 290°C for both geothermometers (Fig. 8).

Combeynot shear zone

Sample A-1-345 was selected in the most deformed outcropping ductily-deformed basement rocks of the Combeynot shear zone. Mylonites are scarce and proto-mynolites, derived from orthogneiss, which belongs to a volcano-sedimentary complex (Barbier et al., 1973), are often directly overthrusted onto the sedimentary cover. White micas occur generally as large clasts surrounded by very fine-grained blasts. Aggregates of fine-grained white-micas also occur in tension gashes in K-feldspar. Composition of white-micas shows a rather continuous pattern from muscovite (Si(3.05;3.15); Na(0.06;0.08)) to phengite (Si(3.25;3.5); Na(0;0.02)) (Fig. 8). Despite a clear partially reequilibration within Alpine physico-chemical conditions, Alpine white-micas occur as very fine grained aggregates.

Chlorite is rare, small and often closely associated with white-micas. Thus, most chlorites show mixed composition with white-micas (i.e. K-rich chlorite) and were thus discarded. Data are thus only presented in table 2.

Synkinematic fine-grained aggregates of phengite appear particularly adapted to put age-constraints on the activity of the shear zones. Accordingly, samples from Col de Cluy shear zone which may record only a weak Alpine re-equilibration have not been selected from the *in situ* $^{39}Ar/^{40}Ar$ approach. For all other samples, success of the study relies on our ability to effectively analyze newly formed crystals whose typical size is often small (150µm max.).

Temperatures recorded in the shear zones yielded very consistent results close to 250-300°C which falls below RSCM Tmax recorded in the cover series. Chlorite therefore probably recorded retrograde metamorphic increments during exhumation and cooling of the Oisans

Massif. It is noteworthy that temperatures recorded at peak-T conditions also fall below the lower bound of the closure temperature of white-micas (e.g. Dodson, 1973; Cliff et al., 1998; Villa, 1998).

6 $^{40}Ar/^{39}Ar$ age constraints

Our dataset consists of 199 *in situ* $^{40}Ar/^{39}Ar$ ages performed on 7 samples collected over three main Alpine shear zones, namely (from west to east), the Plan du Lac, Col du Lac, and the Combeynot shear zones (Table 3, see location on Fig. 2). To ensure the coverage of the different strain facies recognized in the field, a more systematic sampling was performed over the Plan du Lac shear zone. Results of the *in situ* $^{40}Ar/^{39}Ar$ approach are all shown and discussed in Fig. 9 as apparent ages for which an initial $^{40}Ar/^{39}Ar$ ratio of 295.5 is assumed for the non-radiogenic argon component. These age results are described in the light of the textural/structural observations, chemical composition results and the output isotopic ratios ($^{36}Ar/^{39}Ar$, $^{37}Ar/^{39}Ar$ and $^{38}Ar/^{39}Ar$) informative of potential disturbances of the K/Ar system. For small-scale phengite aggregates located in the vicinity of chlorite, calcium or fluid inclusions-bearing minerals, the release of the ^{38}Ar and ^{37}Ar isotopes interfering with chlorine and calcium revealed that argon was extracted from both phengites and K-poor minerals (Brereton, 1970; McDougall & Harrison, 1988). The quoted errors represent one sigma deviation and do not include uncertainty on the monitor. Errors are routinely inferior to ca. 1 Ma while larger error (ca. 2 to 15 Ma) are generally due to both a weak argon signal and a high atmospheric contribution (Table 3).

At a first glance, an important conclusion is that the successive phengite generations recognized on the basis of textures (e.g. Fig. 7), compositions (Figs 8) effectively yield successive ages. Fine-grained aggregates of synkinematic phengites yield Alpine ages *sensu lato*. Conversely, white-micas characterized by muscovite chemical compositions and/or presenting clear pre-kinematic (i.e. inherited) habits yielded pre-alpine ages or even sometimes Variscan ages. Interestingly, a clear dependency to the intensity of the deformation may even be detected either at the scale of the sample or at the scale of the strain gradient within a shear zone (e.g. Fig. 10). Therefore, most ages are tentatively interpreted either as, at least partially, re-opened Variscan isotopic systems for “old” ages or as genuine crystallization ages for the “young” ca. 35-25 Ma ages. More locally, results however show important age variations that may also record fluid percolations.

6.1 Plan du Lac shear zone

In order to study the potential impact of the finite Alpine deformation, four samples were selected over a single strain gradient toward the core of the Plan du Lac shear zone. The relative structural position of samples is given on figure 10.

A-4-74b (Proto-mylonite)

In this sample, discrete ca. 1mm-thick shear bands partially overprint a high-temperature inherited texture composed by large, brittlely fractured feldspar clasts and more ductilely stretched quartz and muscovite crystals (Fig. 10). Conversely, this sample contains Alpine phyllosilicates including phengite and chlorite either carried along a weak vertical foliation, or crystallized along top-to-the-W shear bands. A total of 40 apparent *in situ* analyses were performed to cover all situations. Apparent *in situ* ages are scattered between 207 ± 5.2 Ma and 24.3 ± 1.8 Ma (Fig. 10). 22 analyses corresponding to the oldest ages are correlated with high $^{38}Ar/^{39}Ar$ ratio and atmospheric content (Table 3) but ages fall within the age range of uncontaminated phengites. Interestingly, the core of the shear bands provides ca. 25 Ma consistent ages (24.3 ± 1.8 Ma and 26.7 ± 0.6 Ma).

A-4-66b (Top-to-the-E Mylonite)

This sample is characterized by a schistosed high-grade gneiss traversed by a 3 mm-thick top-to-the-E shear band (Fig. 10). While Variscan fabrics are still well developed in most of the rock volume, Alpine synkinematic recrystallizations are almost complete within shear bands. There, former muscovites and feldspars are absent and a ca. 2mm thick phengitized fringe is developed (Fig. 10). 34 *in situ* analyses were performed. No relationship between apparent ages and the $^{37}Ar/^{39}Ar$ and $^{38}Ar/^{39}Ar$ variations were detected, except for the 3 three apparent ages older than ca. 100Ma, which have high $^{38}Ar/^{39}Ar$ values (Table 3). Analyses show a first order textural control of the age. Large muscovites, at least partially preserved within the matrix yielded 301.4 ± 6.6 and 62.3 ± 1.4 Ma. Conversely, small-scale phengites within the shear band yielded 30 alpine ages ranging between 40.5 ± 1.1 Ma and 29.5 ± 0.6 Ma plus an older age of 47.6 ± 1.2 Ma (Fig. 10). Interestingly, while ages depict a clear first order younging toward and within the shear band, older ages occur within the core of the shear band over a ca. 1-2mm-thick fringe (Fig. 10). In this case, a late gradient of ^{40}Ar excess seems to overprint an initial age gradient related to deformation.

A-4-68 (Phyllonite)

Sample A-4-68 is a phyllonite sample. 15 *in situ* analyses were performed and yielded ages ranging between 93.5 ± 2.0 and 22.4 ± 0.9 Ma (Table 3). Most of apparent ages cluster between 32 and 22 Ma (Fig. 10). There is no relationship of apparent ages with $^{37}Ar/^{39}Ar$ unlike with $^{38}Ar/^{39}Ar$, suggesting some interaction with chlorine-rich fluids that may occur as trapped inclusions (Fig. 10).

A-4-68b (Phyllonite)

Sample A-4-68b was cut in two distinct rock slabs (section 8 and 5) selected only a few centimeters distant; section 5 being a little less deformed than section 8. Analyses performed on section 5 yielded 21 apparent ages, ranging between 114.2 ± 4.3 and 25.9 ± 0.5 Ma (Fig. 10). Analyses present a strong relationship between apparent ages and $^{37}Ar/^{39}Ar$, $^{38}Ar/^{39}Ar$ and atmospheric content. In the absence of Ca-rich and Cl-rich phases in the chip, contamination may be rather related with fluid inclusions trapped in the analysed phengites (Table 3). Despite contamination by Ca-rich and Cl-rich fluids, analyses yielded ages of about 25-27 Ma. Interestingly, analyses performed on section 8 yielded 44 apparent ages, which do not show any evidence of a direct relationship with the $^{37}Ar/^{39}Ar$, $^{38}Ar/^{39}Ar$ and atmospheric content. These ages are scattered between 37.2 ± 1.0 Ma and 23.2 ± 0.6 Ma (with two old ages of 46.4 and 47.2 Ma) and define mainly two age groups at 31-33 Ma (7 ages) and 25-27 Ma (18 ages) (Fig. 10).

6.2 Col du Lac shear zone (Sample A-1-355, phyllonites)

Sample A-1-355 was collected from the core of a top-to-the-W shear band characterized by a ca. 1 meter-thick layer of phyllonites. This sample derives from a Variscan high-grade gneiss still preserved a few decimetres apart on the same outcrop and turned into a phengite-quartz rock in the most deformed zone. It contains few chlorites and no remnant of inherited muscovites present in the undeformed protolith. The 30 apparent ages are scattered between 110 ± 7 Ma and 15 ± 10 Ma and 25 of them range between 42.68 ± 2.22 and 23.88 ± 1.6 Ma (Table 3). No correlation between the apparent age and $^{38}Ar/^{39}Ar$ and $^{37}Ar/^{39}Ar$ ratios was observed. However, some analyses, particularly the “old”, up to 50 Ma ages present high $^{38}Ar/^{39}Ar$ values and/or an important atmospheric contribution (Table 3). Interestingly, these old ages were found in micas from C'-type shear bands and therefore argue for a ^{40}Ar excess. These results are quite similar to those obtained in the most deformed parts of sample A-4-66b. Despite this potential contamination, analyses with low

$^{38}Ar/^{39}Ar$ ratio and low atmospheric content yielded 15 internally consistent apparent ages scattered between 32.9 ± 0.9 and 24.8 ± 0.6 Ma (Fig. 10).

6.3 Combeynot shear zone *(Sample A-1-345, proto-mylonite)*

Sample A-1-345 was selected in the most deformed outcropping ductilely-deformed basement rocks of the Combeynot shear zone. Mylonites are scarce and protomylonites, derived at the expense of orthogneiss (former leucogranite) are often directly overthrusted onto the sedimentary cover. It is the less deformed sample of the data set. None of the 15 *in situ* analyses provide Alpine age (Table 3, Fig. 10). Instead, apparent ages are distributed between 389 ± 27 Ma and 156 ± 3 Ma with no clear textural control. Part of the apparent ages is correlated with the $^{38}Ar/^{39}Ar$ ratio, which suggests a possible contribution of Cl-rich phases or fluid inclusions. High $^{37}Ar/^{39}Ar$ ratios (Table 3) are probably due to the degassing of Variscan epidote or titanite, but again no systematic correlation between the variation of these ratios and the age dispersion was observed.

7. Discussion

7.1 Reliability, significance of the RSCM Tmax mapping

RSCM Tmax estimates has proven an efficient mean to put extensive temperature constraints on the thermal structure of coherent units or on the importance of tectonic contacts (Beyssac et al., 2002; Augier et al., 2005; Negro et al., 2006; Gabalda et al., 2009; Angiboust et al., 2011). In the Oisans Massif, RSCM Tmax fall in the same temperature range as more punctual results issued from other methods available in literature. The most important result is the uniformity of Tmax values at the scale of study area, with an average value of ca. 330°C with a relative error that may not exceed 10-15°C (Beyssac et al., 2004). Thermopaleomagnetic studies indicate that cooling started from 335°C in the north of the Emparis formations and in the Bourg d'Oisans basin, after the main tectonic phase at ca. 25 Ma (Ménard and Rochette, 1992; Crouzet et al., 1999, 2001) (Fig. 11). The stability field of paragenesis observed in the Jurassic cover (quartz-cookeite-margarite-pyrophyllite) that most likely recorded peak-metamorphism conditions in the Emparis basin is restricted from 270 to 340°C and from 1 to 5kbar (Jullien and Goffé, 1993) (Fig. 11). Besides, the overall

thermal structure of the Oisans Massif as recorded by the distribution of RSCM Tmax is consistent with illite-crystallinity maps (Aprahamian, 1974; 1988; Barlier et al., 1974) (Fig. 4).

Related to the irreversible character of graphitization, and the insensitivity of the CM structure to retrograde reactions (e.g. Beyssac et al., 2002; Lahfid et al., 2010; Aoya et al., 2010), RSCM record the highest temperature ever undergone by the rock sample. In principle, RSCM Tmax results issued from a continuous section may therefore be diachronous and represent the superimposition of distinct thermal events.

In the Bourg d'Oisans and Emparis basins, metamorphic peak-T conditions of ca. 335°C where reached at ca. 25 Ma (i.e. Crouzet et al., 1999, 2001). As the restored sedimentary cover of this area is generally thinner than ca. 2 km (Barféty et al., 1972; Barbier et al., 1973; Crouzet et al., 2001; Bellahsen et al., 2012), these temperatures are clearly ascribed to an Alpine tectonometamorphic event and particularly to the tectonic burial of the Dauphinois domain under internal units (Crouzet et al. 2001; Dumont et al., 2008). Besides, the progressive temperature decrease toward the top of the overthrusting units close to the Galibier pass is consistent with a late to post-tectonic temperature imprint, as suggested by thermopaleomagnetic results (Crouzet et al., 1999, 2000). Interestingly, the upward RSCM Tmax evolution indicates a ca. 20-30°C.km^{-1} gradient (Fig. 4C), which is consistent with the gradient around 20 to 25°C.km^{-1} proposed by Crouzet et al. (1999) but lower than the ca. 40-50°C.km^{-1} gradient deduced from fluid inclusion data (Gratier et al., 1973; Nziengui, 1993) (Fig. 12). However, high geothermal gradients deduced from fluid inclusions may result from an underestimated pressure due to reequilibriation of fluid inclusion densities during an isothermal decompression as proposed by Boullier (1999) or Crouzet et al. (2001).

Conversely, in the sedimentary cover west of the Belledonne Massif, Tmax values show large temperature variations from 335°C to less than 200°C (Fig. 4, 5). Tilted with the bedding, this ca. 130°C Tmax upward sequence decrease may witness a post-metamorphic peak westward tilting of the sedimentary succession (Fig. 4, 5). Moreover, Tmax recorded at the base of the succession is consistent with the ca. 8 km thickness of the Mesozoic series assuming a ca. 40°C.km^{-1} geothermal gradient (Philippe et al., 1998). Besides, this result is consistent with the 60 to 80 mW.m^{-2} basal heat flow estimated in this area (Deville and Sassi, 2006) and a bulk thermal conductivity close to 1.5 W.m^{-1}.K^{-1} (Beardsmore and Cull, 2001).

Minor and local fluid circulations along the basement-cover interface cannot be ruled out but an overall thermal imprint related to large-scale fluid circulations is unlikely as available

studies show that the fluid flow operated only at small scale in the studied area (Henry et al., 1996; Kirschner et al., 1999; Boutoux et al., 2014b).

7.2 Significance of the $^{40}Ar/^{39}Ar$ in situ *ages*

Geochronological data and particularly $^{40}Ar/^{39}Ar$ data are traditionally interpreted as recording closure of the isotopic system at a specific temperature depending on the isotopic diffusion properties of the mineral (e.g. Dodson, 1973; Cliff et al., 1998; Villa, 1998; Harrison et al., 2009). Accordingly, many studies therefore assume that the closure temperature of the K/Ar system for muscovite argon retention is around 350-450°C depending on cooling-rates, grain-size and other controlling factors such as the geometry of the diffusion domain (e.g. Wijbrans & McDougall, 1986; Hames & Bowring, 1994; Reddy et al., 1996; Villa, 1998). Using recent results of modeling, the closure temperature for muscovite would fall in the range of 400-420°C for a 10-30°C.Ma^{-1} cooling-rate and a diffusion radius of 100µm (Harrison et al., 2009). However, closure temperature for phengite is still discussed as it may largely vary as a function of both intrinsic (e.g. grain-size) and extrinsic (cooling-rates, temperature, pressure and deformation or fluid circulations) parameters. Recent studies suggest that phengite is more retentive for argon than muscovite and that phengite ages are interpretable as crystallisation ages to temperature as high as 500-550°C (e.g. Dunlap, 1997; Agard et al., 2002; Müller, 2003; Mulch and Cosca, 2004; Augier et al., 2005; Mulch et al., 2005; Gerber, 2008; Rolland et al., 2008, 2009; Sanchez et al., 2011a). Temperature experienced during the Alpine orogeny by dated samples did not exceeded 330°C ± 30°C since they initially cooled at the end of the Variscan Orogeny. Ages of the fine-grained synkinematic phengites therefore likely represent crystallization ages. Conversely, large, inherited clasts of muscovite may reflect Variscan cooling ages in the absence of additional disturbing factors. Stratigraphic constraints indicate that the flexural basin of the external zones was diachronously filled up from Lutetian to Bartonian (45 to 33Ma) (Du Fornel et al., 2004; Mulder et al., 2010; Salles et al., 2011). Burial of this basin below internal units occurred during Rupelian (34 to 28 Ma; Fry, 1989; Sinclair, 1997; Ford and Lickorish, 2004; Mulder et al., 2010). In Champsaur and Saint-Antonin basins, amphiboles reworked from Oligocene volcanism coeval with deposition yielded ca. 34-31 Ma Priabonian ages by $^{40}Ar/^{39}Ar$ methods (Féraud et al., 1995; Ivaldi et al. 2003), giving a maximum age for the burial of the basins under the

internal nappes. In addition, part of the Oisans Massif formed a 500 m high relief in the Oligocene (Gupta and Allen, 2000) and dated samples, restored in their inferred initial position, were probably less than 2km deep, between ca. 40 and 34 Ma. It therefore appears unlikely that phengites were formed under these P-T conditions and the ca. 34-33 Ma age clearly fixes the upper bound of the possible ages for the deformation of the Oisans Massif. 97 *in situ* experiments yielded ages younger than 34 Ma.

Interestingly, young ages are clearly correlated with the intensity of fine-grained white-micas blastesis particularly important in high-strain zones. It is therefore proposed that ages younger than 34 Ma reflect synkinematic crystallisation ages and thus deformation ages, in a broad sense. In addition, apparent ages show a bimodal distribution with a first age group settled at ca. 33-30 Ma and a second group at ca. 28-25 Ma ages (Fig. 11). These results are consistent with results of a conventional $^{40}Ar/^{39}Ar$ approach performed on wrench shear zones of the same area (Simon-Labric et al., 2009). However, our interpretation differs. Based on age spectra scattered between 32 and 24 Ma, Simon-Labric et al. (2009) proposed the superimposition of two distinctive shearing events (one at ca. 32 and one ca. 24 Ma). In this study, the use of an *in situ* mean over strain gradients allow linking deformation ages and the amount of finite strain experienced by the rocks. Accordingly, proto-mylonite and mylonite samples yielded older, ca. 33-30Ma ages while highly strained samples (phyllonites) yielded younger ca. 28-25 Ma ages, suggesting that the deformation progressively localized along the phyllonite bands thus leaving large rock volumes devoid of further recrystallizations. In any case, intense E-W shortening started with or just after the burial of external zones under the internal nappes around ca. 34-33 Ma and was still active at ca. 25 Ma. Synchronous deformation ages of either top-to-the-W reverse shear zones or wrench shear zones thus confirm the small-scale mutual cross-cutting relationships observed in the field (Bellanger et al., 2014).

102 in situ experiments yielded ages mostly clustering between 100 and 40 Ma with ages as old as 380 Ma. Older than ca. 34 Ma and presenting sometimes pre-Alpine or even genuine Variscan ages, theses apparent ages clearly do not record alpine collisional deformation. Relying on temperature estimates throughout the studied area, the temperature concept predicts that all white-micas sharing common pre-Alpine textures and inherited muscovite chemical composition should yield the same age corresponding to the time elapsed since initial cooling at the end of the Variscan Orogeny. Yet this is not the case for most analyses. On the contrary, the correlation of in situ $^{40}Ar/^{39}Ar$ ages and finite strain intensity at any scale reveals that ages are texturally-controlled and therefore independent of closure

temperature. This deviation to the closure temperature concept could be simply explained in terms of presence of ^{40}Ar excess either due to (1) partial deformation-induced resetting of Variscan muscovites (inherited argon), or (2) genuine incorporation of extraneous argon related to fluid circulations. Besides, a straightforward yet possible source of geologically meaningless ages could be simply explained by mixtures between inherited muscovite and synkinematic phengite argon reservoirs during lasering.

At first glance, as stated above, an overall correlation with the intensity of the finite strain can be drawn between samples. Weakly strained samples (from the Combeynot or the Plan du Lac shear zones) yielded rather old, sometime only pre-Alpine ages while phyllonites yielded much younger ages that tend to crystallization ages of newly formed crystals. Such control by the deformation is also perceptible at the scale of some dated rock samples with an overall age decrease toward the core of a shear band from ca. 300 Ma to less than 30 Ma in less than 1 centimetre (Fig. 11). It appears therefore tempting to ascribe to deformation the ability to facilitate argon diffusion and thus to partially reset (i.e. re-open) inherited muscovite isotopic system. Intensity of deformation, whether it occurs by grain-size reduction during mylonitization or by presence and distribution of high-diffusivity pathways lattice-modifying microstructures would therefore be the main controlling factor explaining the age scatter between an inherited cooling ages and the age of a tectonometamorphic event (i.e. Scaillet et al., 1990; West and Lux, 1993; Hames & Cheney 1997; Kramar et al. 2001, 2003; Mulch et al. 2002). As suggested by the linear relationships observed between some apparent ages and corresponding $^{38}Ar/^{39}Ar$ ratios arguing for interactions with Cl-rich fluids, minor excess argon cannot be simply ruled out. Besides, a limited yet conspicuous input of extraneous argon within and in the vicinity of shear bands is clearly detectable for some samples (Fig. 10). In this case, results of absolute chronology are markedly inconsistent with the relative chronology established independently on the basis of microtextures. For example, mylonite sample A-4-66b presents a series of ca. 50-40 Ma old ages occurring within the core of the shear band while other analyses show a clear age decrease toward the shear band. Excess argon was moreover reported within fluid inclusions from Oisans basement quartz veins (Nziengui, 1993). In this study seven K/Ar experiments on white-micas from the sedimentary cover yielding initially 48 to 30 Ma ages were corrected to 27-23 Ma by removing excess ^{40}Ar content from fluid inclusions. If excess argon exists, it should have a homogeneous composition at the scale of the whole study area, which seems particularly unlikely. Excess argon is therefore present but does not explain the first order features of the results.

7.3 A new tectonic scenario

This study brings primarily T-t-d (Temperature-time-deformation) results that further constrain the tectonometamorphic evolution of the external zones of the Western Alps. In this section, these results are all integrated into a compilation of published P-T-t-d results (Fig. 11 and 12) in order to discuss a new tectonic scenario (see also in Bellahsen et al., 2014) (Fig. 13).

Among the new results, this study constrains the thermal structure of a large volume of the external basement. Results, despite local variations, show a constant Tmax around 330°C. This constant temperature along several tens of kilometres suggests that the basement and the cover preserved in half-grabens have been first quickly underthrust with rather limited internal shortening. Deformation ages from this study and from Simon-Labric et al. (2009) are consistent with a burial of the external zones around between 34 and 25 Ma (Fig. 12, 13). The main shortening seems to have occurred at or around the metamorphic peak (Fig. 12) as suggested in Boutoux et al. (2014b). The distribution of isotherms obtained with thermopaleomagnetic method, which cross-cut the folds, indicates that the main shortening had ended before cooling started in the Bourg d'Oisans basin (Crouzet et al., 1999). The sampled profile may therefore correspond to an east-dipping isotherm (around 330°C) during underthrusting of the Oisans Massif, which would then suggest that the whole area behaved as a more or less rigid block below the internal units during part of its burial history, before it was ultimately shortened. Similarly, the geothermal gradient observed close to the Lautaret and Galibier passes (around 20-30°C.km^{-1}) seems to seal the PFT activity dated between 32 and 27 Ma (Freeman, 1998). Thus, deformation mainly occured just prior or during metamorphic-peak conditions and seems, in any case, to have ceased before the onset of the main cooling event. During this time period, and around the metamorphic peak conditions, the external zone crust underwent homogeneous shortening until approximately 25 Ma. Shortening was progressively localized into phyllonite bands. At 25 Ma, the crust was progressively decoupled from the subducting lithosphere and started to exhume. The PFT was then inactivated. These results argue against a progressive westward thrust slice development that lead to the exhumation of units after that they have reached

852 diachronously temperatures close to 330°C. However, this would imply that the basement
853 top has been heated up uniformly from 50-100°C to 300-350°C uniformly over ca. 70km,
854 which in turn suggests a rather slow burial.

855 At the scale of individual shear zones, high-strain samples (phyllonite) are younger
856 (28-25Ma) than proto-mylonite and mylonite (33-30Ma). This suggests that deformation
857 progressively localized along phyllonite bands. Moreover, ages of deformation (33-25 Ma)
858 reveal that the deformation is contemporaneous all along the profile from the PFT to the
859 Plan du Lac shear zone, i.e. over more than ca. 30km. This synchronicity of deformation
860 shows that shortening in the ECM was distributed in space and time and confirms that the
861 crust was relatively weak during shortening as proposed in Bellahsen et al. (2012). This is in
862 agreement with the formation of newly formed shear zones rather than normal faults
863 reactivation.

864 Later, shortening reached the Vercors fold and thrust belt during Burdigalian to
865 Langhian times (Fig. 13). This shortening appears linked to crustal ramps below the
866 Belledonne Massif, which suggests that the deformation localized in frontal parts after the
867 end of the main shortening phase of the ECM at around 20 Ma (Ménard, 1979; Butler, 1989;
868 Philippe et al., 1998). Between 25 and 20 Ma, the Oisans Massif has undergone fast cooling
869 at a rate of 33°C.Ma^{-1} (Crouzet et al., 2001) and was exhumed at a rate of 0.4 km.Ma^{-1} (van
870 der Beek et al., 2010). Final cooling, whose age is estimated from fission tracks ages
871 (Vernon et al., 2008), occurred after 15 Ma, which corresponds to the age of thrusting within
872 the Vercors Massif. During this more external fold and thrust belt shortening, only slight
873 deformation occurred in the Oisans Massif (Dumont et al., 2008). The new argon data
874 reported here thus complete the scenario of burial and first shortening at ca. 33 Ma,
875 progressive localisation of shear zones until 25 Ma, and final exhumation above a crustal
876 ramp until after 15-20 Ma.

877 Exhumation of the ECM was also accompanied by extensional reactivation of the PFT since
878 the late Oligocene (Tricart et al., 2007) (Fig. 13). Thus, during the late Oligocene and early
879 Miocene, the ECM was a crustal unit bordered by a normal fault to the east and a reverse
880 fault to the west, transported with low internal deformation, similarly to the models of syn-
881 collisional rock exhumation described by Chemenda et al. (1995) (Fig. 14). Moreover,
882 numerous veins witnessing for fluids circulation have been documented between 17 to 5Ma
883 in the Aar Massif (Mullis et al., 1994; Mullis, 1996; Challandes et al., 2008), in the Mont
884 Blanc Massif (Leutwein et al., 1970; Marshall et al., 1998) or in the Belledonne Massif

(Gasquet et al., 2010), indicating that this event was coeval with a fluid-rich process which affected all the orogen.

8. Conclusion

Following the description of Alpine shear zones responsible for shortening of the Oisans External Massif of the Western Alps by Bellahsen et al. (2012) and Bellanger et al. (2014), the alpine thermal structure of the massif is established here thanks to the RSCM method and the shear zones were dated. The main outcome is that the interface between the cover and the basement has recorded a maximum temperature of ~330°C, constant across the whole massif and that the shortening was accommodated by top-to-the west shear zones that progressively localized from 34 to 25 Ma, before the ECM were finally exhumed above a crustal ramp after 15-20 Ma, which in turn controlled shortening in the deformed cover further west (Vercors Massif).

Acknowledgments

This research was funded by the European Research Council (ERC) under the seventh Framework Programme of the European Union (ERC Advanced Grant, grant agreement No 290864, RHEOLITH) and has received funding from the BRGM (contract L10 U 044). We would like to thank M. Sellos and M. Vacelet for constructing discussions and for their help in the field; J.-G. Badin, S. Janiec for thin-section preparation. Y. Rolland and T. Dumont are thanked for constructive comments that greatly improved the quality of a previous manuscript.

References

Agard, P., L. Jolivet, and B. Goffe (2001), Tectonometamorphic evolution of the Schistes Lustres Complex; implications for the exhumation of HP and UHP rocks in the Western Alps, Bulletin de la Societe Geologique de France, 172(5), 617–636, doi:10.2113/172.5.617.

Agard, P., P. Monié, L. Jolivet, and B. Goffé (2002), Exhumation of the Schistes Lustrés complex: in situ laser probe 40Ar/39Ar constraints and implications for the Western Alps, Journal of Metamorphic Geology, 20(6), 599–618, doi:10.1046/j.1525-1314.2002.00391.x.

Allen, P. A., and J. R. Allen (2005), Basin analysis: principles and applications, 2nd ed., John Wiley & Sons Inc.

Angiboust, S. (2011). Couplages profonds et comportement de la lithosphère océanique dans les zones de subduction: approches pétrologiques et thermomécaniques (Doctoral dissertation, Paris 6).

Aoya, M., Y. Kouketsu, S. Endo, H. Shimizu, T. Mizukami, D. Nakamura, and S. Wallis (2010), Extending the applicability of the Raman carbonaceous-material geothermometer using data from contact metamorphic rocks, Journal of Metamorphic Geology, 28(9), 895–914, doi:10.1111/j.1525-1314.2010.00896.x.

Aprahamian, J. (1974), La cristallinité de l'illite et les minéraux argileux en bordure des massifs cristallins externes de Belledonne et du Pelvoux (Variations et relations possibles avec des événements tectoniques et métamorphiques alpins), Géologie Alpine, 50, 5–15.

Aprahamian, J. (1988), Mapping of low to very low-grade metamorphism in the External Zone of the French Alps by use of illite crystallinity index. Geodinamica Acta (Paris), 2(l), 25–32.

Augier, R., P. Agard, P. Monié, L. Jolivet, C. Robin, and G. Booth-Rea (2005), Exhumation, doming and slab retreat in the Betic Cordillera (SE Spain): in situ40Ar/39Ar ages and P–T–d–t paths for the Nevado-Filabride complex, Journal of Metamorphic Geology, 23(5), 357–381, doi:10.1111/j.1525-1314.2005.00581.x.

Baggio, P., G. Ferrara, and R. Malaroda (1967), Results of some Rb/Sr age determinations of the rocks of the Mont Blanc tunnel, Boll. Soc. Geol. Ital, 86, 193–212.

Barbier, R. (1963), La tectonique de la zone ultradauphinoise au NE du Pelvoux, Géologie Alpine, 39, 239–246.

Barbier, R., J.-C. Barféty,P. Bocquet, P. Le Fort, J. Meloux, R. Mouterde, A. Pêcher, and M. Petitteville (1973),Geological map and explanatory text of the sheet n°798 "la Grave", scale: 1:50000, ed. BRGM.

Barféty,J.-C., P. Bordet, F. Carme, J. Debelmas, M. Meloux, G. Montjuvent, R. Mouterde, and J. Sarrot-Reynauld (1972), Geological map and explanatory text of the sheet n°797 "Vizille", scale: 1:50000, ed. BRGM.

Barféty, J. C., and A. Pêcher (1984), Geological map and explanatory text of the sheet n°822 "St Christophe en Oisans," Carte géologique de la France au 1/50 000, BRGM, Orléans, France.

Barféty, J. C., J. Blaise, J.-C. Fourneaux, and J. Méloux (1984), Geological map and explanatory text of the sheet n°750 "La Rochette," Carte géologique de la France au 1/50 000, BRGM, Orléans, France.

Barféty, J. C., G. Montjuvent, A. Pêcher, and F. Carme (1988), Geological map and explanatory text of the sheet n°821 "La Mure," Carte géologique de la France au 1/50 000, BRGM, Orléans, France.

959 Barféty, J.-C., and M. Gidon (1983), La stratigraphie et la structure de la couverture
960 dauphinoise au Sud de Bourg d'Oisans. Leurs relations avec les déformations
961 synsédimentaires jurassiques, Géologie Alpine, 59, 5–32.

962 Barlier, J., J.-P. Ragot, and J.-C. Touray (1974), L'évolution des Terres noires subalpine
963 méridionales d'après l'analyse minéralogique des argiles et la réflectométrie des
964 particules carbonées., Bulletin du BRGM, 2(6), 533–548.

965 Bartoli, F., A. Pêcher, and P. Vialon (1974), Le chevauchement Meije-Muzelle et la
966 répartition des domaines structuraux alpins du massif de l'Oisans (partie Nord du
967 Haut-Dauphiné cristallin), Géologie Alpine, 50, 17–26.

968 Beach, A. (1981a), Some observations on the development of thrust faults in the
969 Ultradauphinois Zone, French Alps, Geological Society, London, Special
970 Publications, 9, 329–334, doi:10.1144/GSL.SP.1981.009.01.29.

971 Beach, A. (1981b), Thrust tectonics and cover-basement relations on the northern margin of
972 the Pelvoux massif, French Alps, Eclogae Geologicae Helvetiae, 74(2), 471–479.

973 Beach, A. (1982), Strain analysis in a cover thrust zone, external French Alps,
974 Tectonophysics, 88(3–4), 333–346, doi:10.1016/0040-1951(82)90245-1.

975 Beardsmore, G. R., & Cull, J. P. (2001). Crustal heat flow: a guide to measurement and
976 modelling. Cambridge University Press.

977 Van der Beek, P. A., P. G. Valla, F. Herman, J. Braun, C. Persano, K. J. Dobson, and E.
978 Labrin (2010), Inversion of thermochronological age-elevation profiles to extract
979 independent estimates of denudation and relief history - II: Application to the French
980 Western Alps, Earth and Planetary Science Letters, 296, 9–22.

981 Bellahsen, N., L. Jolivet, O. Lacombe, M. Bellanger, A. Boutoux, S. Garcia, F. Mouthereau,
982 L. Le Pourhiet, and C. Gumiaux (2012), Mechanisms of margin inversion in the
983 external Western Alps: Implications for crustal rheology, Tectonophysics, 560–
984 561(0), 62–83, doi:10.1016/j.tecto.2012.06.022.

985 Bellahsen, N., F. Mouthereau, A. Boutoux, M. Bellanger, O. Lacombe, L. Jolivet, and Y.
986 Rolland (2014), Collision kinematics in the western external
987 Alps, Tectonics, 33, 1055–1088, doi:10.1002/2013TC003453.

988 Bellanger, M. (2013). Raccourcissement alpin du massif des Ecrins: cinématique, calendrier
989 tectonique et conditions pression-température (Doctoral dissertation, Orléans).

990 Bellanger, M., N. Bellahsen, L. Jolivet, T. Baudin, R. Augier, and A.
991 Boutoux (2014), Basement shear zones development and shortening kinematics in
992 the Ecrins Massif, Western Alps, Tectonics, 33, 84–111,
993 doi:10.1002/2013TC003294.

994 Berger, A., and R. Bousquet (2008), Subduction-related metamorphism in the Alps: review
995 of isotopic ages based on petrology and their geodynamic consequences, Geological
996 Society, London, Special Publications, 298(1), 117–144, doi:10.1144/SP298.7.

997 Bernard, D. (1978), Microthermometrie des inclusions fluides de cristaux syn-cinematiques.
998 Application à la couverture sedimentaire du Nord Pelvoux., Univ. Grenoble, France.

999 Beucher, R. (2009), Évolution Néogène de l'Arc Alpin sud-occidental. Approches
1000 sismotectonique et thermochronologique, Univ. Joseph Fourier, Grenoble, France.

1001 Beucher, R., P. van der Beek, J. Braun, and G. E. Batt (2012), Exhumation and relief
1002 development in the Pelvoux and Dora-Maira massifs (western Alps) assessed by
1003 spectral analysis and inversion of thermochronological age transects, J. Geophys.
1004 Res., 117(F3), n/a–n/a, doi:10.1029/2011JF002240.

1005 Beyssac, O., B. Goffé, C. Chopin, and J. N. Rouzaud (2002), Raman spectra of
1006 carbonaceous material in metasediments: a new geothermometer, Journal of
1007 Metamorphic Geology, 20(9), 859–871, doi:10.1046/j.1525-1314.2002.00408.x.

1008 Beyssac, O., Bollinger, L., Avouac, J. P., & Goffé, B. (2004). Thermal metamorphism in the
1009 lesser Himalaya of Nepal determined from Raman spectroscopy of carbonaceous
1010 material. Earth and Planetary Science Letters, 225(1), 233-241.

1011 Beyssac, O., Simoes, M., Avouac, J. P., Farley, K. A., Chen, Y. G., Chan, Y. C., & Goffé,
1012 B. (2007). Late Cenozoic metamorphic evolution and exhumation of
1013 Taiwan. Tectonics, 26(6).

1014 Bigot-Cormier, F., G. Poupeau, and M. Sosson (2000), Dénudations différentielles du massif
1015 cristallin externe alpin de l'Argentera (Sud-Est de la France) révélées par
1016 thermochronologie traces de fission (apatites, zircons), Comptes Rendus de
1017 l'Académie des Sciences - Series IIA - Earth and Planetary Science, 330(5), 363–
1018 370, doi:10.1016/S1251-8050(00)00127-0.

1019 Bogdanoff, S., A. Michard, M. Mansour, and G. Poupeau (2000), Apatite fission track
1020 analysis in the Argentera massif: evidence of contrasting denudation rates in the
1021 External Crystalline Massifs of the Western Alps, Terra Nova, 12(3), 117–125,
1022 doi:10.1046/j.1365-3121.2000.123281.x.

1023 Bouillin, J.P., Pecher, A., Rolland, Y., Carrio, E., Dumont, T. and Tricart, P., (1997). Les
1024 filons sédimentaires jurassiques du Pelvoux, enregistreurs des déformations alpines
1025 de la bordure orientale du massif cristallin externe de l'Oisans (Alpes occidentales).
1026 C. R. Acad. Sci.Paris, 324, 409-415.

1027 Boullier, A.-M. (1999), Fluid inclusions: tectonic indicators, Journal of Structural Geology,
1028 21(8–9), 1229–1235, doi:10.1016/S0191-8141(99)00039-5.

1029 Boutoux, A., Bellahsen, N., Lacombe, O., Verlaguet, A., & Mouthereau, F. (2014a).
1030 Inversion of pre-orogenic extensional basins in the external Western Alps: Structure,
1031 microstructures and restoration. Journal of Structural Geology, 60, 13-29.

1032 Boutoux, A., Verlaguet, A., Bellahsen, N., Lacombe, O., Villemant, B., Caron, B., ... &
1033 Cartigny, P. (2014b). Fluid systems above basement shear zones during inversion of
1034 pre-orogenic sedimentary basins (External Crystalline Massifs, Western
1035 Alps). Lithos, accepted. DOI: 10.1016/j.lithos.2014.07.005

1036 Bravard, C., and M. Gidon (1979), La structure du revers oriental du Massif du Pelvoux:
1037 Observations et interprétations nouvelles, Géologie Alpine, 55, 23–33.Burgisser, J.,
1038 and M. Ford (1998), Overthrust shear deformation of a foreland basin; structural
1039 studies southeast of the Pelvoux massif, SE France, Journal of Structural Geology,
1040 20(11), 1455–1475.

1041 Brereton, N. R. (1970). Corrections for interfering isotopes in the $^{40}Ar/^{39}Ar$ dating
1042 method. Earth and Planetary Science Letters, 8(6), 427-433.

1043 Butler, R. W. H. (1989), The influence of pre-existing basin structure on thrust system
1044 evolution in the Western Alps, Geological Society, London, Special Publications,
1045 44(1), 105–122, doi:10.1144/GSL.SP.1989.044.01.07.

1046 Caby, R. (1973), Les plis transversaux dans les Alpes occidentales: implications pour la
1047 genèse de la chaîne alpine, Bulletin de la Société géologique de France, (5-6), 624–
1048 634.

1049 Cathelineau, M. (1988), Cation Site Occupancy in Chlorites and Illites as a Function of
1050 Temperature, Clay Minerals, 23(4), 471–485, doi:10.1180/claymin.1988.023.4.13.

1051 Cathelineau, M., and D. Nieva (1985), A chlorite solid solution geothermometer the Los
1052 Azufres (Mexico) geothermal system, Contr. Mineral. and Petrol., 91(3), 235–244,
1053 doi:10.1007/BF00413350.

1054 Cenki-Tok, B., J. R. Darling, Y. Rolland, B. Dhuime, and C. D. Storey (2013), Direct dating
1055 of mid-crustal shear zones with synkinematic allanite: new in situ U-Th-Pb
1056 geochronological approaches applied to the Mont Blanc massif, Terra Nova, n/a–n/a,
1057 doi:10.1111/ter.12066.

1058 Ceriani, S., and S. M. Schmid (2004), From n-s collision to WNW-directed post-collisional
1059 thrusting and folding: Structural study of the Frontal Penninic Units in Savoie
1060 (Western Alps, France), Eclogae Geologicae Helvetiae, 97(3), 347–369.

1061 Ceriani, S., B. Fugenschuh, and S. M. Schmid (2001), Multi-stage thrusting at the “Penninic
1062 Front” in the Western Alps between Mont Blanc and Pelvoux massifs, International
1063 Journal of Earth Sciences, 90(3), 685–702.

1064 Ceriani, S., B. Fugenschuh, S. Potel, and S. Schmid (2003), Tectono-metamorphic evolution
1065 of the Frontal Penninic units of the Western Alps: correlation between low-grade
1066 metamorphism and tectonic phases, Swiss Bulletin of Mineralogy and
1067 Petrology, 83(2), 111–131.

1068 Challandes, N., D. Marquer, and M. Villa (2008), P-T-t modelling, fluid circulation, and
1069 39Ar-40Ar and Rb-Sr mica ages in the Aar Massif shear zones (Swiss Alps), Swiss
1070 Journal of Geosciences, 101(2), 269–288, doi:10.1007/s00015-008-1260-6.

1071 Chemenda, A. I., M. Mattauer, J. Malavieille, and A. N. Bokun (1995), A mechanism for
1072 syn-collisional rock exhumation and associated normal faulting: Results from
1073 physical modelling, Earth and Planetary Science Letters, 132(1–4), 225–232,
1074 doi:10.1016/0012-821X(95)00042-B.

1075 Chopin, C. (1984), Coesite and pure pyrope in high-grade blueschists of the Western Alps: a
1076 first record and some consequences, Contr. Mineral. and Petrol., 86(2), 107–118,
1077 doi:10.1007/BF00381838.

1078 Chopin, C., and H. Maluski (1980), 40Ar-39Ar dating of high pressure metamorphic micas
1079 from the Gran Paradiso area (Western Alps): Evidence against the blocking
1080 temperature concept, Contr. Mineral. and Petrol., 74(2), 109–122,
1081 doi:10.1007/BF01131997.

1082 Clauzon, G. (1990), Genèse et évolution du piémont néogène subalpin du Bas-Dauphiné.
1083 Livret guide de l'excursion préforum du 3ème forum national de géomorphologie,
1084 Aix en Provence, Unité de recherche associé (URA) n°903 - C.N.R.S.

1085 Cliff, R. A., A. C. Barnicoat, and S. Inger (1998), Early Tertiary eclogite facies
1086 metamorphism in the Monviso Ophiolite, Journal of Metamorphic Geology, 16(3),
1087 447–455, doi:10.1111/j.1525-1314.1998.00147.x.

1088 Corna, M., J.-L. Dommergues, C. Meister & K. Page (1997) - Les faunes d'ammonites du
1089 Jurassique inférieur (Hettangien, Sinémurien et Pliensbachien) au nord du massif des
1090 Écrins (Oisans, Alpes occidentales). Revue de Paléobiologie, 16 : 321-409.

1091 Corsini, M., G. Ruffet, and R. Caby (2004), Alpine and late-hercynian geochronological
1092 constraints in the Argentera Massif (Western Alps), Eclogae geol. Helv., 97(1), 3–
1093 15, doi:10.1007/s00015-004-1107-8.

1094 Crespo-Blanc, A., H. Masson, Z. Sharp, M. Cosca, and J. Hunziker (1995), A stable and
1095 40Ar/39Ar isotope study of a major thrust in the Helvetic nappes (Swiss Alps):
1096 Evidence for fluid flow and constraints on nappe kinematics, Geological Society of
1097 America Bulletin, 107(10), 1129–1144, doi:10.1130/0016-
1098 7606(1995)107<1129:ASAAAI>2.3.CO;2.

1099 Crouzet, C., G. Menard, and P. Rochette (1999), High-precision three-dimensional
1100 paleothermometry derived from paleomagnetic data in an Alpine metamorphic unit,
1101 Geology, 27(6), 503–506.

1102 Crouzet, C., P. Rochette, and G. Menard (2001), Experimental evaluation of thermal
1103 recording of successive polarities during uplift of metasediments, Geophysical
1104 Journal International, 145(3), 771–785.

1105 Debon, F., and M. Lemmet (1999), Evolution of Mg/Fe Ratios in Late Variscan Plutonic
1106 Rocks from the External Crystalline Massifs of the Alps (France, Italy, Switzerland),
1107 Journal of Petrology, 40(7), 1151 –1185.

1108 Depardon, J. P. (1979), Les déformations de la couverture mésozoïque au Nord de l'Oisans,
1109 Université Claude Bernard - Lyon I.

1110 Deville, E., and W. Sassi (2006), Contrasting thermal evolution of thrust systems: An
1111 analytical and modeling approach in the front of the western Alps, AAPG
1112 bulletin, 90(6), 887–907.

1113 Dodson, M. H. (1973). Closure temperature in cooling geochronological and petrological
1114 systems. Contributions to Mineralogy and Petrology, 40(3), 259-274.

1115 Duchêne, S., J. Blichert-Toft, B. Luais, P. Telouk, J.-M. Lardeaux, and F. Albarede (1997),
1116 The Lu-Hf dating of garnets and the ages of the Alpine high-pressure metamorphism,
1117 Nature, 387(6633), 586–589, doi:10.1038/42446.

1118 Dumont, T. (1988). Late Triassic-early Jurassic evolution of the western Alps and of their
1119 European foreland; initiation of the Tethyan rifting. Bulletin de la Société géologique
1120 de France, 4(4), 601-611.

1121 Dumont T., 1998, Sea-level changes and early rifting of a European Tethyan margin in the
1122 Western Alps and SE France. In : Mesozoic and Cenozoic sequence stratigraphy of
1123 European basins, de Graciansky P.C., Hardenbol J., Jacquin T. & Vail P., Eds. , Soc.
1124 Econ. Petr. Geol Spec. Publ. 60, p. 623-639

1125 Dumont, T., J. D. Champagnac, C. Crouzet, and P. Rochat (2008), Multistage shortening in
1126 the Dauphine zone (French Alps): the record of Alpine collision and implications for
1127 pre-Alpine restoration, Swiss Journal of Geosciences,101(1), S89–S110.

1128 Dumont, T., T. Simon-Labric, C. Authemayou, and T. Heymes (2011), Lateral termination
1129 of the north-directed Alpine orogeny and onset of westward escape in the Western
1130 Alpine arc: Structural and sedimentary evidence from the external zone, Tectonics,
1131 30(5), TC5006.

1132 Dumont, T., S. Schwartz, S. Guillot, T. Simon-Labric, P. Tricart, and S. Jourdan (2012),
1133 Structural and sedimentary records of the Oligocene revolution in the Western
1134 Alpine arc, Journal of Geodynamics, 56, 18–38.

1135 Dunlap, W. J. (1997), Neocrystallization or cooling? 40Ar/39Ar ages of white micas from
1136 low-grade mylonites, Chemical Geology, 143(3–4), 181–203, doi:10.1016/S0009-
1137 2541(97)00113-7.

1138 Ellenberger, F. (1958), Etude géologique du pays de Vanoise (Savoie), Mémoire servant à la
1139 carte géologique de la France, BRGM.

1140 Faure, G. (1986), Principles of Isotope Geology, John Wiley & Sons.

1141 Féraud, G., G. Ruffet, J. Stéphan, H. Lapierre, E. Delgado, and M. Popoff (1995), Nouvelles
1142 données géochronologiques sur le volcanisme paléogène des Alpes occidentales:
1143 existence d'un événement magmatique bref généralisé, in Séance Spéciale de la
1144 Société géologique de France et de l" Association des Géologues du SE"
1145 Magmatismes dans le sud-est de la France", Nice, pp. 25–26.

1146 Ford, M. (1996), Kinematics and geometry of early Alpine, basement-involved folds, SW
1147 Pelvoux massif, SE France, Eclogae Geologicae Helvetiae, 89(1), 269–295.

1148 Ford, M., and W. H. Lickorish (2004), Foreland basin evolution around the western Alpine
1149 Arc, edited by P. J. Lomas and S. A. Lomas, pp. 39–63, Geological Soc Publishing
1150 House, Bath. (online) Available from: <Go to ISI>://000223880200004

1151 Du Fornel, E., P. Joseph, G. Desaubliaux, R. Eschard, F. Guillocheau, O. Lerat, C. Muller,
1152 C. Ravenne, and K. Sztràkos (2004), The southern Grès d'Annot outcrops (French
1153 Alps): an attempt at regional correlation, Geological Society, London, Special
1154 Publications, 221(1), 137–160, doi:10.1144/GSL.SP.2004.221.01.08.

1155 Le Fort, P. (1973) - Geologie du Haut-Dauphiné cristallin (Alpes Française). Etude
1156 pétrologique et structurale de la partie occidentale. - Sci. de la terre, Nancy. Mem.
1157 25, 373 p.

1158 Freeman, S. R., S. Inger, R. W. H. Butler, and R. A. Cliff (1997), Dating deformation using
1159 Rb-Sr in white mica: Greenschist facies deformation ages from the Entrelor shear
1160 zone, Italian Alps, Tectonics, 16(1), 57–76, doi:10.1029/96TC02477.

1161 Freeman, S. R., R. W. H. Butler, R. A. Cliff, S. Inger, and A. C. Barnicoat (1998),
1162 Deformation migration in an orogen-scale shear zone array: an example from the
1163 Basal Briançonnais Thrust, internal Franco-Italian Alps, Geological
1164 Magazine, 135(3), 349–367.

1165 Fry, N. (1989), Southwestward thrusting and tectonics of the western Alps, Geological
1166 Society, London, Special Publications, 45(1), 83–109.

1167 Fügenschuh, B., and S. M. Schmid (2003), Late stages of deformation and exhumation of an
1168 orogen constrained by fission-track data: A case study in the Western Alps,
1169 Geological Society of America Bulletin, 115(11), 1425–1440,
1170 doi:10.1130/B25092.1.

1171 Gabalda, S., O. Beyssac, L. Jolivet, P. Agard, and C. Chopin (2009), Thermal structure of a
1172 fossil subduction wedge in the Western Alps, Terra Nova, 21(1), 28–34,
1173 doi:10.1111/j.1365-3121.2008.00849.x.

1174 Ganne, J. (2003), Les dômes de socle HP-BT dans le domaine Pennique des Alpes Nord-
1175 Occidentales: modalité de leur exhumation., Univ. de Savoie, France.

1176 Gasquet, D., J.-M. Bertrand, J.-L. Paquette, J. Lehmann, G. Ratzov, R. D. A. Guedes, M.
1177 Tiepolo, A.-M. Boullier, S. Scaillet, and S. Nomade (2010), Miocene to Messinian
1178 deformation and hydrothermal activity in a pre-Alpine basement massif of the
1179 French western Alps: new U-Th-Pb and argon ages from the Lauziere massif,
1180 Bulletin de la Société Géologique de France, 181(3), 227–241.

1181 Gebauer, D., H.-P. Schertl, M. Brix, and W. Schreyer (1997), 35 Ma old ultrahigh-pressure
1182 metamorphism and evidence for very rapid exhumation in the Dora Maira Massif,
1183 Western Alps, Lithos, 41(1–3), 5–24, doi:10.1016/S0024-4937(97)82002-6.

1184 Gerber, W. (2008), Evolution tectono-métamorphique du Briançonnais interne (Alpes
1185 Occidentales, massifs de Vanoise Sud et d'Ambin): comportement du socle et de sa
1186 couverture dans un contexte de subduction continentale profonde, Univ. Pierre et
1187 Marie Curie, France.

1188 Gidon, M., and J.-L. Pairis (1980), Nouvelles données sur la structure des écailles de Soleil
1189 Boeuf (bordure sud du massif du Pelvoux), Bull. Bur. Rech. Geol. Min, 1, 35–41.

1190 Gratier, J. P., and P. Vialon (1980), Deformation pattern in a heterogeneous material -
1191 folded and cleaved sedimentary cover immediately overlying a crystalline basement
1192 (Oisans, French Alps), Tectonophysics, 65(1), 151–180.

1193 Gratier, J.-P., B. Lejeune, and V. Jean-Louis (1973), Etude des déformations de la
1194 couverture et des bordures sédimentaires des massifs cristallins externes de
1195 Belledonne, des Grandes Rousses et du Pelvoux (depuis des Aravis jusqu'à le région
1196 de Remollon), Université de Grenoble.

1197 Gueydan, F., Leroy, Y. M., Jolivet, L., & Agard, P. (2003). Analysis of continental
1198 midcrustal strain localization induced by microfracturing and
1199 reaction-softening. Journal of Geophysical Research: Solid Earth (1978–2012),
1200 108(B2).

1201 Guillot, S., and R. Menot (1999), Nappe stacking and first evidence of Late Variscan
1202 extension in the Belledonne Massif (External Crystalline Massifs, French Alps),
1203 Geodinamica Acta, 12(2), 97–111.

1204 Guillot, S., S. di Paola, R.-P. Ménot, P. Ledru, M. I. Spalla, G. Gosso, and S. Schwartz
1205 (2009), Suture zones and importance of strike-slip faulting for Variscan geodynamic
1206 reconstructions of the External Crystalline Massifs of the western Alps, Bulletin de
1207 la Societe Geologique de France, 180(6), 483–500, doi:10.2113/gssgfbull.180.6.483.

1208 Gupta, S., and P. A. Allen (2000), Implications of foreland paleotopography for stratigraphic
1209 development in the Eocene distal Alpine foreland basin, Geological Society of
1210 America Bulletin, 112(4), 515–530.

1211 Hames, W. E., & Bowring, S. A. (1994). An empirical evaluation of the argon diffusion
1212 geometry in muscovite. Earth and Planetary Science Letters, 124(1), 161-169.

1213 Hames, W. E., & Cheney, J. T. (1997). On the loss of 40Ar∗ from muscovite during
1214 polymetamorphism. Geochimica et Cosmochimica Acta, 61(18), 3863-3872.

1215 Harrison, T. M., J. Célérier, A. B. Aikman, J. Hermann, and M. T. Heizler (2009), Diffusion
1216 of 40Ar in muscovite, Geochimica et Cosmochimica Acta, 73(4), 1039–1051,
1217 doi:10.1016/j.gca.2008.09.038.

1218 Henry, C., Burkhard, M., & Goffe, B. (1996). Evolution of synmetamorphic veins and their
1219 wallrocks through a Western Alps transect: no evidence for large-scale fluid flow.
1220 Stable isotope, major-and trace-element systematics. Chemical Geology, 127(1), 81-
1221 109.

1222 Hurford, A. J., and J. C. Hunziker (1989), A revised thermal history for the Gran Paradiso
1223 massif, Schwei. Mineral. Petro. Mitt., 69(3), 319–329.

1224 Hurford, A. J., J. C. Hunziker, and B. Stöckhert (1991), Constraints on the late
1225 thermotectonic evolution of the western Alps: EVidence for episodic rapid uplift,
1226 Tectonics, 10(4), 758–769, doi:10.1029/91TC00167.

1227 Ivaldi, J. P., Bellon, H., Guardia, P., Mangan, C., Müller, C., Perez, J. L., & Terramorsi, S.
1228 (2003). Contexte lithostructural, âges $^{40}K/^{40}Ar$ et géochimie du volcanisme calco-
1229 alcalin tertiaire de Cap-d'Ail dans le tunnel ferroviaire de Monaco. Comptes Rendus
1230 Geoscience,335(4), 411-421.

1231 Jourdan, F., and P. R. Renne (2007), Age calibration of the Fish Canyon sanidine 40Ar/39Ar
1232 dating standard using primary K–Ar standards, Geochimica et Cosmochimica Acta,
1233 71(2), 387–402, doi:10.1016/j.gca.2006.09.002.

1234 Jullien, M., and B. Goffé (1993), Cookeite and pyrophyllite in the Dauphinois black shales
1235 (Isères, rance) : implications for the conditions of metamorphism in the Alpine
1236 external zones, Schwei. Mineral. Petro. Mitt, 73, 357–363.

1237 Kerckhove, C. (1969), La « zone du Flysch » dans les nappes de l'Embrunais-Ubaye (Alpes
1238 occidentales), Géologie Alpine, 45, 5–204.

1239 Kirschner, D. L., M. A. Cosca, H. Masson, and J. C. Hunziker (1996), Staircase 40/Ar39Ar
1240 spectra of fine-grained white mica: Timing and duration of deformation and
1241 empirical constraints on argon diffusion, Geology, 24(8), 747–750,
1242 doi:10.1130/0091-7613(1996)024<0747:SAASOF>2.3.CO;2.

1243 Kirschner, D. L., Masson, H., & Sharp, Z. D. (1999). Fluid migration through thrust faults in
1244 the Helvetic nappes (Western Swiss Alps). Contributions to Mineralogy and
1245 Petrology, 136(1-2), 169-183.

1246 Koppers, A. A. P. (2002), ArArCALC—software for 40Ar/39Ar age calculations,
1247 Computers & Geosciences, 28(5), 605–619, doi:10.1016/S0098-3004(01)00095-4.

1248 Kramar, N., M. A. Cosca, and J. C. Hunziker (2001), Heterogeneous 40Ar* distributions in
1249 naturally deformed muscovite: in situ UV-laser ablation evidence for
1250 microstructurally controlled intragrain diffusion, Earth and Planetary Science
1251 Letters, 192(3), 377–388, doi:10.1016/S0012-821X(01)00456-3.

1252 Krummenacher, D., and J. F. Evernden (1960), Déterminations d'âge isotropique faites sur
1253 quelques roches des Alpes par la méthode Potassium-Argon, Schwei. Mineral. Petro.
1254 Mitt., 40, 267-277.

1255 Lahfid, A., O. Beyssac, E. Deville, F. Negro, C. Chopin, and B. Goffé (2010), Evolution of
1256 the Raman spectrum of carbonaceous material in low-grade metasediments of the
1257 Glarus Alps (Switzerland), Terra Nova, 22(5), 354–360, doi:10.1111/j.1365-
1258 3121.2010.00956.x.

1259 Lanari, P., S. Guillot, S. Schwartz, O. Vidal, P. Tricart, N. Riel, and O. Beyssac (2012),
1260 Diachronous evolution of the alpine continental subduction wedge: Evidence from
1261 P–T estimates in the Briançonnais Zone houillère (France – Western Alps), Journal
1262 of Geodynamics, 56–57(0), 39–54, doi:10.1016/j.jog.2011.09.006.

1263 Laurent, J.-C. (1992), Les épisodes magmatiques filoniens basiques du Massif des Pelvoux-
1264 Pelvoux entre Carbonifère et Lias, Université Joseph Fourier - Grenoble 1.

1265 Leloup, P., N. Arnaud, E. Sobel, and R. Lacassin (2005), Alpine thermal and structural
1266 evolution of the highest external crystalline massif: The Mont Blanc
1267 Tectonics, 24(4), TC4002.

1268 Lemoine, M. (1972), Rythme et Modalités des Plissements Superposés dans les Chaînes
1269 Subalpines Méridionales des Alpes Occidentales Française, Geologische
1270 Rundschau, 61(3), 975–1010.

1271 Lemoine, M., and P. De Graciansky (1988), Histoire d'une marge continentale passive: les
1272 Alpes occidentales au Mésozoïque: introduction, Introduction: Bulletin de la Société
1273 Géologique de France, (8), t. IV(4), 597–600.

1274 Lemoine, M., Bas, T., Arnaud-Vanneau, A., Arnaud, H., Dumont, T., Gidon, M., ... &
1275 Tricart, P. (1986), The continental margin of the Mesozoic Tethys in the Western
1276 Alps, Marine and Petroleum Geology, 3(3), 179–199.

1277 Leutwein, F., B. Poty, J. Sonet, and J. L. Zimmerman (1970), Age des cavités à cristaux du
1278 granite du Mont Blanc, CR Acad. Sci. Paris.

1279 Malusà, M. G., R. Polino, M. Zattin, G. Bigazzi, S. Martin, and F. Piana (2005), Miocene to
1280 Present differential exhumation in the Western Alps: Insights from fission track
1281 thermochronology, Tectonics, 24(3), n/a–n/a, doi:10.1029/2004TC001782.

1282 Maluski, H., and P. Monié (1988), 40Ar-39Ar laser probe multi-dating inside single biotites
1283 of a Variscan orthogeneiss (Pinet, Massif Central, France), Chemical Geology:
1284 Isotope Geoscience section, 73(3), 245–263, doi:10.1016/0168-9622(88)90005-X.

1285 Marignac, C., M. Cathelineau, D. Bank, M.-C. Boiron, M. Ayt Ougoudal, Y. Argouarc'h,
1286 and B. Poty (1997), Alpine fault sealing at the contact between a crystalline
1287 basement and its sedimentary cover : La Gardette (French Alps). European current
1288 research on fluid 1027 inclusions. Biennial symposium No14, Nancy , FRANCE
1289 (01/07/1997), 194-195.

1290 Marshall, D., N. Meisser, and R. P. Taylor (1998), Fluid inclusion, stable isotope and Ar-Ar
1291 evidence for the age and origin of gold-bearing quartz veins at Mont Chemin,
1292 Switzerland, Mineralogy and Petrology, 62(3-4), 147–165,
1293 doi:10.1007/BF01178027.

1294 McDougall, I., and T. M. Harrison (1988), Geochronology and Thermochronology by the
1295 40Ar/39Ar Method, Oxford University Press.

1296 Meffan-Main, S., R. A. Cliff, A. C. Barnicoat, B. Lombardo, and R. Compagnoni (2004), A
1297 Tertiary age for Alpine high-pressure metamorphism in the Gran Paradiso massif,
1298 Western Alps: a Rb–Sr microsampling study, Journal of Metamorphic Geology,
1299 22(4), 267–281, doi:10.1111/j.1525-1314.2004.00512.x.

1300 Ménard, G. (1979), Relations entres structures profondes et structures superficielles dans le
1301 Sud-Est de la France. Essai d'utilisation de données Géophysiques, Université de
1302 Grenoble.

Ménard, G., and P. Rochette (1992), Utilisation de reaimantations postmetamorphiques pour une etude de l'evolution tectonique et thermique tardive dans les Alpes occidentales (France), Bulletin de la Societe Geologique de France, 163(4), 381–392.

Michard, A., T. Dumont, L. Andreani, and N. Loget (2010), Cretaceous folding in the Dévoluy mountains (Subalpine Chains, France): gravity-driven detachment at the European paleomargin versus compressional event, Bulletin de la Societe Geologique de France, 181(6), 565–581.

Min, K., R. Mundil, P. R. Renne, and K. R. Ludwig (2000), A test for systematic errors in 40Ar/39Ar geochronology through comparison with U/Pb analysis of a 1.1-Ga rhyolite, Geochimica et Cosmochimica Acta, 64(1), 73–98, doi:10.1016/S0016-7037(99)00204-5.

Monié, P., and P. Philippot (1989), 39Ar−40Ar evidence for mid-Eocene high-pressure metamorphism in the Monviso ophiolitic massif, Comptes Rendus de l'Académie des Sciences - Series 2, 309(2), 245–251.

Mulch, A., and M. A. Cosca (2004), Recrystallization or cooling ages: in situ UV-laser 40Ar/39Ar geochronology of muscovite in mylonitic rocks, Journal of the Geological Society, 161(4), 573–582, doi:10.1144/0016-764903-110.

Mulch, A., M. Cosca, and M. Handy (2002), In-situ UV-laser 40Ar/39Ar geochronology of a micaceous mylonite : an example of defect-enhanced argon loss, Contrib Mineral Petrol, 142(6), 738–752, doi:10.1007/s00410-001-0325-6.

Mulch, A., M. A. Cosca, A. Andresen, and J. Fiebig (2005), Time scales of deformation and exhumation in extensional detachment systems determined by high-spatial resolution in situ UV-laser 40Ar/39Ar dating, Earth and Planetary Science Letters, 233(3–4), 375–390, doi:10.1016/j.epsl.2005.01.042.

Mulder, T., Callec, Y., Parize, O., Joseph, P., Schneider, J. L., Robin, C., ... & Zaragosi, S. (2010). High-resolution analysis of submarine lobes deposits: Seismic-scale outcrops of the Lauzanier area (SE Alps, France). Sedimentary Geology, 229(3), 160-191., doi:10.1016/j.sedgeo.2009.11.005.

Müller, W. (2003), Strengthening the link between geochronology, textures and petrology, Earth and Planetary Science Letters, 206(3–4), 237–251, doi:10.1016/S0012-821X(02)01007-5.

Mullis, J. (1996), P-T-t path of quartz formation in extensional veins of the Central Alps, Schwei. Mineral. Petro. Mitt., 76, 159–164.

Mullis, J., J. Dubessy, B. Poty, and J. O'Neil (1994), Fluid regimes during late stages of a continental collision: Physical, chemical, and stable isotope measurements of fluid inclusions in fissure quartz from a geotraverse through the Central Alps, Switzerland, Geochimica et Cosmochimica Acta, 58(10), 2239–2267, doi:10.1016/0016-7037(94)90008-6.

Negro, F., Beyssac, O., Goffé, B., Saddiqi, O., & Bouybaouene, M. L. (2006). Thermal structure of the Alboran Domain in the Rif (northern Morocco) and the Western

Betics (southern Spain). Constraints from Raman spectroscopy of carbonaceous material. Journal of Metamorphic Geology, 24(4), 309-327.

Nziengui, J.-J. (1993), Excès d'argon radiogénique dans les quartz des fissures tectoniques : implications pour la datation des séries métamorphiques. L'exemple de la coupe de la Romanche, Alpes Occidentales françaises, Univ. Joseph Fourier, Grenoble, France.

Pfiffner, A. (1992), Alpine orogeny, D. Blundell, R. Freeman and St. Mliller (Editors), A Continent Revealed: The European Geotraverse. Cambridge University Press, Cambridge, 180–190.

Philippe, Y., E. Deville, and A. Mascle (1998), Thin-skinned inversion tectonics at oblique basin margins: example of the western Vercors and Chartreuse Subalpine massifs (SE France), Geological Society, London, Special Publications, 134(1), 239–262, doi:10.1144/GSL.SP.1998.134.01.11.

Plunder, A., P. Agard, B. Dubacq, C. Chopin, and M. Bellanger (2012), How continuous and precise is the record of P–T paths? Insights from combined thermobarometry and thermodynamic modelling into subduction dynamics (Schistes Lustrés, W. Alps), Journal of Metamorphic Geology, 30(3), 323–346, doi:10.1111/j.1525-1314.2011.00969.x.

Von Raumer, J., J. Abrecht, F. Bussy, B. Lombardo, R. Ménot, and U. Schaltegger (1999), The Palaeozoic metamorphic evolution of the Alpine external massifs, Schweiz. mineral. petrogr. Mitt, 79(1), 5–22.

Reddy, S. M., Kelley, S. P., & Wheeler, J. (1996). A 40Ar/39Ar laser probe study of micas from the Sesia Zone, Italian Alps: implications for metamorphic and deformation histories. Journal of Metamorphic Geology, 14(4), 493-508.

Renne, P. R., C. C. Swisher, A. L. Deino, D. B. Karner, T. L. Owens, and D. J. DePaolo (1998), Intercalibration of standards, absolute ages and uncertainties in 40Ar/39Ar dating, Chemical Geology, 145(1–2), 117–152, doi:10.1016/S0009-2541(97)00159-9.

Riche, P., and P. Trémolières (1987), Tectonique synsédimentaire sur la bordure orientale du bassin tertiaire de Valreas, Géologie Alpine, Mémoire H.S., 13, 409–416.

Rolland, Y., M. Rossi, S. F. Cox, M. Corsini, N. Mancktelow, G. Pennacchioni, M. Fornari, and A. M. Boullier (2008), 40Ar/39Ar dating of synkinematic white mica: insights from fluid-rock reaction in low-grade shear zones (Mont Blanc Massif) and constraints on timing of deformation in the NW external Alps, Geological Society, London, Special Publications, 299(1), 293–315, doi:10.1144/SP299.18.

Rolland, Y., S. F. Cox, and M. Corsini (2009), Constraining deformation stages in brittle-ductile shear zones from combined field mapping and Ar-40/Ar-39 dating: The structural evolution of the Grimsel Pass area (Aar Massif, Swiss Alps), Journal of Structural Geology, 31, 1377–1394.

1382 Rosenbaum, G., and G. S. Lister (2005), The Western Alps from the Jurassic to Oligocene:
1383 spatio-temporal constraints and evolutionary reconstructions, Earth-Science
1384 Reviews, 69(3–4), 281–306, doi:10.1016/j.earscirev.2004.10.001.

1385 Roux, M., J.-P. Bourseau, T. Bas, T. Dumont, P.-C. de Graciansky, M. Lemoine, and J.-L.
1386 Rudkiewicz (1988), Bathymetric evolution of the Tethyan margin in the western
1387 Alps (data from stalked crinoids): a reappraisal of eustatism problems during the
1388 Jurassic, Bulletin de la Société géologique de France, 4(4), 633–641.

1389 Rubatto, D., and J. Hermann (2001), Exhumation as fast as subduction?, Geology, 29(1), 3–
1390 6, doi:10.1130/0091-7613(2001)029<0003:EAFAS>2.0.CO;2.

1391 Rubatto, D., and J. Hermann (2003), Zircon formation during fluid circulation in eclogites
1392 (Monviso, Western Alps): implications for Zr and Hf budget in subduction zones,
1393 Geochimica et Cosmochimica Acta, 67(12), 2173–2187, doi:10.1016/S0016-
1394 7037(02)01321-2.

1395 Ruffini, R., R. Polino, E. Callegari, J. Hunziker, and H. Pfeifer (1997), Volcanic clast-rich
1396 turbidites of the Tavayanne sandstones from the Thone syncline (Savoie, France):
1397 records for a tertiary postcollisional volcanism, Schweiz. Miner. Petrogr. Mitt, 77,
1398 161–174.

1399 Sabil, N. (1995), La datation par traces de fission: aspects méthodologiques et applications
1400 thermochronologique en contexte Alpin et de Marge Continentale., Univ. Joseph
1401 Fourier, Grenoble, France.

1402 Salles, L., M. Ford, P. Joseph, C. Le Carlier De Veslud, and A. Le Solleuz (2011), Migration
1403 of a synclinal depocentre from turbidite growth strata: the Annot syncline, SE
1404 France, Bulletin de la Societe Geologique de France, 182(3), 199–220.

1405 Saliot, P. (1973). Les principales zones de métamorphisme dans les Alpes françaises.
1406 Répartition et signification. CR Acad. Sci. Paris, 276, 3081-3084.

1407 Sanchez, G., Y. Rolland, J. Schneider, M. Corsini, E. Oliot, P. Goncalves, C. Verati, J.-M.
1408 Lardeaux, and D. Marquer (2011a), Dating low-temperature deformation by
1409 40Ar/39Ar on white mica, insights from the Argentera-Mercantour Massif (SW
1410 Alps), Lithos, 125(1), 521–536.

1411 Sanchez, G., Y. Rolland, M. Jolivet, S. Brichau, M. Corsini, and A. Carter (2011b),
1412 Exhumation controlled by transcurrent tectonics: the Argentera-Mercantour massif
1413 (SW Alps), Terra Nova, 23(2), 116–126.

1414 Scaillet, S., G. Féraud, Y. Lagabrielle, M. Ballévre, and G. Ruffet (1990), 40Ar/39Ar laser-
1415 probe dating by step heating and spot fusion of phengites from the Dora Maira nappe
1416 of the western Alps, Italy, Geology, 18(8), 741–744, doi:10.1130/0091-
1417 7613(1990)018<0741:AALPDB>2.3.CO;2.

1418 Scaillet, S., G. Feraud, M. Ballevre, and M. Amouric (1992), MgFe and ((Mg,Fe)Si-Al2)
1419 compositional control on argon behaviour in high-pressure white micas: A 40Ar39Ar
1420 continuous laser-probe study from the Dora-Maira nappe of the internal western
1421 Alps, Italy, Geochimica et Cosmochimica Acta, 56(7), 2851–2872,
1422 doi:10.1016/0016-7037(92)90364-O.

1423 Schaeffer, O., H. W. Mueller, and T. L. Grove (1977), Laser Ar-39-Ar-40 study of Apollo
1424 17 basalts, vol. Proceedings. Volume 2. (A78-41551 18-91), New York, Pergamon,
1425 Houston.

1426 Schwartz, S., J. M. Lardeaux, P. Tricart, S. Guillot, and E. Labrin (2007), Diachronous
1427 exhumation of HP-LT metamorphic rocks from south-western Alps: evidence from
1428 fission-track analysis, Terra Nova, 19(2), 133–140.

1429 Seward, D., and N. S. Mancktelow (1994), Neogene kinematics of the central and western
1430 Alps: Evidence from fission-track dating, Geology, 22(9), 803–806,
1431 doi:10.1130/0091-7613(1994)022<0803:NKOTCA>2.3.CO;2.

1432 Simon-Labric, T., Y. Rolland, T. Dumont, T. Heymes, C. Authemayou, M. Corsini, and M.
1433 Fornari (2009), Ar-40/Ar-39 dating of Penninic Front tectonic displacement (W
1434 Alps) during the Lower Oligocene (31-34 Ma), Terra Nova,21(2), 127–136.

1435 Sinclair, H. D. (1997), Tectonostratigraphic model for underfilled peripheral foreland
1436 basins: An Alpine perspective, Geological Society of America Bulletin, 109(3), 324–
1437 346, doi:10.1130/0016-7606(1997)109<0324:TMFUPF>2.3.CO;2.

1438 Strzerzynski, P., S. Guillot, P. H. Leloup, N. Arnaud, O. Vidal, P. Ledru, G. Courrioux, and
1439 X. Darmendrail (2012), Tectono-metamorphic evolution of the Briançonnais zone
1440 (Modane-Aussois and Southern Vanoise units, Lyon Turin transect, Western Alps),
1441 Journal of Geodynamics, 56–57(0), 55–75, doi:10.1016/j.jog.2011.11.010.

1442 Tilton, G. R., W. Schreyer, and H.-P. Schertl (1991), Pb−Sr−Nd isotopic behavior of deeply
1443 subducted crustal rocks from the Dora Maira Massif, Western Alps, Italy-II: what is
1444 the age of the ultrahigh-pressure metamorphism?, Contr. Mineral. and Petrol., 108(1-
1445 2), 22–33, doi:10.1007/BF00307323.

1446 Tricart, P., S. Schwartz, C. Sue, G. Poupeau, and J.-M. Lardeaux (2001), La denudation
1447 tectonique de la zone ultradauphinoise et l'inversion du front brianconnais au sud-est
1448 du Pelvoux (Alpes occidentales); une dynamique miocene a actuelle, Bulletin de la
1449 Societe Geologique de France, 172(1), 49–58, doi:10.2113/172.1.49.

1450 Tricart, P., S. Schwartz, C. Sue, and J.-M. Lardeaux (2004), Evidence of synextension tilting
1451 and doming during final exhumation from analysis of multistage faults (Queyras
1452 Schistes lustrés, Western Alps), Journal of Structural Geology, 26(9), 1633–1645,
1453 doi:10.1016/j.jsg.2004.02.002.

1454 Tricart, P., J.-M. Lardeaux, S. Schwartz, and C. Sue (2006), The late extension in the inner
1455 western Alps: a synthesis along the south-Pelvoux transect, Bulletin de la Societe
1456 Geologique de France, 177(6), 299–310, doi:10.2113/gssgfbull.177.6.299.

1457 Tricart, P., P. Van der Beek, S. Schwartz, and E. Labrin (2007), Diachronous late-stage
1458 exhumation across the western Alpine arc: constraints from apatite fission-track
1459 thermochronology between the Pelvoux and Dora-Maira Massifs, Journal of the
1460 Geological Society, 164(1), 163–174.

1461 Turrillot, P., Augier, R., Monié, P., & Faure, M. (2011). Late orogenic exhumation of the
1462 Variscan high-grade units (South Armorican Domain, western France), combined
1463 structural and 40Ar/39Ar constraints. Tectonics, 30(5).

1464 Vernon, A. J., Van Der Beek, P. A., Sinclair, H. D., & Rahn, M. K. (2008). Increase in late
1465 Neogene denudation of the European Alps confirmed by analysis of a fission-track
1466 thermochronology database. Earth and Planetary Science Letters, 270(3), 316-329.

1467 Vidal, O., T. Parra, and F. Trotet (2001), A Thermodynamic Model for Fe-Mg Aluminous
1468 Chlorite Using Data from Phase Equilibrium Experiments and Natural Pelitic
1469 Assemblages in the 100° to 600°c, 1 to 25 kb Range, American Journal of Science,
1470 301(6), 557–592, doi:10.2475/ajs.301.6.557.

1471 Vidal, O., T. Parra, and P. Vieillard (2005), Thermodynamic properties of the Tschermak
1472 solid solution in Fe-chlorite: Application to natural examples and possible role of
1473 oxidation, American Mineralogist, 90(2-3), 347–358, doi:10.2138/am.2005.1554.

1474 Vidal, O., V. De Andrade, E. Lewin, M. Munoz, T. Parra, and S. Pascarelli (2006), P–T-
1475 deformation-Fe3+/Fe2+ mapping at the thin section scale and comparison with
1476 XANES mapping: application to a garnet-bearing metapelite from the Sambagawa
1477 metamorphic belt (Japan), Journal of Metamorphic Geology, 24(7), 669–683,
1478 doi:10.1111/j.1525-1314.2006.00661.x.

1479 Villa, I. M. (1998). Isotopic closure. Terra Nova-Oxford, 10(1), 42-47.

1480 Vitale Brovarone, A., Beyssac, O., Malavieille, J., Molli, G., Beltrando, M., & Compagnoni,
1481 R. (2013). Stacking and metamorphism of continuous segments of subducted
1482 lithosphere in a high-pressure wedge: the example of Alpine Corsica (France). Earth-
1483 Science Reviews, 116, 35-56.

1484 Waibel, A. F. (1990), Sedimentology, petrographic variability and very-low-garde
1485 metamorphism of the Champsaur sandstone (Paleogene, Hautes-Alpes, France).
1486 Evolution of Volcaniclastic Foreland Turbidites in the External Western Alps., Univ.
1487 Genève, Switzerland.

1488 West, D. P., and D. R. Lux (1993), Dating mylonitic deformation by the 40Ar-39Ar method:
1489 An example from the Norumbega Fault Zone, Maine, Earth and Planetary Science
1490 Letters, 120(3–4), 221–237, doi:10.1016/0012-821X(93)90241-Z.

1491 De Wever, P., and R. Caby (1981), Datation de la base des schistes lustrés
1492 postophiolithiques par des radiolaires (Oxfordien supérieur? Kimmeridgien moyen)
1493 dans les Alpes Cottiennes (Saint Véran, France), Comptes Rendus de l'Academie des
1494 Sciences, 292, 467–472.

1495 De Wever, P., T. Danelian, M. Durand-Delga, F. Cordey, and N. Kito (1987), Datations des
1496 radiolarites post-ophiolitiques de Corse alpine à l'aide des Radiolaires, CR Acad.
1497 Sci. Paris, 305, 893–900.

1498 Wibberley, C. (1999), Are feldspar-to-mica reactions necessarily reaction-softening
1499 processes in fault zones?, Journal of Structural Geology, 21(8), 1219–1227.

1500 Wibberley, C. A. . (2005), Initiation of basement thrust detachments by fault-zone reaction
1501 weakening, Geological Society, London, Special Publications, 245, 347–372.

1502 Wijbrans, J. R., & McDougall, I. (1986). 40Ar/39Ar dating of white micas from an Alpine
1503 high-pressure metamorphic belt on Naxos (Greece): the resetting of the argon
1504 isotopic system. Contributions to Mineralogy and Petrology, 93(2), 187-194.

1505 York, D. (1968), Least squares fitting of a straight line with correlated errors, Earth and
1506 Planetary Science Letters, 5(0), 320–324, doi:10.1016/S0012-821X(68)80059-7.

1507 York, D., C. M. Hall, Y. Yanase, J. A. Hanes, and W. J. Kenyon (1981), 40Ar/39Ar dating
1508 of terrestrial minerals with a continuous laser, Geophys. Res. Lett., 8(11), 1136–
1509 1138, doi:10.1029/GL008i011p01136.

1510

1511 **Figure captions**

1512

1513 Figure 1: (a) Large-scale tectonic map of the Western Alps. Indicated is the location of the
1514 figure 2 that embraces the whole studied area. (b) Geological cross-section across the
1515 studied area close to the 45th parallel modified from Bellanger et al. (2014).

1516

1517 Figure 2: Simplified structural map of the studied area modified from Bellanger et al.
1518 (2014). Indicated is the location of the studied samples either form the Mesozoic cover for
1519 RSCM and chlorite geothermometry or from the basement shear zones for chlorite
1520 geothermometry and for the $^{40}Ar/^{39}Ar$ *in situ* approach. See tables for precise locations of
1521 samples.

1522

1523 Figure 3: Deformation features of the Oisans Massif at decreasing scales. (a) kilometer-scale
1524 view as illustrated by a geological cross-section from the Penninic Frontal Thrust (PFT) to
1525 La Mure Massif. Note the distribution of the Alpine shear zones and the overall eastward
1526 increasing of the finite strain intensity; (b) landscape-scale view as illustrated by a picture of
1527 a part of the Plan du Lac shear zone in the Vénéon Valley. Note the anastomosed
1528 relationships of the shear planes, the folded shape of the basement-cover interface and the
1529 pinched part of Mesozoic cover. Field-sketch diagrams represent macroscopic features of

the deformation from mylonite to phyllonite at outcrop-scale. (c) Thin-section pictures showing small-scale deformation features of from proto-mylonite to phyllonite strain-stage. Note the clear increase of the phengite fraction with strain increasing.

Figure 4: First-order results from the Raman Spectrometry of Carbonaceous Material approach. (a) RSCM Map showing mapping of the T_{max} results and inferred isotherms. The isotherm shape was drawn from interpolated map and from the distribution of the Illite crystallinity; (b) Illite crystallinity map modified from Aprahamian (1974) and Barlier et al. (1974). (c) Projection of the RSCM Tmax over a classical E-W cross-section from the west of the Belledonne Massif to the Penninic Frontal Thrust. (d and e) RSCM Tmax results vs. longitude and elevation along the cross-section (c). Data represented with smaller symbols to the east of the Penninic Frontal Thrust come from Beyssac et al. (2002); Gabalda et al. (2009); Lanari et al. (2012) and Plunder et al. (2012). Detailed results are given in table 1.

Figure 5: Local-scale features of results from the Raman Spectrometry of Carbonaceous Material approach. (a) Distribution of the Tmax to the west of the Belledonne Massif from RSCM (circle) and vitrinite reflectance results (star; data from Deville and Sassi (2006) transformed into temperatures using the equation proposed in Allen and Allen (2005). The distribution of the Tmax in the sedimentary pile is aligned along a ca. 30-50°C.km^{-1} gradient. Besides, temperature gaps across narrow zones highlight localized tectonic contacts. (b) Distribution of the RSCM Tmax results close to the Lautaret and Galibier passes. The structural data come from Depardon (1979), Beach (1981a, 1982), Ceriani et al. (2001), and Bellanger (2013). Note that the distribution of the Tmax within the tectonic pile is consistent with a ca. 20-30°C.km^{-1} post-tectonic field gradient. Detailed results are given in table 1.

Figure 6: Chlorite composition and results from chlorite geothermometry the Mesozoic cover. (a) XMg *vs.* Silica content diagram. (b) Clinochlore/Amesite/Sudoite ternary plot. Note that chlorite composition is first controlled by the bulk composition of the protolith. (c) Internal consistency of the geothermometric results. Chlorite geothermometry results using

both thermodynamic and empirical approaches (Cathelineau and Nieva, 1985, Vidal et al., 2005, 2006) are compared to RSCM data. Chlorite probably records a part of the cooling (retrograde) evolution. Detailed results are given in table 2.

Figure 7: Example of microstructural and composition of sample A.4.64 used as a guideline for dated samples. (a) Contrasted habits of white-micas as seen on several close-up views from the same thin-section. (b) White-mica chemical composition in ternary plots and XMg *vs.* Silica content diagram. Fine-grained, often syn-kinematic white-micas present in C-type and S-type foliation have phengite compositions. Well-developed white-mica clasts have a muscovite composition.

Figure 8: White-micas composition and chlorite geothermometry from dated samples (basement shear zones). For each of the dated shear zone, presented is the composition of white-micas as a function to their textural position in Si *vs*. Na content diagram and Muscovite/Celadonite/Pyrophyllite ternary plot together with results of chlorite geothermometry using both thermodynamic and empirical approaches (Cathelineau and Nieva, 1985, Vidal et al., 2001, 2005, 2006). Detailed results are given in table 2. (a) corresponds to results for the Col de Cluy shear zone while (b), (c) and (d) correspond to Plan du Lac, Col du Lac and Combeynot shear zones, respectively. Due to a very poor dataset, results for the Combeynot shear zone are not shown.

Figure 9: Time-chart showing all results of the *in situ* $^{40}Ar/^{39}Ar$ approach. Detailed results are given in table 3. Stratigraphic age for the Nummulitic flysch deposit is from Mulder et al. (2010); zircon and apatite fission-tracks results from Van der Beek et al. (2010).

Figure 10: Pictures showing the distribution of *in situ* laser ablation of the $^{40}Ar/^{39}Ar$ approach. Note the overall dependency of the K/Ar system to the finite strain intensity. Detailed results are given in table 3.

Figure 11: Pressure-Temperature-deformation-time evolution of the Oisans Massif. (a) Pressure-Temperature (P-T) constraints for the Oisans Massif. The P-T data come from (Gratier et al., 1973; Bernard, 1978) and references therein (Thermobarometry from fluids inclusions and paragenesis from cover and basement veins), (Jullien and Goffé, 1993) (conventional metamorphic petrology from the Emparis basin Mesozoic cover, (Crouzet et al., 1999) (thermopaleomagnetism from the Bourg d'Oisans basin), (Ceriani et al., 2003) (Zircon fission track and Kübler index and b-cell dimension of white mica fom the Nummulitic cover of the Cheval noir unit), this study (RSCM from Mesozoic and Nummulitic cover). Temperature-deformation-time (T-d-t) constraints for the Oisans Massif. The T-d-t data come from (1) (Nziengui, 1993); (2) (Jullien and Goffé, 1993); (3) this study; (4) (Crouzet et al., 1999); (5) (Ménard and Rochette, 1992); (6) (Crouzet et al., 2001); (7) (van der Beek et al., 2010); (8) (Sabil, 1995; van der Beek et al., 2010; Beucher et al., 2012).

Figure 12: Large-scale compilation of existing time-constraints for the External zone and for the Western Alps close to the 45th parallel. (1) (Riche and Trémolières, 1987) (2) (Clauzon, 1990) (3) (Philippe et al., 1998) (4) (Du Fornel et al., 2004) (5) (Mulder et al., 2010) (6) (Féraud et al., 1995) (7) (Marignac et al., 1997) (8) (Gasquet et al., 2010) (9) (Simon-Labric et al., 2009) (a: Combeynot sinistral strike-slip shear zone; b: Pelvoux dextral strike-slip shear zone; c: Ailefroide dextral strike-slip shear zone); (10) this study; (11) (Nziengui, 1993) (12) (Crouzet et al., 1999, 2001) (13) (van der Beek et al., 2010) (14) (Sabil, 1995; van der Beek et al., 2010; Beucher et al., 2012) (15-16) (Fügenschuh and Schmid, 2003) (17) (Ceriani and Schmid, 2004) (18) (Ceriani et al., 2003; Fügenschuh and Schmid, 2003) (19) (Fügenschuh and Schmid, 2003) (20) (Féraud et al., 1995) (21) (Corsini et al., 2004) (22) (Sanchez et al., 2011a) (23) (Bigot-Cormier et al., 2000) (24) (Bigot-Cormier et al., 2000; Bogdanoff et al., 2000; Sanchez et al., 2011b) (25) (Pfiffner, 1992) (26) (Ruffini et al., 1997) (27-29) (Leutwein et al., 1970) (30) (Marshall et al., 1998) (31) (Crespo-Blanc et al., 1995) (32) (Kirschner et al., 1996) (33-34) (Rolland et al., 2008) (35) (Krummenacher and Evernden, 1960) (36) (Leutwein et al., 1970) (37-40) (Leloup et al., 2005) (41) (Baggio et al., 1967) (42-43) (Seward and Mancktelow, 1994; Leloup et al., 2005) (44-45) (Fügenschuh and Schmid, 2003) (46) (Freeman et al., 1998) (47) (Beucher, 2009) (48-49) (Fügenschuh and Schmid, 2003; Tricart et al., 2007) (50) (Ellenberger, 1958) (51) (Ganne, 2003) (52) (Gerber, 2008) (53) (Malusà et al., 2005) (54-56) (Ganne, 2003) (57-61) (Gerber, 2008) (62)

(Strzerzynski et al., 2012) (63) (Freeman et al., 1997) (64) (Agard et al., 2002) (65) (Duchêne et al., 1997) (66) (Rubatto and Hermann, 2003) (67) (Monié and Philippot, 1989) (68-69) (Cliff et al., 1998) (70-71) (Schwartz et al., 2007; Tricart et al., 2007; Beucher, 2009) (72) (Agard et al., 2002) (73) (Duchêne et al., 1997) (74) (Gebauer et al., 1997) (75) (Rubatto and Hermann, 2001) (76 et 78) (Tilton et al., 1991) (77) (Scaillet et al., 1992) (79) (Gebauer et al., 1997) (80) (Beucher et al., 2012) (81 et 83) (Chopin and Maluski, 1980) (82) (Ganne, 2003) (84) (Meffan-Main et al., 2004) (85-86) (Hurford and Hunziker, 1989; Hurford et al., 1991).

Figure 13: Lithospheric reconstructions of the Alps along a cross-section close to the 45th parallel. See text for explanations.

Table captions

Table 1: Detailed results from the RSCM approach. Given are the GPS position (latitude (Lat.) and longitude (Long.) in decimal degrees (WGS84) and the elevation in meter), the tectonic unit, the stratigraphic age, the lithology, the number of Raman spectra (Sp.), the R2 or the RA1 ratio, the RSCM temperature (mean and standard deviation). R2 ratio, in regular font (Beyssac et al., 2002) or the RA1 ratio, in italic font (Lahfid et al. 2010) was preferred depending on the shape of the spectra and the presence of the D4 peak (Lahfid et al., 2010).

Table 2: Detailed results from the chlorite geothermometry approach. Given are the GPS position (latitude (Lat.) and longitude (Long.) in decimal degrees (WGS84) and results of thermodynamic and empirical approaches (Cathelineau and Nieva, 1985, Vidal et al., 2005, 2006). Results are presented separately for the Mesozoic cover and the basement (Alpine shear zones).

Table 3: Detailed results from the $^{40}Ar/^{39}Ar$ approach. Given are the GPS position (latitude (Lat.) and longitude (Long.) in decimal degrees (WGS84) in decimal degrees (WGS84) and different output isotopic ratio.

	182	*26.68*	*± 0.86*	*5.52*	*0.09*	*16.617*	*31.735*	*5.459*	*20*	
	184	*27.25*	*± 0.70*	*5.64*	*0.07*	*13.268*	*74.860*	*3.342*	*13*	
	185	*37.15*	*± 0.98*	*7.71*	*0.10*	*16.231*	*17.350*	*5.288*	*15*	
	186	*32.60*	*± 0.78*	*6.75*	*0.08*	*15.331*	*28.381*	*3.749*	*12*	
	188	*23.22*	*± 0.57*	*4.80*	*0.06*	*14.716*	*0.397*	*2.635*	*12*	
	189	*26.87*	*± 0.71*	*5.56*	*0.07*	*14.822*	*3.060*	*3.589*	*14*	
	190	*33.63*	*± 3.54*	*6.97*	*0.37*	*20.026*	*14.646*	*30.393*	*53*	
	192	*34.59*	*± 3.37*	*7.17*	*0.35*	*20.946*	*10.029*	*28.806*	*51*	
	193	*32.12*	*± 1.04*	*6.65*	*0.11*	*17.515*	*17.526*	*7.044*	*21*	
	194	*26.78*	*± 3.41*	*5.54*	*0.36*	*24.354*	*10.163*	*29.142*	*57*	
	196	*28.71*	*± 3.55*	*5.94*	*0.37*	*19.039*	*0.466*	*30.419*	*56*	
	197	*30.02*	*± 2.49*	*6.22*	*0.26*	*19.316*	*27.056*	*20.857*	*46*	
	198	*28.68*	*± 1.10*	*5.93*	*0.11*	*15.174*	*13.405*	*7.848*	*25*	
	200	*35.20*	*± 2.99*	*7.30*	*0.31*	*19.635*	*14.784*	*25.369*	*47*	
	201	*25.89*	*± 0.76*	*5.35*	*0.08*	*14.485*	*16.121*	*3.516*	*14*	***44***
A-4-68b (Ech5)	79	*101.14*	*± 2.19*	*21.36*	*0.24*	*19.325*	*21.345*	*8.756*	*10*	
Plan du Lac	80	*26.78*	*± 0.62*	*5.54*	*0.06*	*14.705*	*7.379*	*2.725*	*11*	
Gneiss	82	*25.90*	*± 0.52*	*5.35*	*0.05*	*13.112*	*5.208*	*0.772*	*3*	
Lat.: 44.984950°	83	*101.52*	*± 4.58*	*21.44*	*0.50*	*36.434*	*26.990*	*37.570*	*33*	
Lon.: 6.143560°	85	*87.86*	*± 3.53*	*18.48*	*0.38*	*30.597*	*18.766*	*27.850*	*30*	
	86	*114.24*	*± 4.28*	*24.21*	*0.47*	*32.663*	*43.649*	*33.490*	*28*	
	88	*57.58*	*± 1.80*	*12.01*	*0.19*	*19.509*	*20.365*	*12.438*	*22*	
	89	*59.11*	*± 1.88*	*12.34*	*0.20*	*22.043*	*10.178*	*13.115*	*23*	
	91	*65.70*	*± 2.07*	*13.74*	*0.22*	*23.431*	*8.778*	*14.399*	*22*	
	92	*96.56*	*± 2.86*	*20.36*	*0.31*	*25.972*	*15.399*	*19.551*	*21*	
	94	*52.37*	*± 1.65*	*10.91*	*0.17*	*22.259*	*6.778*	*11.386*	*22*	
	95	*102.17*	*± 2.88*	*21.58*	*0.31*	*27.804*	*9.330*	*18.937*	*20*	
	96	*37.80*	*± 1.17*	*7.84*	*0.12*	*18.793*	*2.915*	*7.892*	*21*	
	98	*38.11*	*± 0.99*	*7.91*	*0.10*	*12.649*	*108.017*	*5.226*	*15*	
	99	*27.07*	*± 0.61*	*5.60*	*0.06*	*15.396*	*1.553*	*2.420*	*10*	
	101	*37.89*	*± 0.99*	*7.86*	*0.10*	*17.127*	*0.000*	*5.366*	*15*	
	102	*42.32*	*± 1.06*	*8.79*	*0.11*	*18.704*	*16.415*	*5.553*	*14*	
	104	*71.99*	*± 1.71*	*15.08*	*0.18*	*20.856*	*38.529*	*6.467*	*11*	
	105	*49.19*	*± 1.09*	*10.24*	*0.11*	*15.637*	*22.946*	*3.927*	*9*	
	107	*57.58*	*± 1.30*	*12.01*	*0.14*	*17.453*	*18.965*	*5.279*	*11*	
	108	*61.32*	*± 1.35*	*12.80*	*0.14*	*17.214*	*6.628*	*5.273*	*10*	***21***
										65

Table 3

	317	*159.84*	*± 9.51*	*34.09*	*1.06*	*42.598*	*100.620*	*81.736*	*41*	
	318	*83.59*	*± 2.05*	*17.45*	*0.22*	*19.188*	*33.359*	*10.534*	*14*	
	319	*116.28*	*± 2.50*	*24.50*	*0.27*	*19.849*	*18.212*	*8.634*	*9*	
	320	*89.33*	*± 2.20*	*18.68*	*0.24*	*19.482*	*126.785*	*6.793*	*9*	***40***
A-4-66b	19	*37.78*	*± 3.17*	*7.79*	*0.33*	*21.743*	*41.626*	*26.734*	*47*	
Plan du Lac	20	*37.63*	*± 2.03*	*7.76*	*0.21*	*19.494*	*7.915*	*16.086*	*35*	
Gneiss	26	*38.95*	*± 1.54*	*8.03*	*0.16*	*15.253*	*0.760*	*11.468*	*27*	
Lat.: 44.982410°	27	*36.87*	*± 2.03*	*7.60*	*0.21*	*17.892*	*2.116*	*16.419*	*36*	
Lon.: 6.147040°	29	*301.42*	*± 6.56*	*66.91*	*0.79*	*35.325*	*0.000*	*34.137*	*13*	
	30	*62.29*	*± 1.41*	*12.93*	*0.15*	*16.109*	*16.173*	*6.088*	*11*	
	33	*129.05*	*± 3.03*	*27.29*	*0.33*	*27.668*	*8.263*	*15.628*	*14*	
	34	*36.00*	*± 0.98*	*7.42*	*0.10*	*12.959*	*0.000*	*5.512*	*16*	
	37	*35.72*	*± 1.89*	*7.36*	*0.20*	*22.241*	*35.724*	*14.517*	*34*	
	39	*32.67*	*± 1.63*	*6.73*	*0.17*	*17.296*	*12.892*	*12.831*	*33*	
	40	*32.08*	*± 1.10*	*6.60*	*0.11*	*14.308*	*7.733*	*7.737*	*23*	
	42	*30.72*	*± 1.09*	*6.32*	*0.11*	*14.967*	*0.000*	*7.800*	*24*	
	43	*32.87*	*± 1.14*	*6.77*	*0.12*	*13.521*	*3.686*	*8.014*	*23*	
	45	*33.49*	*± 0.77*	*6.90*	*0.08*	*13.770*	*2.480*	*3.254*	*11*	
	46	*33.55*	*± 0.82*	*6.91*	*0.09*	*13.321*	*3.816*	*4.022*	*13*	
	48	*29.17*	*± 0.68*	*6.00*	*0.07*	*14.767*	*13.296*	*2.745*	*10*	
	49	*29.58*	*± 0.67*	*6.08*	*0.07*	*15.319*	*13.327*	*2.398*	*9*	
	51	*31.49*	*± 0.65*	*6.48*	*0.07*	*13.435*	*4.182*	*1.473*	*5*	
	52	*31.98*	*± 0.70*	*6.58*	*0.07*	*14.403*	*2.899*	*2.587*	*9*	
	54	*33.12*	*± 0.79*	*6.82*	*0.08*	*14.390*	*5.062*	*3.737*	*12*	
	55	*39.81*	*± 0.89*	*8.21*	*0.09*	*14.321*	*2.465*	*3.589*	*10*	
	57	*37.33*	*± 2.48*	*7.70*	*0.26*	*18.621*	*8.016*	*20.685*	*41*	
	58	*31.65*	*± 2.39*	*6.51*	*0.25*	*19.490*	*4.940*	*20.049*	*44*	
	60	*35.03*	*± 1.33*	*7.22*	*0.14*	*18.049*	*2.470*	*9.941*	*26*	
	61	*34.70*	*± 1.35*	*7.15*	*0.14*	*18.266*	*3.038*	*10.078*	*27*	
	63	*37.84*	*± 0.96*	*7.80*	*0.10*	*15.423*	*5.192*	*5.144*	*15*	
	64	*40.50*	*± 1.06*	*8.35*	*0.11*	*18.151*	*4.933*	*6.022*	*16*	
	66	*36.59*	*± 1.26*	*7.54*	*0.13*	*18.187*	*8.598*	*8.838*	*23*	
	67	*38.66*	*± 1.45*	*7.97*	*0.15*	*18.954*	*7.837*	*10.731*	*26*	
	69	*47.58*	*± 1.20*	*9.83*	*0.13*	*16.492*	*6.142*	*6.583*	*15*	
	70	*125.56*	*± 3.47*	*26.52*	*0.38*	*36.088*	*10.440*	*22.749*	*20*	
	72	*31.89*	*± 0.88*	*6.56*	*0.09*	*16.576*	*0.000*	*4.987*	*16*	
	73	*30.51*	*± 0.74*	*6.28*	*0.08*	*14.076*	*2.988*	*3.610*	*13*	
	74	*30.90*	*± 0.72*	*6.36*	*0.07*	*14.087*	*5.008*	*3.139*	*11*	***34***
A-4-68	245	*61.32*	*± 2.22*	*12.72*	*0.23*	*19.501*	*25.355*	*16.475*	*26*	
Plan du Lac	246	*40.61*	*± 2.03*	*8.38*	*0.21*	*21.339*	*32.150*	*16.278*	*34*	
Gneiss	247	*31.80*	*± 0.80*	*6.55*	*0.08*	*15.058*	*19.614*	*4.127*	*14*	
Lat.: 44.984950°	249	*28.77*	*± 1.17*	*5.92*	*0.12*	*16.462*	*21.462*	*8.823*	*27*	
Lon.: 6.143560°	250	*93.51*	*± 2.10*	*19.58*	*0.23*	*24.615*	*5.839*	*9.355*	*12*	
	251	*74.73*	*± 1.81*	*15.56*	*0.19*	*24.938*	*42.041*	*9.522*	*14*	
	253	*24.28*	*± 1.26*	*4.99*	*0.13*	*15.279*	*87.896*	*9.612*	*32*	
	254	*25.98*	*± 1.67*	*5.34*	*0.17*	*16.846*	*9.266*	*13.651*	*39*	
	255	*49.36*	*± 2.18*	*10.21*	*0.23*	*26.893*	*34.100*	*17.096*	*31*	
	257	*32.08*	*± 1.17*	*6.60*	*0.12*	*21.853*	*29.097*	*8.412*	*25*	
	258	*24.47*	*± 0.77*	*5.03*	*0.08*	*16.339*	*36.424*	*4.936*	*19*	
	259	*32.06*	*± 1.34*	*6.60*	*0.14*	*24.525*	*32.552*	*10.214*	*28*	
	264	*25.79*	*± 0.79*	*5.30*	*0.08*	*16.313*	*21.900*	*5.101*	*19*	
	265	*22.35*	*± 0.90*	*4.59*	*0.09*	*15.449*	*29.685*	*6.636*	*26*	
	266	*36.85*	*± 0.87*	*7.60*	*0.09*	*16.856*	*28.362*	*4.120*	*12*	***15***
A-4-68b (Ech8)	144	*24.88*	*± 0.54*	*5.14*	*0.06*	*12.752*	*3.706*	*0.478*	*2*	
Plan du Lac	145	*27.16*	*± 1.41*	*5.62*	*0.15*	*17.908*	*0.000*	*0.000*	*0*	
Gneiss	146	*26.65*	*± 0.55*	*5.51*	*0.06*	*13.920*	*0.000*	*0.507*	*2*	
Lat.: 44.984950°	148	*25.74*	*± 0.56*	*5.32*	*0.06*	*14.891*	*0.000*	*0.727*	*3*	
Lon.: 6.143560°	149	*25.16*	*± 0.55*	*5.20*	*0.06*	*14.784*	*0.000*	*0.583*	*3*	
	150	*25.95*	*± 0.55*	*5.37*	*0.06*	*14.536*	*12.917*	*0.570*	*3*	
	152	*26.58*	*± 0.69*	*5.50*	*0.07*	*12.124*	*5.811*	*0.701*	*3*	
	153	*25.66*	*± 2.89*	*5.30*	*0.30*	*12.211*	*0.000*	*0.066*	*0*	
	154	*25.75*	*± 3.15*	*5.32*	*0.33*	*12.126*	*271.884*	*0.184*	*0*	
	156	*32.57*	*± 3.85*	*6.75*	*0.40*	*10.353*	*108.067*	*1.046*	*4*	
	157	*47.23*	*± 1.41*	*9.82*	*0.15*	*11.567*	*168.834*	*3.893*	*9*	
	158	*46.40*	*± 1.90*	*9.65*	*0.20*	*17.515*	*18.150*	*14.508*	*29*	
	160	*201.82*	*± 12.76*	*43.83*	*1.46*	*46.660*	*2794.213*	*115.611*	*42*	
	161	*25.34*	*± 0.63*	*5.24*	*0.07*	*14.586*	*8.934*	*0.558*	*3*	
	162	*28.20*	*± 0.64*	*5.83*	*0.07*	*15.229*	*181.960*	*2.092*	*8*	
	164	*25.22*	*± 0.59*	*5.21*	*0.06*	*14.405*	*2.375*	*2.040*	*9*	
	165	*28.43*	*± 1.02*	*5.88*	*0.11*	*14.576*	*75.735*	*7.377*	*24*	
	166	*27.73*	*± 1.10*	*5.74*	*0.12*	*14.654*	*0.432*	*8.144*	*26*	
	168	*25.92*	*± 0.58*	*5.36*	*0.06*	*10.834*	*14.811*	*0.693*	*3*	
	169	*25.30*	*± 0.53*	*5.23*	*0.05*	*12.533*	*13.464*	*0.821*	*4*	
	170	*32.25*	*± 0.74*	*6.68*	*0.08*	*14.533*	*15.877*	*2.877*	*10*	
	172	*31.89*	*± 0.86*	*6.61*	*0.09*	*14.772*	*25.511*	*4.845*	*16*	
	173	*26.67*	*± 0.61*	*5.52*	*0.06*	*13.389*	*0.000*	*2.188*	*9*	
	174	*32.11*	*± 0.84*	*6.65*	*0.09*	*14.983*	*227.616*	*4.170*	*13*	
	176	*26.71*	*± 0.62*	*5.52*	*0.07*	*10.443*	*40.681*	*2.076*	*9*	
	177	*28.76*	*± 0.68*	*5.95*	*0.07*	*14.683*	*11.784*	*2.458*	*9*	
	178	*30.74*	*± 0.66*	*6.36*	*0.07*	*12.792*	*56.401*	*1.576*	*6*	
	180	*31.38*	*± 2.22*	*6.50*	*0.23*	*15.375*	*6.264*	*18.517*	*42*	
	181	*26.39*	*± 0.57*	*5.46*	*0.06*	*13.365*	*44.315*	*1.762*	*7*	
	182	*26.68*	*± 0.86*	*5.52*	*0.09*	*16.617*	*31.735*	*5.459*	*20*	

Sample	An.	*Age*	*(+2s)*	*40*/39(k)*	*1s*	*38Ar/39Ar*	*37Ar/39Ar*	*36Ar/39Ar*	*% Atm*	***n***
						*(*1000)*	*(*1000)*	*(*1000)*		
A-1-345	110	*389.51*	*± 27.17*	*89.23*	*3.46*	*109.716*	*5.672*	*280.279*	*48*	
Combeynot	111	*315.64*	*± 11.36*	*70.80*	*1.39*	*62.828*	*8.248*	*100.136*	*29*	
Porphyroid	113	*199.95*	*± 5.88*	*43.40*	*0.67*	*34.056*	*22.486*	*42.774*	*22*	
Lat.: 45.026510°	114	*330.96*	*± 7.53*	*74.56*	*0.93*	*42.462*	*3.763*	*44.245*	*15*	
Lon.: 6.404380°	116	*294.73*	*± 6.91*	*65.72*	*0.83*	*40.937*	*5.032*	*43.083*	*16*	
	117	*290.84*	*± 6.72*	*64.78*	*0.81*	*36.516*	*0.000*	*40.250*	*15*	
	119	*231.14*	*± 6.59*	*50.62*	*0.77*	*38.998*	*4.310*	*48.412*	*22*	
	120	*276.63*	*± 9.00*	*61.37*	*1.08*	*50.417*	*8.596*	*74.129*	*26*	
	122	*231.91*	*± 5.81*	*50.80*	*0.68*	*38.043*	*4.734*	*37.637*	*18*	
	123	*221.72*	*± 6.55*	*48.43*	*0.76*	*40.747*	*2.831*	*49.034*	*23*	
	125	*169.08*	*± 3.29*	*36.39*	*0.37*	*13.650*	*11.799*	*3.969*	*3*	
	126	*272.85*	*± 5.81*	*60.46*	*0.69*	*29.630*	*24.865*	*17.269*	*8*	
	128	*252.54*	*± 4.98*	*55.64*	*0.59*	*16.655*	*37.405*	*7.473*	*4*	
	129	*156.32*	*± 3.22*	*33.52*	*0.36*	*21.734*	*4.032*	*7.403*	*6*	
	130	*206.61*	*± 4.42*	*44.93*	*0.51*	*33.808*	*22.324*	*11.769*	*7*	***15***
A-1-355	205	*30.82*	*± 1.00*	*6.38*	*0.10*	*18.330*	*67.910*	*5.718*	*18*	
Col du Lac	206	*38.08*	*± 3.64*	*7.90*	*0.38*	*58.001*	*138.816*	*11.462*	*27*	
Gneiss	207	*32.87*	*± 0.88*	*6.81*	*0.09*	*15.744*	*85.272*	*2.104*	*7*	
Lat.: 45.017860°	209	*27.30*	*± 0.80*	*5.65*	*0.08*	*16.684*	*40.285*	*4.607*	*17*	
Lon.: 6.273540°	210	*27.06*	*± 0.99*	*5.60*	*0.10*	*16.173*	*83.580*	*5.847*	*20*	
	211	*24.80*	*± 0.76*	*5.13*	*0.08*	*15.227*	*32.113*	*3.441*	*14*	
	213	*24.80*	*± 0.57*	*5.13*	*0.06*	*13.758*	*26.275*	*2.476*	*11*	
	214	*26.58*	*± 1.41*	*5.50*	*0.15*	*30.685*	*83.420*	*4.539*	*17*	
	215	*26.02*	*± 0.65*	*5.38*	*0.07*	*16.349*	*154.835*	*2.906*	*11*	
	217	*32.34*	*± 1.05*	*6.70*	*0.11*	*16.960*	*124.361*	*7.162*	*21*	
	218	*27.13*	*± 0.91*	*5.61*	*0.09*	*17.432*	*244.419*	*5.225*	*18*	
	219	*27.77*	*± 1.05*	*5.74*	*0.11*	*19.465*	*251.880*	*6.967*	*23*	
	221	*26.22*	*± 0.66*	*5.42*	*0.07*	*15.212*	*51.173*	*2.493*	*10*	
	222	*88.86*	*± 8.58*	*18.70*	*0.93*	*22.432*	*121.326*	*71.317*	*52*	
	223	*58.72*	*± 2.12*	*12.25*	*0.22*	*22.361*	*24.720*	*14.784*	*25*	
	225	*27.22*	*± 0.88*	*5.63*	*0.09*	*15.473*	*93.917*	*5.594*	*20*	
	226	*31.72*	*± 1.11*	*6.57*	*0.12*	*19.244*	*109.244*	*6.726*	*20*	
	227	*26.44*	*± 2.01*	*5.47*	*0.21*	*18.452*	*89.430*	*16.213*	*42*	
	229	*41.30*	*± 1.63*	*8.58*	*0.17*	*15.750*	*79.334*	*11.810*	*27*	
	230	*30.61*	*± 1.13*	*6.34*	*0.12*	*19.183*	*111.046*	*5.922*	*19*	
	231	*23.88*	*± 1.64*	*4.93*	*0.17*	*16.507*	*58.995*	*13.359*	*40*	
	233	*27.55*	*± 1.44*	*5.70*	*0.15*	*10.904*	*120.782*	*9.622*	*29*	
	234	*26.44*	*± 4.85*	*5.47*	*0.50*	*16.482*	*272.598*	*41.140*	*64*	
	235	*21.09*	*± 4.19*	*4.36*	*0.44*	*23.129*	*37.242*	*36.304*	*67*	
	237	*14.54*	*± 9.58*	*3.00*	*0.99*	*31.718*	*0.581*	*83.039*	*86*	
	238	*33.41*	*± 2.36*	*6.92*	*0.25*	*22.418*	*113.398*	*18.933*	*41*	
	239	*42.68*	*± 2.22*	*8.87*	*0.23*	*15.109*	*82.208*	*16.743*	*33*	
	241	*36.11*	*± 2.27*	*7.49*	*0.24*	*19.655*	*164.103*	*18.251*	*38*	
	242	*109.75*	*± 7.11*	*23.23*	*0.78*	*27.052*	*135.090*	*49.364*	*38*	
	243	*37.65*	*± 2.33*	*7.81*	*0.24*	*24.920*	*87.031*	*18.521*	*38*	***30***
A-4-74b	268	*169.77*	*± 3.55*	*36.31*	*0.40*	*27.306*	*43.850*	*13.453*	*10*	
Plan du Lac	269	*52.47*	*± 1.07*	*10.86*	*0.11*	*16.745*	*55.616*	*2.240*	*5*	
Gneiss	270	*74.94*	*± 2.66*	*15.61*	*0.28*	*19.667*	*1412.051*	*14.647*	*19*	
Lat.: 44.984930°	272	*26.69*	*± 0.60*	*5.48*	*0.06*	*12.978*	*52.107*	*1.561*	*7*	
Lon.: 6.125820°	273	*24.76*	*± 0.68*	*5.09*	*0.07*	*13.439*	*3.485*	*3.354*	*14*	
	274	*24.29*	*± 1.75*	*4.99*	*0.18*	*16.268*	*13.714*	*14.242*	*41*	
	277	*105.95*	*± 2.91*	*22.26*	*0.32*	*31.313*	*74.487*	*7.328*	*9*	
	278	*186.61*	*± 4.40*	*40.10*	*0.50*	*26.968*	*0.000*	*22.227*	*14*	
	279	*158.63*	*± 4.59*	*33.82*	*0.51*	*28.448*	*79.390*	*30.843*	*21*	
	281	*207.10*	*± 5.24*	*44.76*	*0.60*	*34.788*	*41.001*	*32.855*	*18*	
	282	*132.95*	*± 4.52*	*28.14*	*0.50*	*31.099*	*26.803*	*32.926*	*25*	
	283	*76.73*	*± 3.65*	*15.99*	*0.39*	*12.256*	*154.469*	*25.925*	*31*	
	285	*126.70*	*± 3.73*	*26.77*	*0.41*	*22.875*	*33.883*	*24.493*	*21*	
	286	*43.97*	*± 5.66*	*9.08*	*0.59*	*22.167*	*48.539*	*48.845*	*59*	
	287	*57.14*	*± 1.27*	*11.84*	*0.13*	*16.889*	*58.258*	*4.372*	*9*	
	289	*105.53*	*± 2.37*	*22.17*	*0.26*	*21.393*	*37.534*	*6.227*	*7*	
	290	*131.78*	*± 3.12*	*27.89*	*0.34*	*26.144*	*18.864*	*14.691*	*13*	
	291	*111.61*	*± 6.66*	*23.49*	*0.72*	*37.316*	*48.608*	*54.146*	*40*	
	293	*40.96*	*± 0.98*	*8.45*	*0.10*	*18.950*	*68.986*	*1.636*	*5*	
	294	*36.84*	*± 0.82*	*7.59*	*0.09*	*16.349*	*5.038*	*2.719*	*9*	
	295	*54.01*	*± 1.35*	*11.18*	*0.14*	*20.151*	*2.290*	*6.796*	*14*	
	297	*32.65*	*± 0.93*	*6.72*	*0.10*	*16.406*	*321.626*	*4.222*	*13*	
	298	*36.43*	*± 0.87*	*7.51*	*0.09*	*14.979*	*25.149*	*1.999*	*6*	
	299	*32.17*	*± 0.80*	*6.62*	*0.08*	*15.178*	*20.601*	*3.209*	*11*	
	301	*40.05*	*± 0.91*	*8.26*	*0.09*	*13.792*	*14.734*	*2.443*	*7*	
	302	*32.71*	*± 0.81*	*6.73*	*0.08*	*13.812*	*102.166*	*1.986*	*7*	
	303	*38.28*	*± 1.00*	*7.89*	*0.10*	*15.011*	*2.251*	*5.515*	*16*	
	305	*46.66*	*± 1.09*	*9.64*	*0.11*	*17.635*	*42.403*	*4.734*	*12*	
	306	*47.53*	*± 1.15*	*9.83*	*0.12*	*17.989*	*25.982*	*5.711*	*13*	
	307	*59.65*	*± 1.67*	*12.37*	*0.18*	*19.478*	*125.491*	*9.956*	*18*	
	309	*25.22*	*± 1.08*	*5.18*	*0.11*	*15.696*	*103.169*	*8.232*	*28*	
	310	*43.87*	*± 1.14*	*9.06*	*0.12*	*16.736*	*4.395*	*6.180*	*15*	
	311	*86.77*	*± 3.01*	*18.13*	*0.32*	*26.519*	*11.467*	*22.305*	*26*	
	313	*45.26*	*± 1.45*	*9.35*	*0.15*	*20.073*	*12.845*	*9.898*	*22*	
	314	*34.80*	*± 1.04*	*7.17*	*0.11*	*16.355*	*471.527*	*6.146*	*17*	
	315	*73.72*	*± 3.24*	*15.35*	*0.34*	*28.247*	*13.271*	*25.751*	*32*	

	Sample	Lat.	Lon.	*Shear zone*	Lithology	n	T	σ	T	*σ*	XFe3+	σ	RSCM	σ
		(°)	(°)	*(or area)*		Cathelineau and Nieva [1985]			Vidal et al. [2005, 2006]				Beyssac et al. [2002]	
Cover	A-2-2	45.16481	5.851862	*Uriage*	Limestone	25	294	*17*	252	*61*	6	*5*	306	*13*
	A-1-321	45.223812	6.138562	*Bourg d'Oisans*	Shale	11	296	*9*	313	*55*	6	*6*	345	*9*
	A-1-345(2)	45.00973	6.26403	*Col du Lac*	Limestone	24	297	*12*	294	*45*	7	*5*	335	*5*
	A-4-232	44.55958	6.47881	*Embrun*	Black shale	13	288	*13*	269	*51*	5	*5*	308	*5*
Basement	A-4-114	45.08019	6.11031	*Col de Cluy*	Chloritoschist	4	259	*15*	187	*61*	34	*9*		
						7	275	*17*	255	*43*	30	*10*		
	A-4-64	44.97745	6.15251	*Plan du Lac*	Gneiss	8	267	*8*	255	*26*	29	*4*		
						3	256	*16*	267	*11*	34	*3*		
						4	261	*7*	250	*32*	31	*7*		
						5	262	*16*	250	*8*	32	*4*		
	A-4-28a	45.0173	6.270507	*Col du Lac*	Gneiss	7	268	*7*	258	*15*	32	*4*		
						10	266	*6*	262	*11*	30	*4*		
	A-4-222c	45.01764	6.28244		Gneiss	2	265	*4*	271	*10*	42	*3*		
						2	*262*	*2*	*263*	*9*	*46*	*0*		
						4	269	*1*	283	*4*	38	*1*		
						1	266		268	-	40	-		
	A-1-355	45.01786	6.27354		Gneiss	17	255	*8*	267	*13*	56	*5*		
						5	239	*18*	263	*9*	62	*3*		
	A-1-345	45.02651	6.40438	*Combeynot*	Orthogneiss	2	263	*1*	244	*1*	31	*0*		

Table 2

Sample	Lat.	Lon.	Elev.	Tectonic unit	Stratigraphic age	Lithology	n	R2/*RA1*	Tmax	sd
	(°)	(°)	(m)					ratio	(°C)	(°C)
A-1-001	45.004578	5.70136	560	Dauphinois	Upper Lias	Slate	14	0.70	329	8
A-1-004	*44.87225*	*5.86169*	*948*	*Dauphinois*	*Upper Lias*	*Slate*	*25*	*0.58*	*258*	*7*
A-1-007	45.069906	6.000484	806	Dauphinois	Lower Lias	Limestone	12	0.72	321	6
A-1-009	45.08103	6.04491	1513	Dauphinois	Lower Lias	Limestone	13	0.71	327	3
A-1-016	*45.03812*	*6.131952*	*1257*	*Dauphinois*	*Lower Dogger*	*Slate*	*12*	*0.63*	*321*	*12*
A-1-025	45.14811	6.31462	1516	Dauphinois	Upper Lias	Slate	12	0.69	335	6
A-1-029	45.032105	6.381495	1952	Dauphinois	Middle Dogger	Limestone	12	0.69	335	2
A-1-030	45.038448	6.398698	2128	Dauphinois	Lower Lias	Limestone	11	0.69	333	4
A-1-32	*45.042092*	*6.388473*	*2215*	*Dauphinois*	*Priabonian*	*Flysch*	*15*	*0.61*	*298*	*4*
A-1-37	45.291423	6.324367	1485	Dauphinois	Upper Lias	Slate	12	0.69	333	2
A-1-171	45.226435	6.190374	2119	Dauphinois	Lower Lias	Limestone	12	0.71	327	5
A-1-208	*45.062326*	*6.126121*	*1761*	*Dauphinois*	*Lower Lias*	*Limestone*	*11*	*0.63*	*319*	*8*
A-1-224	45.049632	6.102744	1166	Dauphinois	Lower Lias	Limestone	11	0.70	330	5
A-1-225	45.037	5.97841	1120	Dauphinois	Lower Lias	Limestone	10	0.70	331	3
A-1-318	44.984199	6.123207	982	Dauphinois	Upper Lias	Slate	14	0.69	333	9
A-1-320	45.127996	6.045468	801	Dauphinois	Upper Lias	Slate	12	0.69	336	9
A-1-321	45.223812	6.138562	1770	Dauphinois	Upper Lias	Slate	11	0.67	345	9
A-1-322b	45.21556	6.213118	1794	Dauphinois	Upper Lias	Slate	12	0.70	329	3
A-1-323	45.215115	6.252217	1461	Dauphinois	Upper Lias	Slate	12	0.69	336	8
A-1-324	45.192802	6.290928	1271	Dauphinois	Lower Lias	Limestone	12	0.69	332	3
A-1-326	*45.200339*	*6.336937*	*1502*	*Dauphinois*	*Lower Dogger*	*Slate*	*11*	*0.63*	*322*	*10*
A-1-327	45.218918	6.305905	1290	Dauphinois	Upper Lias	Slate	11	0.66	347	4
A-1-328	45.227265	6.303567	1240	Dauphinois	Lower Lias	Limestone	11	0.69	336	5
A-1-329	45.249661	6.28425	1286	Dauphinois	Lower Dogger	Slate	8	0.69	334	5
A-1-330	45.2608	6.367982	776	Dauphinois	Lower Dogger	Slate	12	0.66	347	6
A-1-331	45.291702	6.23121	1107	Dauphinois	Upper Lias	Slate	12	0.69	332	12
A-1-332	45.045302	6.313245	1464	Dauphinois	Upper Lias	Slate	12	0.69	332	8
A-1-333	45.040348	6.30609	1592	Dauphinois	Lower Dogger	Slate	12	0.71	326	4
A-1-334	45.039006	6.304639	1587	Dauphinois	Lower Dogger	Slate	11	0.70	328	4
A-1-337	45.052165	6.288855	1806	Dauphinois	Lower Dogger	Slate	13	0.70	330	4
A-1-342	*45.076795*	*6.338908*	*2119*	*Dauphinois*	*Middle Dogger*	*Limestone*	*11*	*0.64*	*326*	*4*
A-1-345(2)	45.00973	6.26403	3193	Dauphinois	Upper Lias	Slate	12	0.69	335	5
A-2-002	*45.16481*	*5.851862*	*813*	*Dauphinois*	*Lower Dogger*	*Slate*	*12*	*0.62*	*306*	*13*
A-2-003	*45.162054*	*5.81894*	*393*	*Dauphinois*	*Middle Dogger*	*Limestone*	*10*	*0.62*	*306*	*6*
A-3-019	*44.526656*	*6.726225*	*1690*	*Embrunais-Ubaye*	*Cretaceous*	*Helm. Flysch*	*12*	*0.59*	*262*	*6*
A-4-005	*45.052408*	*6.390277*	*2355*	*Dauphinois*	*Priabonian*	*Flysch*	*12*	*0.61*	*296*	*9*
A-4-006	*45.05279*	*6.40051*	*2379*	*Dauphinois*	*Priabonian*	*Flysch*	*12*	*0.61*	*288*	*6*
A-4-010	*45.06035*	*6.4223*	*2758*	*Tête Noire*	*Cretaceous*	*Helm. Flysch*	*12*	*0.59*	*265*	*8*
A-4-011	*45.06062*	*6.42282*	*2772*	*Tête Noire*	*Cretaceous*	*Helm. Flysch*	*11*	*0.58*	*261*	*9*
A-4-014	*45.063536*	*6.412644*	*2670*	*Subbriançonnais*	*Eocene*	*Flysch*	*12*	*0.59*	*267*	*6*
A-4-039c1	*45.04773*	*6.13796*	*1072*	*Grandes Rousses*	*Carboniferous*	*Sandstone*	*15*	*0.63*	*319*	*7*
A-4-042	45.044332	6.15657	1064	Dauphinois	Lower Dogger	Slate	15	0.69	335	14
A-4-044	45.042854	6.168657	1462	Dauphinois	Lower Dogger	Slate	12	0.70	329	5
A-4-055	45.0421	6.35506	1770	Dauphinois	Lower Dogger	Slate	12	0.69	335	3
A-4-057	45.016852	6.039292	1509	Dauphinois	Lower Lias	Limestone	12	0.69	334	2
A-4-121	*44.95072*	*5.96606*	*978*	*Dauphinois*	*Lower Lias*	*Limestone*	*10*	*0.64*	*326*	*7*
A-4-122	*44.89179*	*5.8778*	*695*	*Dauphinois*	*Lower Lias*	*Limestone*	*12*	*0.61*	*298*	*10*
A-4-123	*44.87871*	*5.7535*	*793*	*Dauphinois*	*Lower Dogger*	*Slate*	*12*	*0.60*	*279*	*9*
A-4-124	*44.87459*	*5.71011*	*667*	*Dauphinois*	*Lower Lias*	*Limestone*	*14*	*0.64*	*334*	*6*
A-4-126	*44.96182*	*5.81198*	*1181*	*Dauphinois*	*Upper Lias*	*Slate*	*11*	*0.63*	*314*	*8*
A-4-140	45.33314	6.33442	1137	Dauphinois	Upper Lias	Slate	11	0.70	331	3
A-4-196	*44.789297*	*6.45698*	*1671*	*Dauphinois*	*Priabonian*	*Flysch*	*11*	*0.64*	*330*	*5*
A-4-197	45.03796	5.7054	403	Dauphinois	Upper Lias	Slate	12	0.69	334	4
A-4-198	*45.04444*	*5.69423*	*309*	*Dauphinois*	*Middle Dogger*	*Limestone*	*11*	*0.64*	*325*	*6*
A-4-199	*45.04834*	*5.68057*	*340*	*Dauphinois*	*Middle Dogger*	*Limestone*	*12*	*0.61*	*296*	*5*
A-4-200	*45.01018*	*5.63507*	*499*	*Subalpine chain*	*Lower Malm*	*Marls*	*12*	*0.54*	*208*	*9*
A-4-201	*45.00197*	*5.62223*	*741*	*Subalpine chain*	*Lower Malm*	*Marls*	*14*		*< 200*	
A-4-223	45.013605	6.283496	2509	Dauphinois	Lower Lias	Limestone	11	0.68	338	4
A-4-231	*44.63593*	*6.56532*	*912*	*Subbriançonnais*	*Eocene*	*Flysch*	*16*	*0.62*	*302*	*10*
A-4-232	*44.55958*	*6.47881*	*883*	*Vocontian domain*	*Dogger/Malm*	*Black Shale*	*13*	*0.62*	*308*	*5*
A-4-233	*44.58166*	*6.39937*	*1211*	*Vocontian domain*	*Dogger/Malm*	*Black Shale*	*11*	*0.59*	*271*	*11*
A-4-235	*44.5549*	*6.34229*	*1246*	*Vocontian domain*	*Dogger/Malm*	*Black Shale*	*11*	*0.58*	*253*	*10*
A-4-236	*44.714333*	*6.156877*	*1667*	*Dauphinois*	*Upper Lias*	*Slate*	*11*	*0.56*	*228*	*8*
A-4-238	*44.713257*	*6.167974*	*1960*	*Dauphinois*	*Upper Lias*	*Slate*	*12*	*0.54*	*202*	*4*
A-4-239b	*44.714389*	*6.168411*	*1982*	*Dauphinois*	*Priabonian*	*Flysch*	*13*		*< 200*	
A-4-242	*45.027604*	*6.312056*	*2228*	*Dauphinois*	*Lower Lias*	*Limestone*	*10*	*0.64*	*333*	*8*
A-4-244	*44.83378*	*5.93966*	*1002*	*Dauphinois*	*Upper Lias*	*Slate*	*11*	*0.57*	*237*	*7*
A-4-247	44.844446	6.127314	2055	Dauphinois	Lower Lias	Limestone	12	0.69	334	2
A-5-1	*44.867686*	*5.61239*	*847*	*Subalpine chain*	*Lower Malm*	*Marls*	*13*	*0.54*	*204*	*14*
A-5-2	*44.92326*	*5.63483*	*829*	*Dauphinois*	*Middle Dogger*	*Limestone*	*11*	*0.61*	*288*	*7*
A-5-3	*44.95121*	*5.60154*	*788*	*Subalpine chain*	*Upper Dogger*	*Marls*	*11*		*< 200*	
A-5-4	*44.9613*	*5.58629*	*701*	*Subalpine chain*	*Lower Malm*	*Marls*	*12*		*< 200*	
A-5-5	*44.92913*	*5.63472*	*819*	*Dauphinois*	*Middle Dogger*	*Limestone*	*11*	*0.60*	*286*	*5*
A-5-6	*44.9058*	*5.6258*	*902*	*Subalpine chain*	*Upper Dogger*	*Marls*	*15*	*0.56*	*227*	*23*
A-4-154	45.25002	6.78357	1438	Subbriançonnais	Lias	Limestone	12	0.51	412	5
A-4-228	*44.814212*	*6.567413*	*1147*	*Dent Parraché*	*Malm*	*Limestone*	*12*	*0.61*	*291*	*6*

Table 1

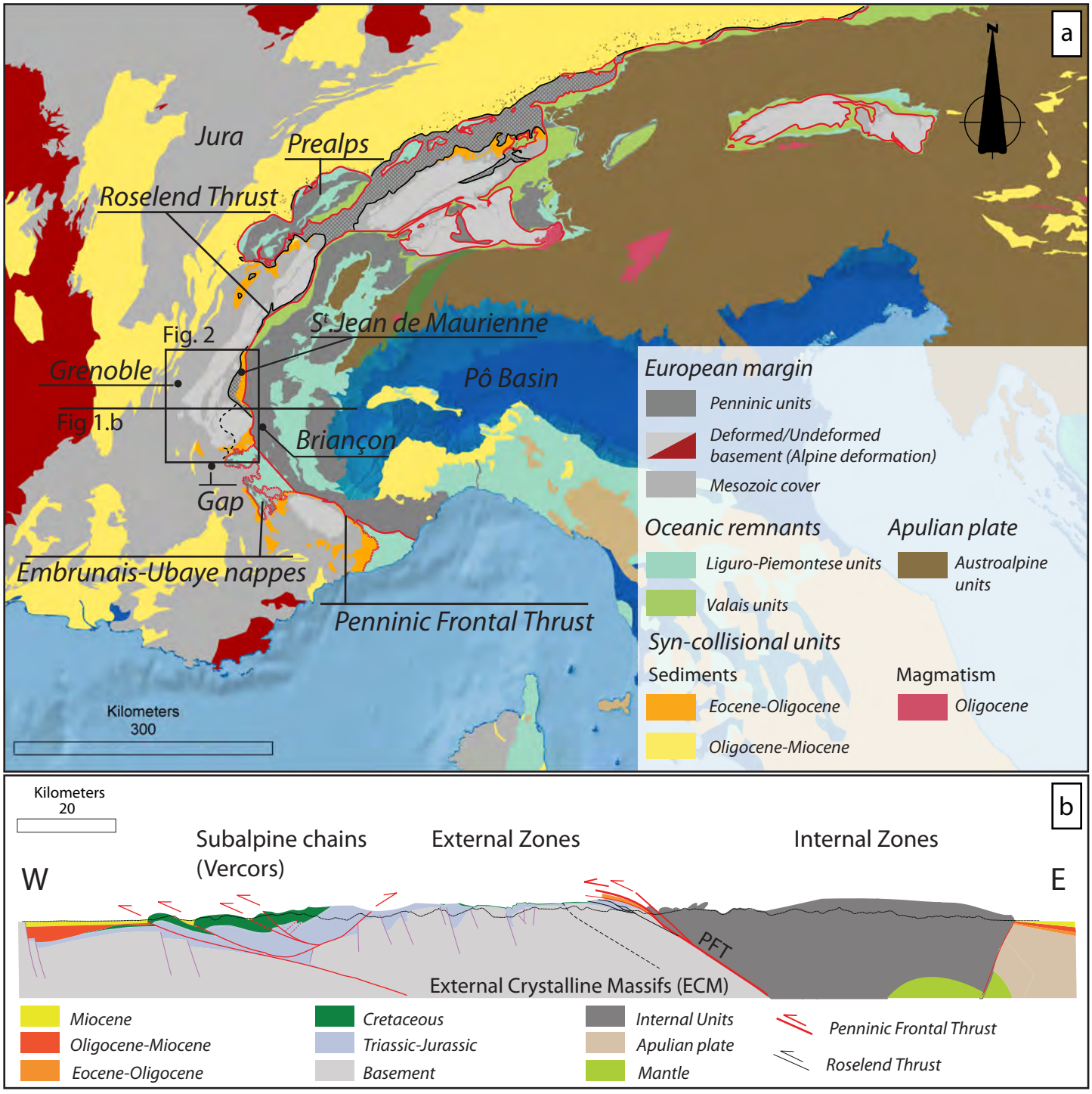
a
Jura
Prealps
Roselend Thrust
Fig. 2
St.Jean de Maurienne
Grenoble
Pô Basin
Fig 1.b
Briançon
Gap
Embrunais-Ubaye nappes
Penninic Frontal Thrust
Kilometers
300
European margin
Penninic units
Deformed/Undeformed basement (Alpine deformation)
Mesozoic cover
Oceanic remnants
Liguro-Piemontese units
Valais units
Apulian plate
Austroalpine units
Syn-collisional units
Sediments
Eocene-Oligocene
Oligocene-Miocene
Magmatism
Oligocene
b
Kilometers
20
Subalpine chains (Vercors)
External Zones
Internal Zones
W
E
PFT
External Crystalline Massifs (ECM)
Miocene
Oligocene-Miocene
Eocene-Oligocene
Cretaceous
Triassic-Jurassic
Basement
Internal Units
Apulian plate
Mantle
Penninic Frontal Thrust
Roselend Thrust

Figure 1

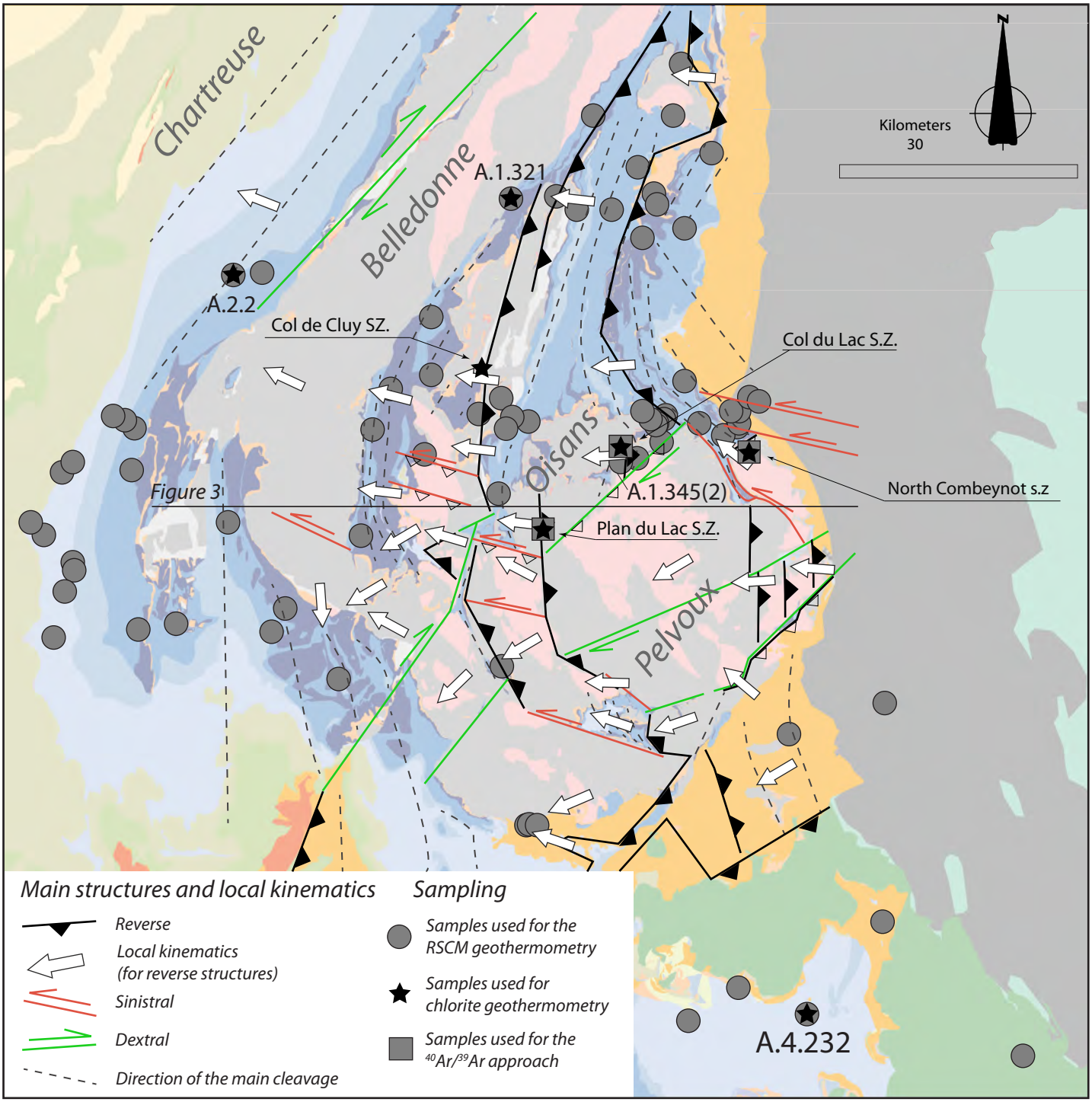
Chartreuse
Belledonne
Oisans
Pelvoux
A.1.321
A.2.2
A.1.345(2)
A.4.232
Col de Cluy SZ.
Col du Lac S.Z.
North Combeynot s.z
Plan du Lac S.Z.
Figure 3
Kilometers
30
N
Main structures and local kinematics
Reverse
Local kinematics
(for reverse structures)
Sinistral
Dextral
Direction of the main cleavage
Sampling
Samples used for the
RSCM geothermometry
Samples used for
chlorite geothermometry
Samples used for the
40Ar/39Ar approach

Figure 2

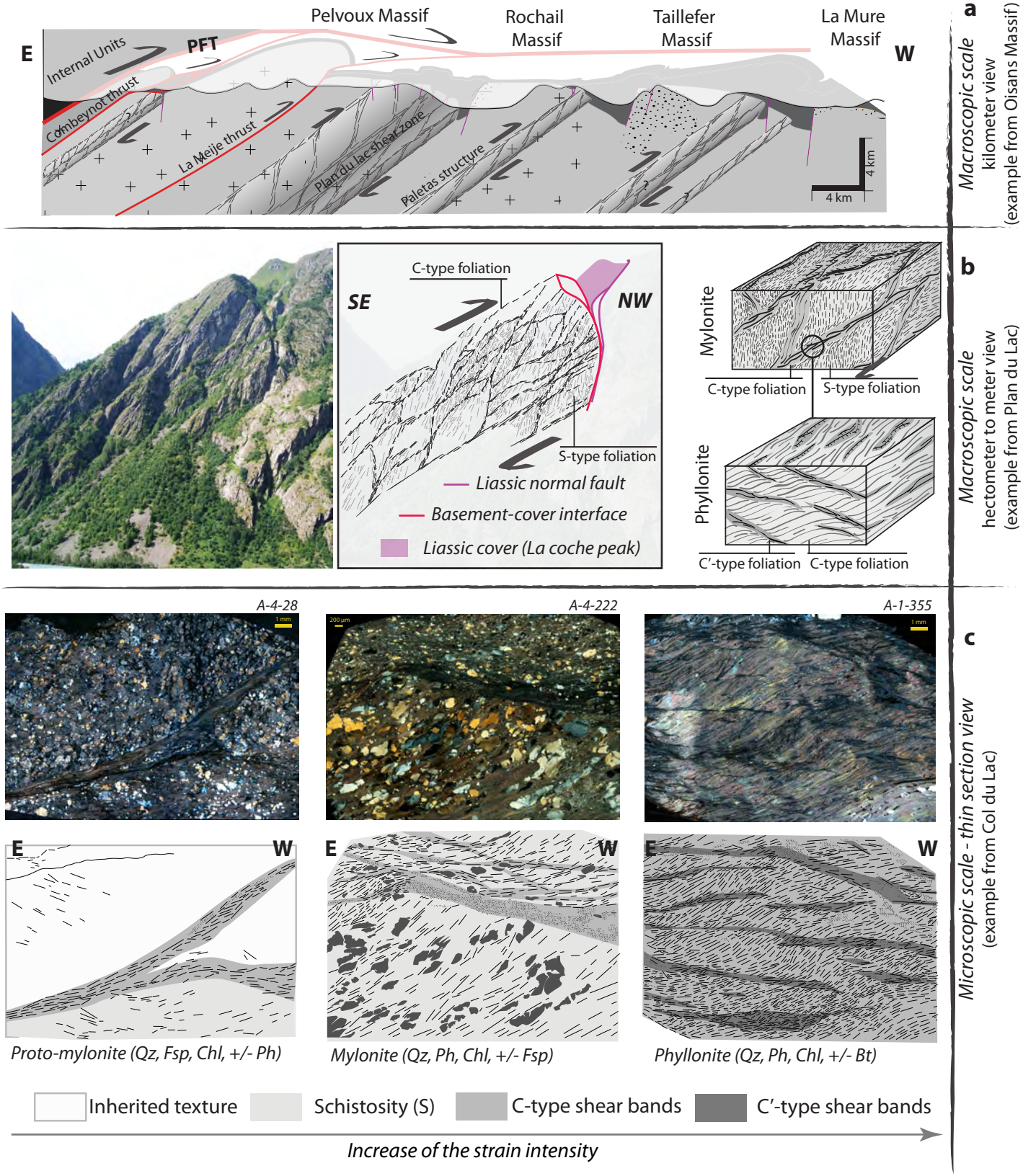
a
Macroscopic scale
kilometer view
(example from Oisans Massif)
E
W
Internal Units
PFT
Combeynot thrust
La Meije thrust
Pelvoux Massif
Rochail Massif
Taillefer Massif
La Mure Massif
Plan du lac shear zone
Paletas structure
4 km
4 km
b
Macroscopic scale
hectometer to meter view
(example from Plan du Lac)
C-type foliation
SE
NW
S-type foliation
Liassic normal fault
Basement-cover interface
Liassic cover (La coche peak)
Mylonite
C-type foliation
S-type foliation
Phyllonite
C'-type foliation
C-type foliation
c
Microscopic scale - thin section view
(example from Col du Lac)
A-4-28
A-4-222
A-1-355
E
W
Proto-mylonite (Qz, Fsp, Chl, +/- Ph)
Mylonite (Qz, Ph, Chl, +/- Fsp)
Phyllonite (Qz, Ph, Chl, +/- Bt)
Inherited texture
Schistosity (S)
C-type shear bands
C'-type shear bands
Increase of the strain intensity

Figure 3

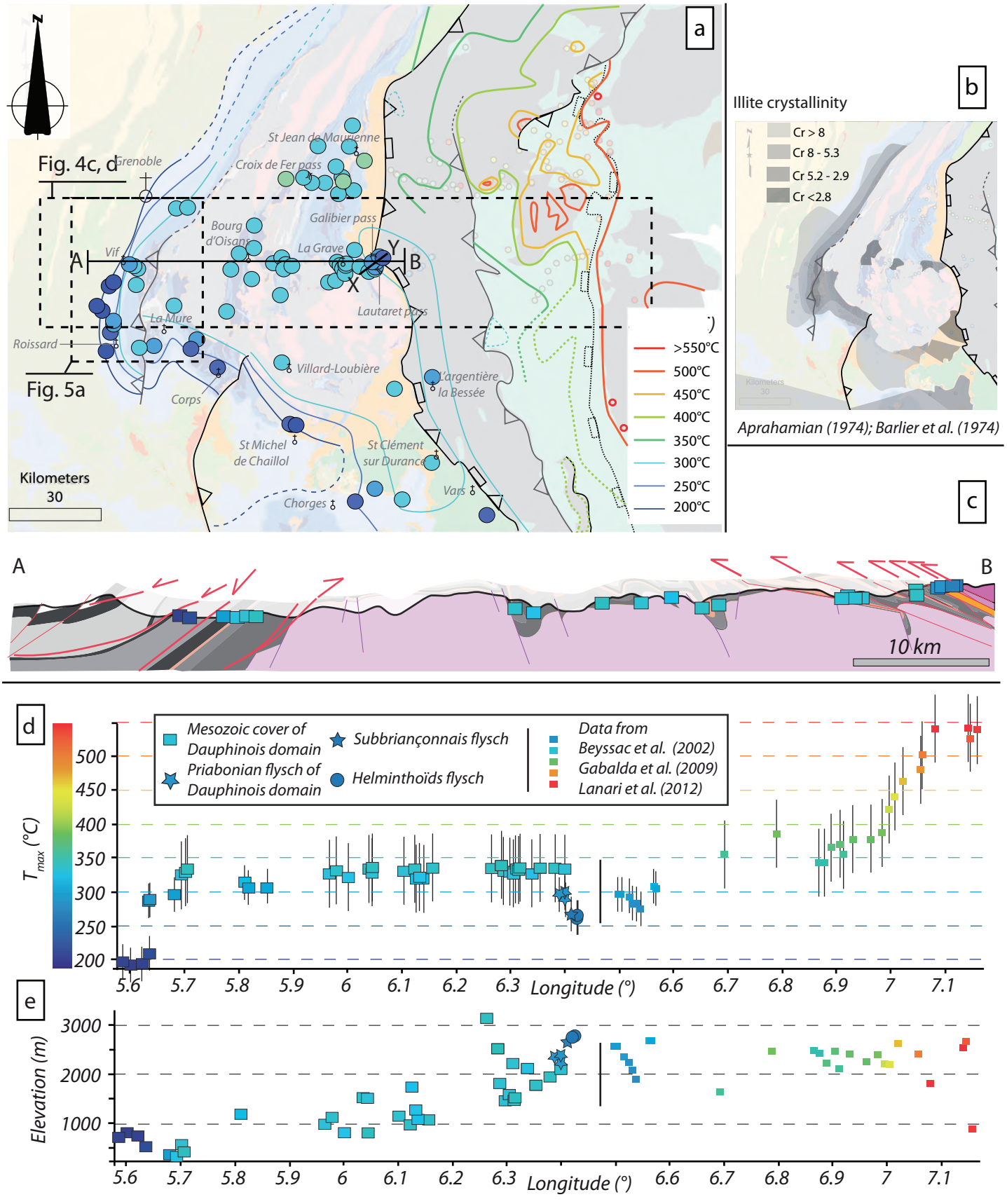
a
N
Fig. 4c, d
Grenoble
St Jean de Maurienne
Croix de Fer pass
Galibier pass
Bourg d'Oisans
Vif
La Grave
A
B
X
Y
Lautaret pass
La Mure
Roissard
Fig. 5a
Villard-Loubière
Corps
l'argentière la Bessée
St Michel de Chaillol
St Clément sur Durance
Vars
Chorges
Kilometers
30
>550°C
500°C
450°C
400°C
350°C
300°C
250°C
200°C
b
Illite crystallinity
Cr > 8
Cr 8 - 5.3
Cr 5.2 - 2.9
Cr <2.8
Aprahamian (1974); Barlier et al. (1974)
c
A
B
10 km
d
Mesozoic cover of Dauphinois domain
Priabonian flysch of Dauphinois domain
Subbriançonnais flysch
Helminthoïds flysch
Data from
Beyssac et al. (2002)
Gabalda et al. (2009)
Lanari et al. (2012)
T_{max} (°C)
500
450
400
350
300
250
200
5.6
5.7
5.8
5.9
6
6.1
6.2
6.3
Longitude (°)
6.6
6.7
6.8
6.9
7
7.1
e
Elevation (m)
3000
2000
1000
5.6
5.7
5.8
5.9
6
6.1
6.2
6.3
Longitude (°)
6.6
6.7
6.8
6.9
7
7.1

Figure 4

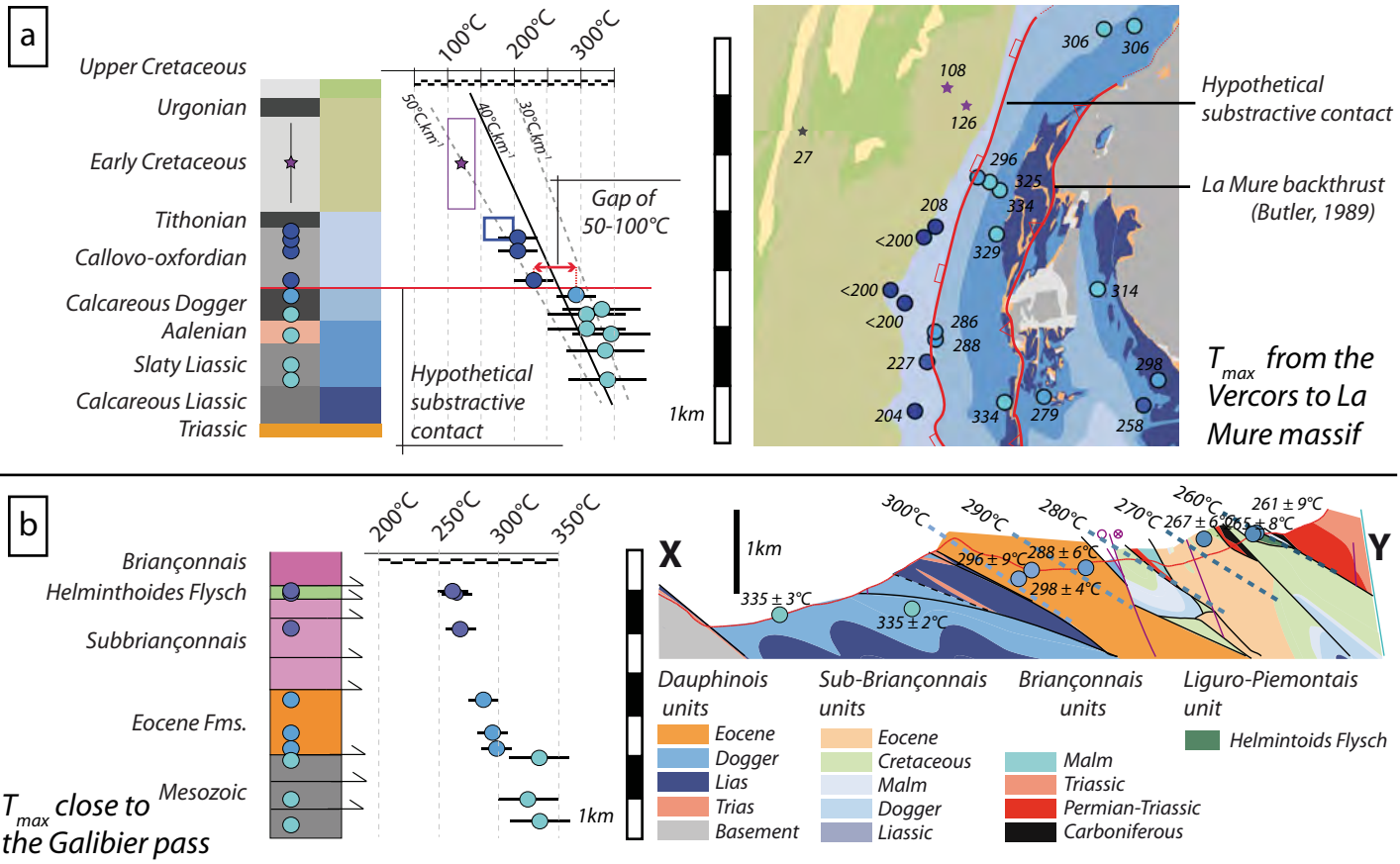
a
Upper Cretaceous
Urgonian
Early Cretaceous
Tithonian
Callovo-oxfordian
Calcareous Dogger
Aalenian
Slaty Liassic
Calcareous Liassic
Triassic
100°C
200°C
300°C
50°C.km-1
40°C.km-1
30°C.km-1
Gap of 50-100°C
Hypothetical substractive contact
1km
306
306
108
126
27
296
325
334
208
<200
329
<200
314
<200
286
288
227
298
204
334
279
258
Hypothetical substractive contact
La Mure backthrust (Butler, 1989)
T max from the Vercors to La Mure massif
b
Briançonnais
Helminthoides Flysch
Subbriançonnais
Eocene Fms.
Mesozoic
T max close to the Galibier pass
200°C
250°C
300°C
350°C
1km
X
Y
1km
300°C
290°C
280°C
270°C
260°C
335 ± 3°C
335 ± 2°C
296 ± 9°C
288 ± 6°C
298 ± 4°C
267 ± 6°C
261 ± 9°C
265 ± 8°C
Dauphinois units
Eocene
Dogger
Lias
Trias
Basement
Sub-Briançonnais units
Eocene
Cretaceous
Malm
Dogger
Liassic
Briançonnais units
Malm
Triassic
Permian-Triassic
Carboniferous
Liguro-Piemontais unit
Helmintoids Flysch

Figure 5

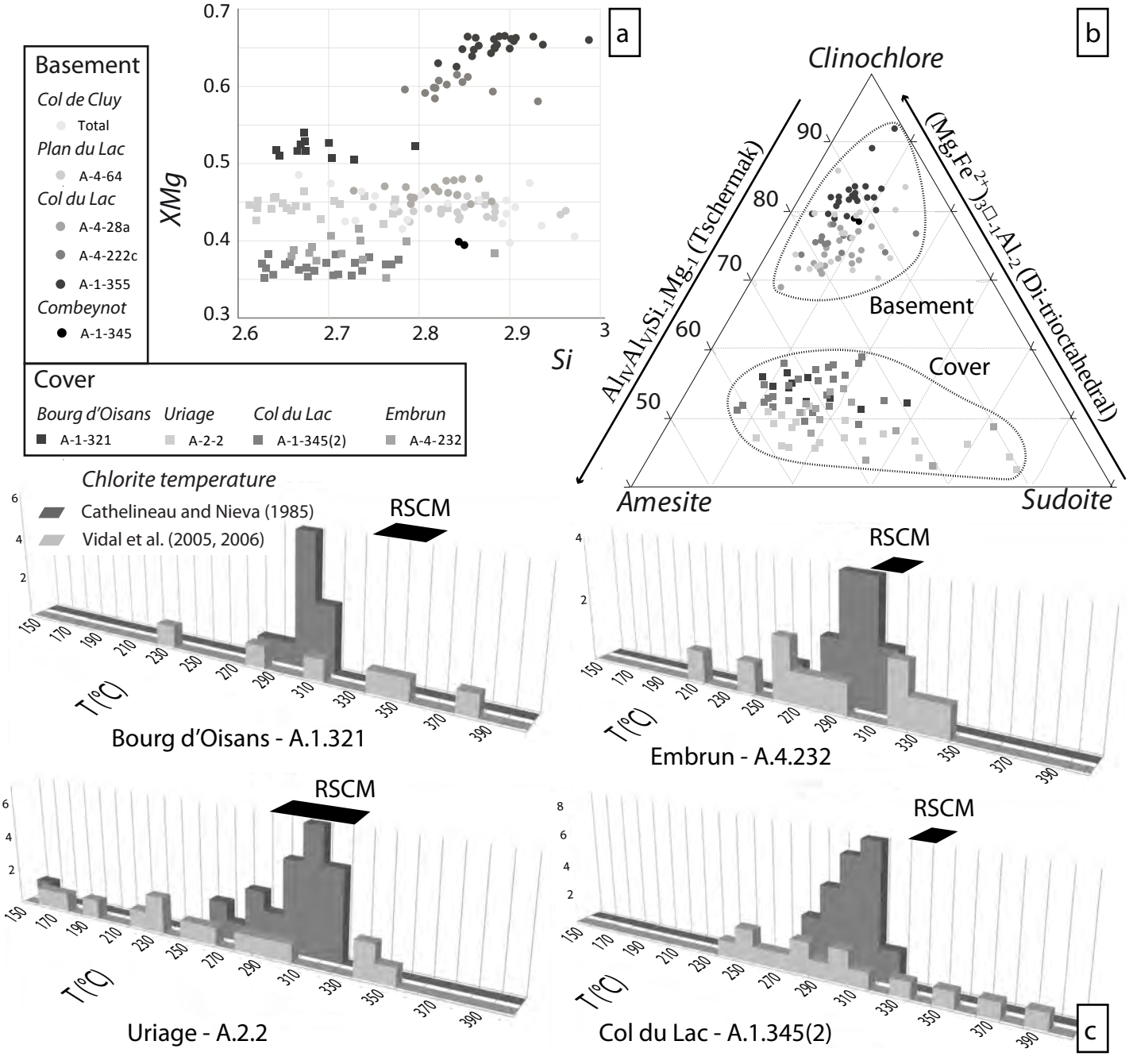
a
b
c
Basement
Col de Cluy
Total
Plan du Lac
A-4-64
Col du Lac
A-4-28a
A-4-222c
A-1-355
Combeynot
A-1-345
Cover
Bourg d'Oisans
A-1-321
Uriage
A-2-2
Col du Lac
A-1-345(2)
Embrun
A-4-232
XMg
Si
Clinochlore
Amesite
Sudoite
Basement
Cover
(Mg,Fe2+)3□-1Al2 (Di-trioctahedral)
Chlorite temperature
Cathelineau and Nieva (1985)
Vidal et al. (2005, 2006)
RSCM
T(°C)
Bourg d'Oisans - A.1.321
Embrun - A.4.232
Uriage - A.2.2
Col du Lac - A.1.345(2)

Figure 6

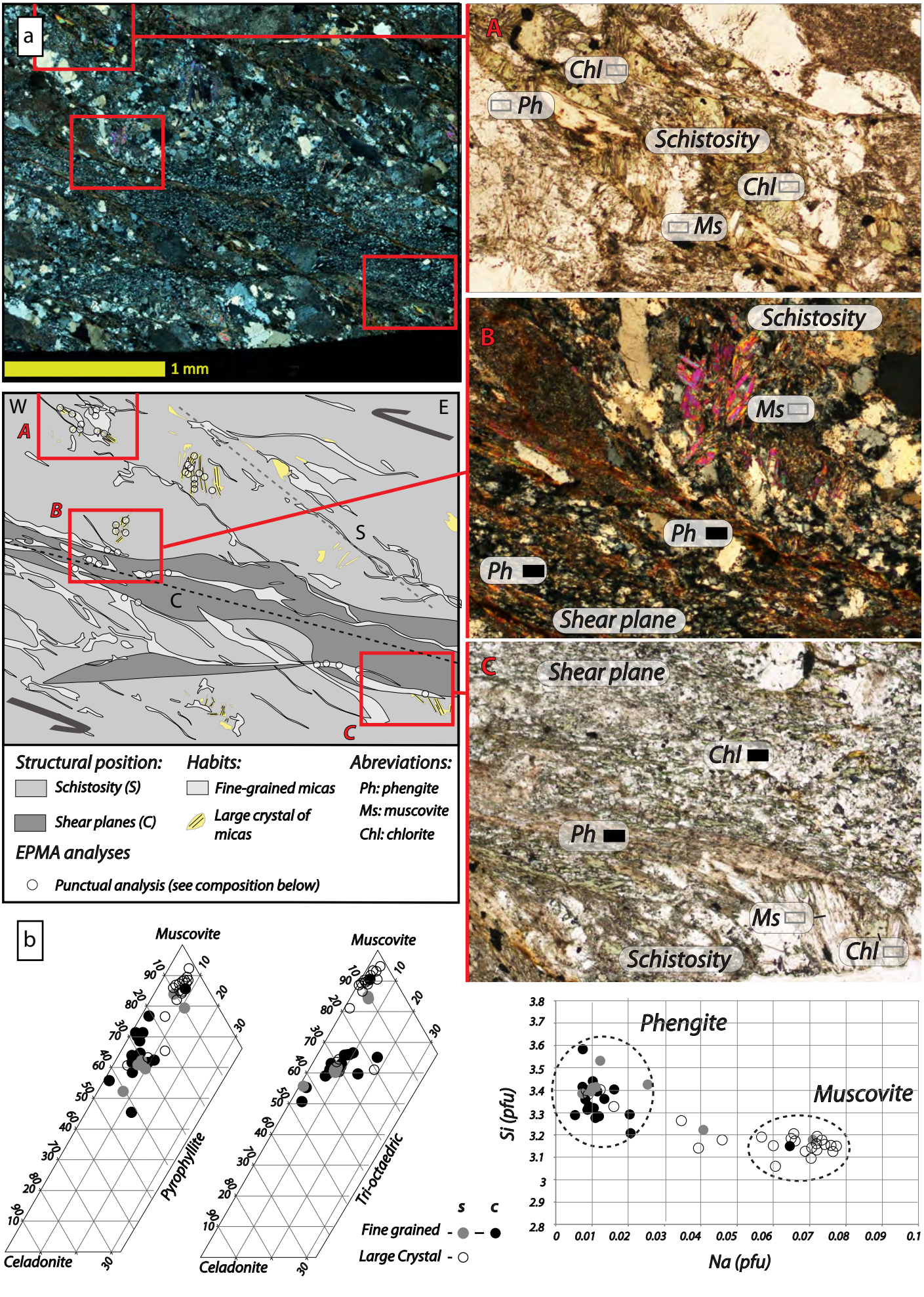
a
1 mm
A
Chl
Ph
Schistosity
Chl
Ms
B
Schistosity
Ms
Ph
Ph
Shear plane
C
Shear plane
Chl
Ph
Ms
Schistosity
Chl
W
E
A
B
C
S
C
Structural position:
Schistosity (S)
Shear planes (C)
Habits:
Fine-grained micas
Large crystal of micas
Abreviations:
Ph: phengite
Ms: muscovite
Chl: chlorite
EPMA analyses
Punctual analysis (see composition below)
b
Muscovite
Pyrophyllite
Celadonite
Muscovite
Tri-octaedric
Celadonite
S
C
Fine grained
Large Crystal
Phengite
Muscovite
Si (pfu)
Na (pfu)
3.8
3.7
3.6
3.5
3.4
3.3
3.2
3.1
3
2.9
2.8
0
0.01
0.02
0.03
0.04
0.05
0.06
0.07
0.08
0.09
0.1

Figure 7

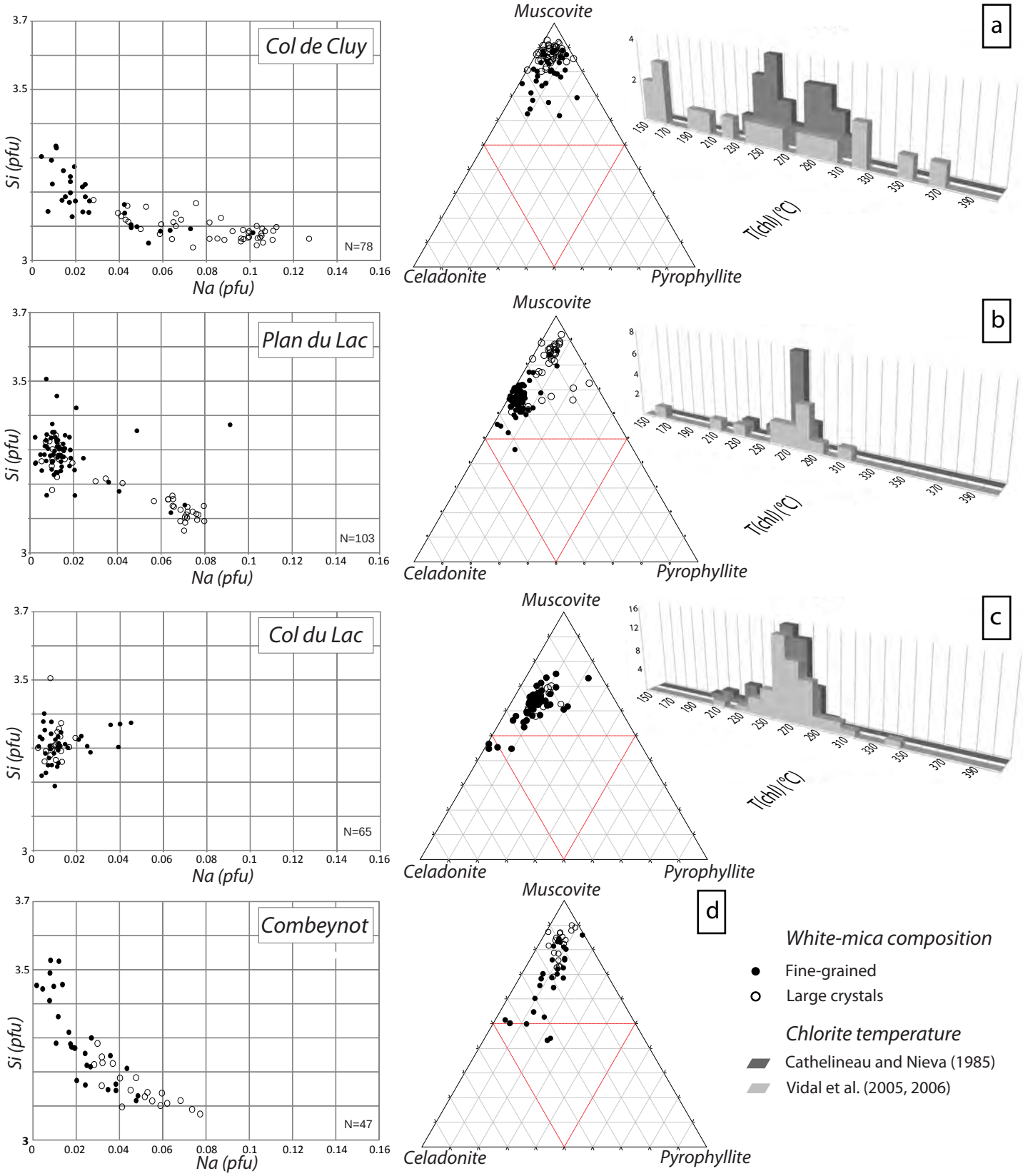
Col de Cluy
N=78
Plan du Lac
N=103
Col du Lac
N=65
Combeynot
N=47
Si (pfu)
Na (pfu)
Muscovite
Celadonite
Pyrophyllite
T(chl) (°C)
a
b
c
d
White-mica composition
Fine-grained
Large crystals
Chlorite temperature
Cathelineau and Nieva (1985)
Vidal et al. (2005, 2006)

Figure 8

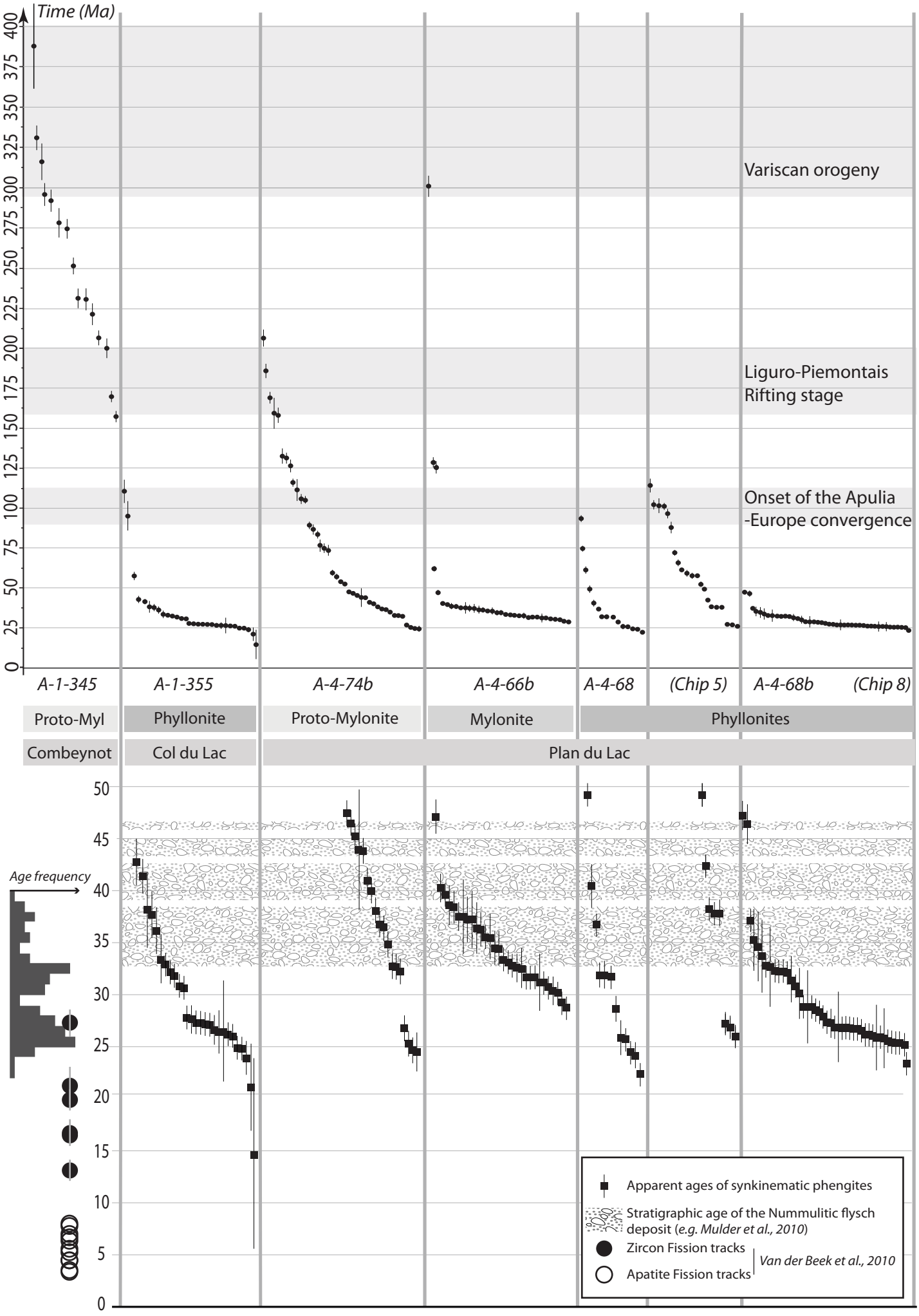
Time (Ma)
0
25
50
75
100
125
150
175
200
225
250
275
300
325
350
375
400
Variscan orogeny
Liguro-Piemontais
Rifting stage
Onset of the Apulia
-Europe convergence
A-1-345
A-1-355
A-4-74b
A-4-66b
A-4-68
(Chip 5)
A-4-68b
(Chip 8)
Proto-Myl
Phyllonite
Proto-Mylonite
Mylonite
Phyllonites
Combeynot
Col du Lac
Plan du Lac
Age frequency
0
5
10
15
20
25
30
35
40
45
50
Apparent ages of synkinematic phengites
Stratigraphic age of the Nummulitic flysch deposit (e.g. Mulder et al., 2010)
Zircon Fission tracks
Apatite Fission tracks
Van der Beek et al., 2010

Figure 9

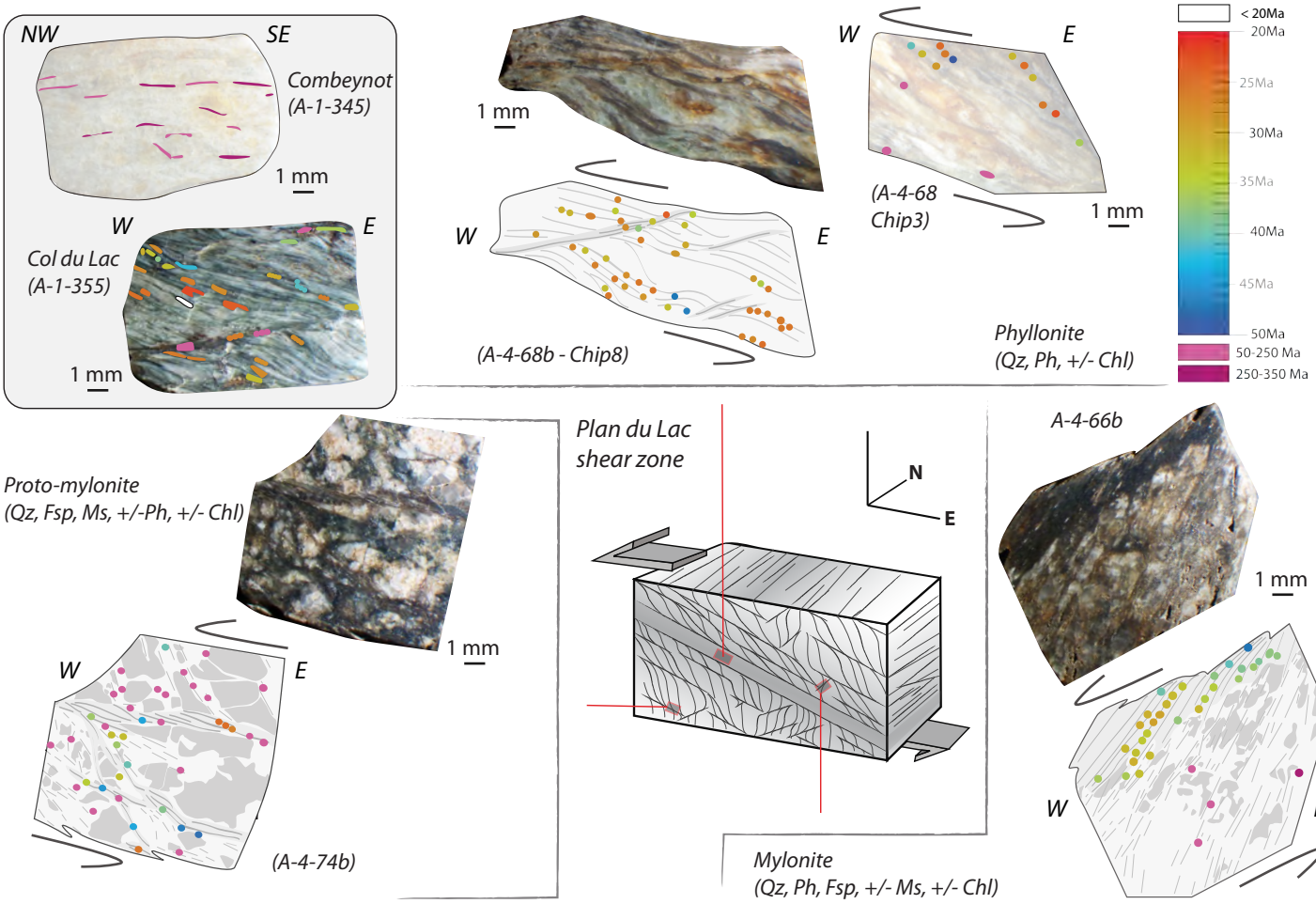
NW
SE
Combeynot
(A-1-345)
1 mm
W
E
Col du Lac
(A-1-355)
1 mm
1 mm
W
E
(A-4-68b - Chip8)
W
E
(A-4-68
Chip3)
1 mm
Phyllonite
(Qz, Ph, +/- Chl)
< 20Ma
20Ma
25Ma
30Ma
35Ma
40Ma
45Ma
50Ma
50-250 Ma
250-350 Ma
Proto-mylonite
(Qz, Fsp, Ms, +/-Ph, +/- Chl)
1 mm
W
E
(A-4-74b)
Plan du Lac
shear zone
N
E
Mylonite
(Qz, Ph, Fsp, +/- Ms, +/- Chl)
A-4-66b
1 mm
W
E

Figure 10

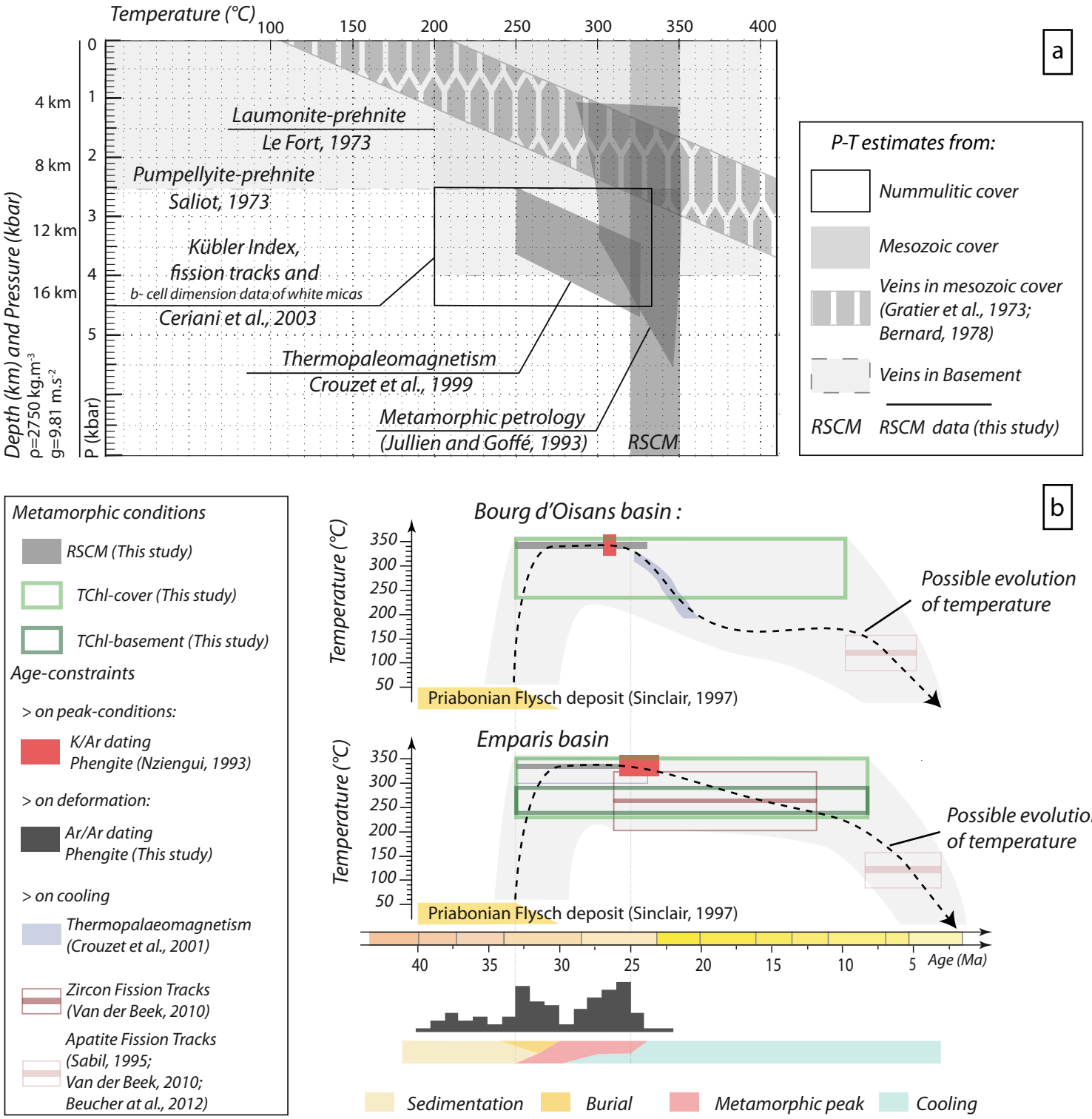
Temperature (°C)
100
150
200
250
300
350
400
a
0
1
2
3
4
5
4 km
8 km
12 km
16 km
P (kbar)
Depth (km) and Pressure (kbar)
ρ=2750 kg.m-3
g=9.81 m.s-2
Laumonite-prehnite
Le Fort, 1973
Pumpellyite-prehnite
Saliot, 1973
Kübler Index,
fission tracks and
b- cell dimension data of white micas
Ceriani et al., 2003
Thermopaleomagnetism
Crouzet et al., 1999
Metamorphic petrology
(Jullien and Goffé, 1993)
RSCM
P-T estimates from:
Nummulitic cover
Mesozoic cover
Veins in mesozoic cover
(Gratier et al., 1973;
Bernard, 1978)
Veins in Basement
RSCM
RSCM data (this study)
b
Metamorphic conditions
RSCM (This study)
TChl-cover (This study)
TChl-basement (This study)
Age-constraints
> on peak-conditions:
K/Ar dating
Phengite (Nziengui, 1993)
> on deformation:
Ar/Ar dating
Phengite (This study)
> on cooling
Thermopalaeomagnetism
(Crouzet et al., 2001)
Zircon Fission Tracks
(Van der Beek, 2010)
Apatite Fission Tracks
(Sabil, 1995;
Van der Beek, 2010;
Beucher at al., 2012)
Bourg d'Oisans basin :
Temperature (°C)
350
300
250
200
150
100
50
Possible evolution
of temperature
Priabonian Flysch deposit (Sinclair, 1997)
Emparis basin
Temperature (°C)
350
300
250
200
150
100
50
Possible evolution
of temperature
Priabonian Flysch deposit (Sinclair, 1997)
40
35
30
25
20
15
10
5
Age (Ma)
Sedimentation
Burial
Metamorphic peak
Cooling

Figure 11

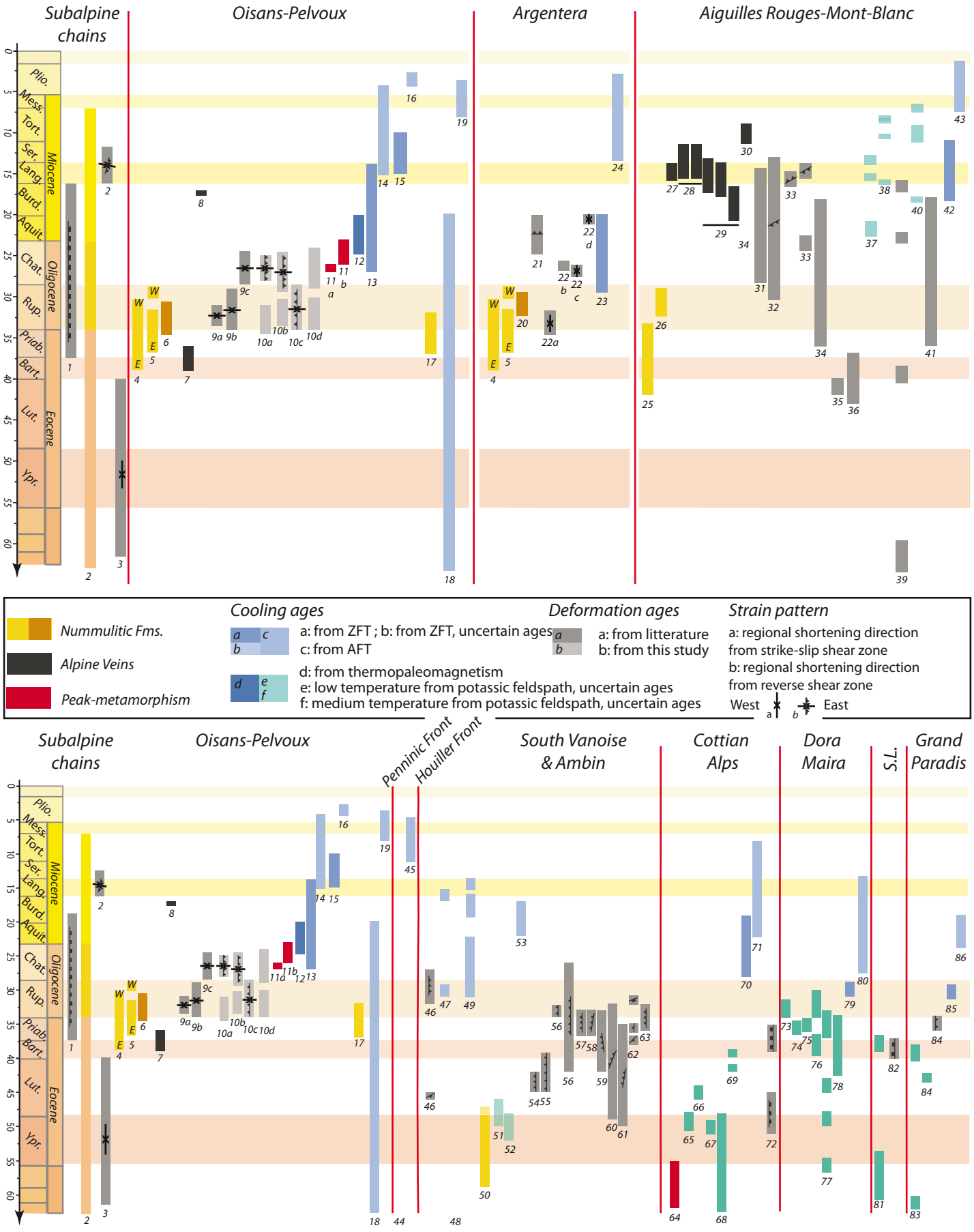
Subalpine chains
Oisans-Pelvoux
Argentera
Aiguilles Rouges-Mont-Blanc
Plio.
Mess.
Tort.
Ser.
Lang.
Burd.
Aquit.
Chat.
Rup.
Priab.
Bart.
Lut.
Ypr.
Miocene
Oligocene
Eocene
Nummulitic Fms.
Alpine Veins
Peak-metamorphism
Cooling ages
a: from ZFT ; b: from ZFT, uncertain ages
c: from AFT
d: from thermopaleomagnetism
e: low temperature from potassic feldspath, uncertain ages
f: medium temperature from potassic feldspath, uncertain ages
Deformation ages
a: from litterature
b: from this study
Strain pattern
a: regional shortening direction from strike-slip shear zone
b: regional shortening direction from reverse shear zone
West
East
Subalpine chains
Oisans-Pelvoux
Penninic Front
Houiller Front
South Vanoise & Ambin
Cottian Alps
Dora Maira
St.
Grand Paradis

Figure 12

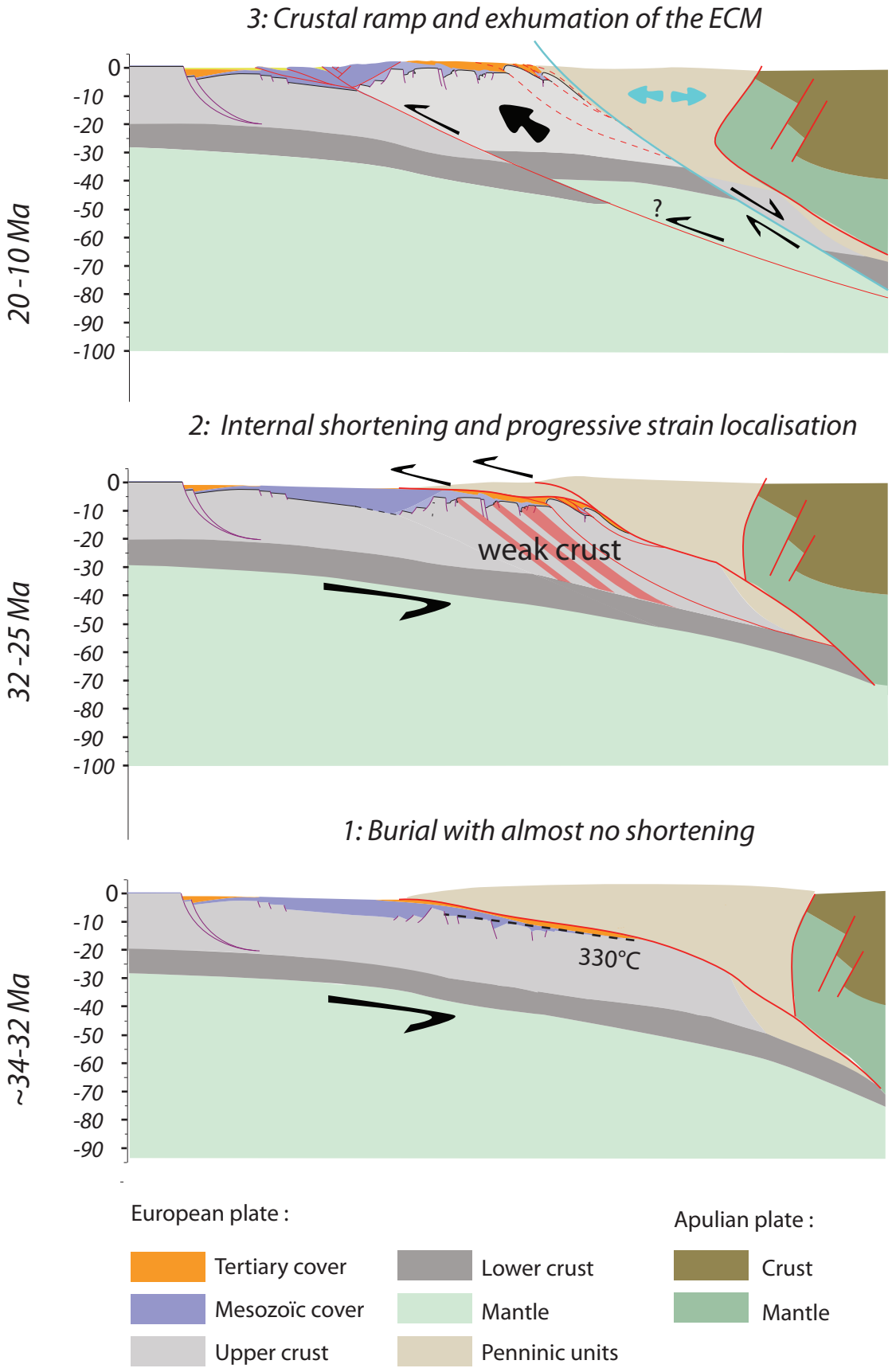
3: Crustal ramp and exhumation of the ECM
20 -10 Ma
0
-10
-20
-30
-40
-50
-60
-70
-80
-90
-100
?
2: Internal shortening and progressive strain localisation
32 -25 Ma
weak crust
1: Burial with almost no shortening
~34-32 Ma
330°C
European plate :
Tertiary cover
Mesozoïc cover
Upper crust
Lower crust
Mantle
Penninic units
Apulian plate :
Crust
Mantle

Figure 13